SRESA's International Journal of

LIFE CYCLE RELIABILITY AND SAFETY ENGINEERING

Vol.4 **Issue No.2** **April–June 2015** **ISSN – 2250 0820**

Special issue

On

"Prognostics & Structural Health Management–Part II"

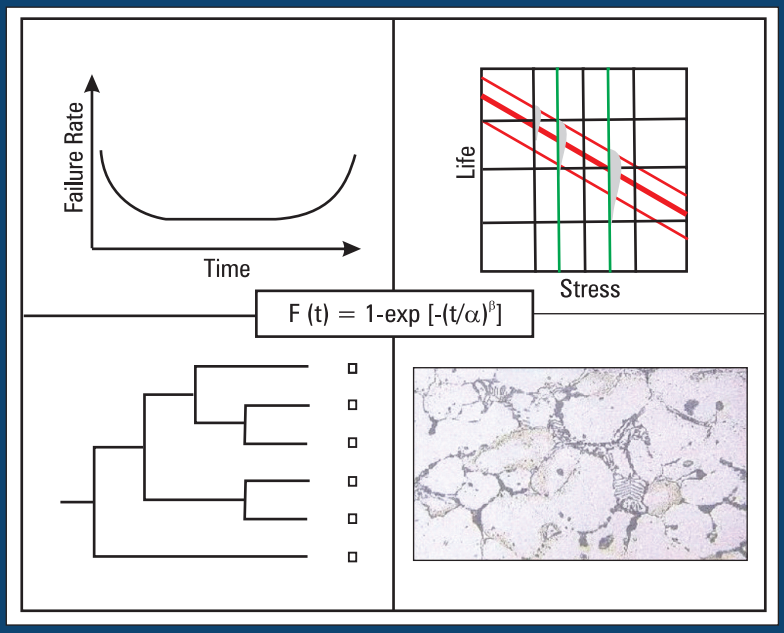

Guest Editor:
Dr. Achintya Haldar

Society for Reliability and Safety

website: http://www.sresa.org.in

SRESA Journal of Life Cycle Reliability and Safety Engineering

Extensive work is being performed world over on assessment of Reliability and Safety for engineering systems in support of decisions. The increasing number of risk-based / risk-informed applications being developed world over is a testimony to the growth of this field. Here, along with probabilistic methods, deterministic methods including Physics-of-Failure based approach is playing an important role. The International Journal of Life Cycle Reliability and Safety Engineering provides a unique medium for researchers and academicians to contribute articles based on their R&D work, applied work and review work, in the area of Reliability, Safety and related fields. Articles based on technology development will also be published as Technical Notes. Review articles on Books published in the subject area of the journal will also form part of the publication.

Society for Reliability and Safety has been actively working for developing means and methods for improving system reliability. Publications of quarterly News Letters and this journal are some of the areas the society is vigorously pursuing for societal benefits. Manuscript in the subject areas can be communicated to the Chief Editors. Manuscript will be reviewed by the experts in the respective area of the work and comments will be communicated to the corresponding author. The reviewed final manuscript will be published and the author will be communicated the publication details. Instruction for preparing the manuscript has been given on inside page of the end cover page of each issue. The rights of publication rest with the Chief-Editors.

SCOPE OF JOURNAL

System Reliability analysis	**Structural Reliability**	**Risk-based applications**
Statistical tools and methods	Remaining life prediction	Technical specification optimization
Probabilistic Safety Assessment	Reliability based design	Risk-informed approach
Quantitative methods	Physics-of-Failure methods	Risk-based ISI
Human factor modeling	Probabilistic Fracture Mechanics	Risk-based maintenance
Common Cause Failure analysis	Passive system reliability	Risk-monitor
Life testing methods	Precursor event analysis	Prognostics & health management
Software reliability	Bayesian modeling	Severe accident management
Uncertainty modeling	Artificial intelligence in risk and reliability modeling	Risk-based Operator support systems
Dynamic reliability models	Design of Experiments	Role of risk-based approach in Regulatory reviews
Sensitivity analysis	Fuzzy approach in risk analysis	Advanced electronic systems reliability modeling
Decision support systems	Cognitive framework	Risk-informed asset management

SRESA AND ITS OBJECTIVES

a) To promote and develop the science of reliability and safety.

b) To encourage research in the area of reliability and safety engineering technology & allied fields.

c) To hold meetings for presentation and discussion of scientific and technical issues related to safety and reliability.

d) To evolve a unified standard code of practice in safety and reliability engineering for assurance of quality based professional engineering services.

e) To publish journals, books, reports and other information, alone or in collaboration with other organizations, and to disseminate information, knowledge and practice of ensuring quality services in the field of Reliability and Safety.

f) To organize reliability and safety engineering courses and / or services for any kind of energy systems like nuclear and thermal power plants, research reactors, other nuclear and radiation facilities, conventional process and chemical industries.

g) To co-operate with government agencies, educational institutions and research oganisations

SRESA's International Journal of

LIFE CYCLE RELIABILITY AND SAFETY ENGINEERING

Vol.4 Issue No.2 April–June 2015 ISSN – 2250 0820

Special issue

On

"Prognostics & Structural Health Management-Part II"

Guest Editor:

Dr. Achintya Haldar

Chief-Editors

P.V. Varde
A.K. Verma
Michael G. Pecht

SOCIETY FOR RELIABILITY AND SAFETY

Typeset & Printed

EBENEZER PRINTING HOUSE
Unit No. 5 & 11, 2nd Floor, Hind Services Industries,
Veer Savarkar Marg,
Dadar (west), Mumbai -28
Tel.: 2446 2632/ 3872
E-mail: outwork@gmail.com

Guest Editorial

Prognostics and structural health management has become an active interdisciplinary research area all over the world. Infrastructures are deteriorating, some of them are over their design life, or they are being exposed to natural extreme events like strong earthquakes or high winds, or man-made events like blasts or explosions. Due to severe shortage of resources to replace them, it is now necessary to extend their design life without exposing public to unnecessary risk. One approach has attracted a considerable amount of attention is inspecting the infrastructures as thoroughly as practicable in a timely manner to identify the defect spots, quantify their severity and then take appropriate remedial actions so that they can be used for which they were initially designed. Researchers from many different disciplines are now concentrating on developing new mathematical techniques, inspection methods, necessary instruments or sensors, sources of energy require to operate the sensors in field conditions, etc. The first two issues of 2015 of this journal Life Cycle Reliability and Safety Engineering are dedicated to these special topics.

Five papers from renowned scholars from all over the world were published in the first issue and another five papers are presented in this second issue.

The state-of-the-art of health assessment of large structural systems using dynamic response information measured at a small part has advanced significantly in the recent past. The related information is summarized in the first paper. The authors and their research team conducted extensive analytical and experimental investigations. The team demonstrated in numerous published articles the technical concepts behind some of the advanced data processing algorithms (filters) they used to extract the information on structural health. It was not possible to elaborate the issues related to non-convergence in the iterative process, uncertainties in the responses induced by measurement devices and during the numerical integration process, phase and amplitude errors inherent in the measured responses, the presence of severe nonlinearities caused by defects, and other related important issues in these articles. The success of any new procedure will depend on the process used to mitigate these challenges and cannot be overlooked. These challenges are multidisciplinary in nature and are emphasized in this paper.

It is widely known that in civil structures, the modal properties of higher modes are difficult to obtain using ambient excitations. This is because under ambient conditions, sufficient energy is not available to reasonably excite the higher modes. This scarcity of data coupled with the problem associated with large dimensionality of the uncertain parameter space often makes the damage quantification a challenging job. In the second paper, damage quantification in a numerically simulated 16-storey and a 6-storey moment resisting frame is done under Bayesian framework with different approaches. In the first approach, a two-stage damage quantification approach is employed where the stages differ with the choice of starting value of Markov Chain. In the second approach, the issue of lack of appropriate data is resolved by modifying the structure with adding some known masses such that its natural frequencies and mode shapes get changed. Therefore, more data can be acquired from the same structure to improve the efficiency of the updating algorithm. Results show that both approaches seem to be promising in model updating/damage quantification based on only a few lower mode shape data.

The problem of estimating reduced complexity metamodels for the accurate representation of computationally costly numerical models with time-varying properties and uncertain input parameters is addressed in this third paper. The introduced metamodeling method is based on the discrete wavelet transform of the dynamic response signals. The coefficients of this transform are defined as random parameters, in this way accounting for the inherent system uncertainties. These random coefficients are expanded onto a polynomial chaos basis resulting into a representation that is fully described via a finite number of deterministic projection coefficients. The effectiveness of the proposed methodology is illustrated through its application on the metamodeling of a finite element model of a simply supported beam featuring a moving mass, simulating the vehicle crossing problem. The attained results demonstrate the efficiency of the proposed methodology for accurate simulation of the involved time-varying dynamics.

In the fourth paper, three methods are presented to reduce the influence of measurement errors in parameter estimation in finite element model updating for structural health monitoring and damage assessment. First, a method using the Fisher information matrix is developed to choose an efficient set of measurement locations.

This ensures efficient setup of a non-destructive test for finite element model updating for a given set of unknown parameters. Second, a normalization scheme is presented that, generally speaking, weighs data in a manner that varies inversely to the level of measurement error. This normalization results in a final estimate that is very close to the maximum likelihood estimator of the unknown parameters. Finally, the Fisher information matrix and its inverse, the Cramer-Rao lower bound covariance matrix, are used to quantify the uncertainty in the final estimates. Numerical examples showed the proposed methods are effective in improving observability and accuracy of parameter estimates in finite element model updating. Minimizing the effect of measurement errors and their propagation in parameter estimates can greatly improve the finite element model updating for structural health monitoring.

Many of the available approaches for Structural Health Monitoring (SHM) can benefit from the availability of dynamic displacement measurements. However, current SHM technologies rarely support dynamic displacement monitoring, primarily due to the difficulty in measuring absolute displacements. The newly developed smartphone application presented in this paper allows measuring absolute dynamic displacements in real time using state-of-the-art smartphone technologies, such as high-performance graphics processing unit (GPU), in addition to already powerful CPU and memories, embedded high-speed/resolution camera, and open-source computer vision libraries. A carefully designed color-patterned target and user-adjustable crop filter enable accurate and fast image processing, allowing up to 120Hz frame rate for complete displacement calculation. The performances of the developed smartphone application are experimentally validated, showing comparable results with those of conventional laser displacement sensor.

Achintya Haldar
Guest Editor
University of Arizona, Tucson, Arizona

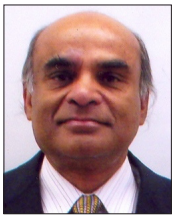

Dr. Haldar is a Distinguished Member of ASCE and a Fellow of Structural Engineering institute. He started his research career at the University of Illinois (M.S., 1973 and Ph.D., 1976). After graduation, he worked two years for Bechtel Power Corporation in Los Angeles. Then he returned to an academic career, first at Illinois Institute of Technology, then at Georgia Institute of Technology, and now at the University of Arizona (UA). He also taught courses at Hong Kong University of Science & Technology and at the Technical University of Ostrava in the Czech Republic. He conducted research at the University of Tokyo and Indian Inst. of Science, Bangalore, India. In addition, Dr. Haldar has more than 5 1/2 years of practical experience. Dr. Haldar was the founding Editor-in-Chief for "Engineering under Uncertainty; Hazards, Assessment and Mitigation." He was an associate editor of the ASCE's Journal of Structural Engineering. Dr. Haldar was a co-chair of the Probabilistic Mechanics Conference sponsored by the ASCE. He also organized Euro-SiBRAM'02 in Prague, Czech Republic. Dr. Haldar received numerous recognitions for his service and exceptional teaching at the highest level. They are listed at haldar.faculty.arizona.edu.

Dr. Haldar's research emphasizes the presence of uncertainty in engineering problems. Recently, under a research grant from the NSF, he has been working on multiple deterministic analyses to capture the presence of uncertainty. If successful, it will revolutionized engineering computations. So far, Dr. Haldar has published over 450 technical publications, including 10 books, 25 book chapters, and made numerous keynote and invited presentations worldwide. For the areas covered in this special issue, he published 1 edited book, 6 book chapters, gave 3 special lectures, over 46 referred papers, over 21 conference papers, and gave 22 special invited international presentations. He has advised a large number of graduate students. Some of them are now professor in the U.S., Canada, Jordon, Korea, Mexico, Taiwan, West Bank, etc.

Dr. Haldar received many awards for his research, including the first Presidential Young Investigator Award and the ASCE's Huber Civil Engineering Research prize. He received an Honorable Diploma from the Czech Society for Mechanics. He received the Distinguished Alumnus Award from the CEE Alumni Association, University of Illinois. He received inaugural da Vinci fellowship from the College of Engineering. ASME gave him the Honorable Recognition Award. He received John C. Park Outstanding Civil Engineer Award in from the Arizona Society of ASCE. He was selected one of 23 Scientists and Technologists of Indian Origin abroad (STIOs) by the Government of India for collaborative projects with Indian scientists and technologists. Recently he received Honorary Distinguished Visiting Professorship, Bengal Engineering and Science University, Shibpur, India, 2013-2018 and Invited Wenyuan Lecture Professorship, Tongji University, Shanghai, China, 2013.

Life Cycle Reliability and Safety Engineering
Vol.4 Issue 2 (2015) 01-12

Issues on Structural Health Assessment and Monitoring under Measurement Uncertainty and Nonlinearity

Ajoy Kumar Das and Achintya Haldar*
Dept. of Civil Engineering & Engineering Mechanics, University of Arizona,
P.O. Box 210072, Tucson, AZ 85721, USA;
Email: haldar@u.arizona.edu

Abstract

The state-of-the-art of health assessment of large structural systems using dynamic response information measured at a small part has advanced significantly in the recent past. The authors and their research team played an important role in developing the area and published extensively. They conducted extensive analytical and experimental investigations. The team demonstrated in numerous published articles the technical concepts behind some of the advanced data processing algorithms (filters) they used to extract the information on structural health. It was not possible to elaborate the issues of non-convergence in the iterative process, uncertainties in the responses induced by measurement devices and during the numerical integration process, phase and amplitude errors inherent in the measured responses, the presence of severe nonlinearities caused by defects, and other related important issues. The success and failure of any new procedure will depend on the process used to mitigate these challenges and cannot be overlooked. These challenges are multidisciplinary in nature and are emphasized in this paper.

Keywords*: System identification; Uncertainty and nonlinearity; Dynamic responses; Mathematical model; Unknown excitation.*

1. Introduction

Extending the life of existing structures has become an economic necessity all over the world. It has attracted a multi-disciplinary research interest. Several methods with various degrees of sophistication are now available. The research team at the University of Arizona has been working on the related areas and proposed various methods. The team conducted extensive analytical and experimental investigations and published extensively. However, some of the fine but important observations the team made are not properly clarified or explained in the published technical articles; emphasis was given to the major mathematical developments. The authors would like to present some of these observations in this paper.

Structural health assessment and monitoring (SHAM) is the process of assessing the state of health (defect-free or defective) of structures. Most of the civil engineering structures are expected to be defective from the very early stage of their operation. Defects are expected to be very minor in nature and may not compromise the intended use of the structures. Thus, assessing the overall health of a structure is not the primary goal of SHAM at the time of inspection. Furthermore, all defects are not equally important. The challenges are to detect defects at the element level and then assess defect severity in terms of structural integrity to provide services for which they were built. For the rapid assessment of structural health, the process should be based on some measure of the structural behavior at the time of inspection. It should be simple to implement, robust, economical, and accurate.

Because of its numerous advantages, dynamic response information measured during an inspection has become one of the most widely used approaches to the scholars [1]. The research team also concluded that to avoid contamination from several sources of excitation, a very small duration of acceleration time histories measured at a high sampling rate will be ideal for the SHAM purpose. To detect defects at the element level, the team decided to represent a real structure by Finite Elements (FEs). By tracking the changes in the dynamic properties (essentially the stiffness) of each element with respect to previous value, or expected value obtained from the design, or variation with respect to other similar elements, the health of a structure can be assessed at the local element level. By knowing the excitation and response information and using an inverse technique

commonly known as System Identification (SI), the current stiffness properties of all the elements can be estimated. Mathematically, the concept can be represented as discussed below.

For a multi-degree of freedom (MDOF) structural system with *ne* number of elements and *N* number of dynamic degrees of freedom (DDOFs), the governing differential equation of motion in the matrix form can be written as:

$$\mathbf{M}\ddot{\mathbf{X}}(t) + \mathbf{C}\dot{\mathbf{X}}(t) + \mathbf{K}\mathbf{X}(t) = \mathbf{F}(t) \quad (1)$$

where **F**(t) is the $N \times 1$ input excitation force vector; $\ddot{\mathbf{X}}$, $\dot{\mathbf{X}}$, and $\mathbf{X}$ are the $N \times 1$ output vectors containing measured information on acceleration, velocity, and displacement at all the DDOFs at time *t*; **M**, **K**, and **C** are the $N \times N$ global mass, stiffness, and damping matrices, respectively. They are the system parameters and assumed to be time-invariant at the time of inspection.

For the purpose of SI, the above mathematical model can be represented in a block diagram, as shown in Figure 1. The SI block consists of three components; (a) the input excitation that generated the responses, (b) the parameters in the mathematical model using FEs and the governing differential equation of motion represented by Eq. 1, and (c) output responses caused by the excitation. To calculate the system parameters using a SI technique, two approaches are commonly used; (a) development of an over-determined linear system of equations and the solution using the least-squares procedure and (b) development of state equations and solution using recursive procedures, such as Kalman Filter (KF)-based procedures.

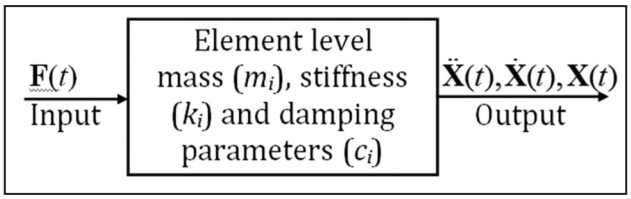

Figure 1: Concept of System Identification

2. Challenges in the Development of SI-based SHAM Techniques

The above concept appears to be conceptually simple. As discussed earlier, one of the most desirable features of a potential SHAM procedure is that it should be easily implemented for the rapid assessment of structural health. When the information on excitation and responses is available, the SI-based concept appears to be straight forward. Outside the laboratory environment, measuring excitation information could be error prone and problematic. The implementation potential can be improved significantly if a structure can be identified using only measured dynamic response information. Since two of the three components of the SI-based concept will be unknown, it will add a layer of challenges that needs to be overcome. The research team proposed several methods of SI without excitation information [1-8]. Thus, this challenge is not a game stopper.

The next challenge is to assess health of a large realistic structure where responses may not be available at all DDOFs. It may be impractical and economically prohibitive to instrument a large structure. A structure needs to be identified with a limited number of responses measured only at small parts of the structure. The Kalman filter-based concept is generally used when response information is limited. However, to implement the concept, the information on excitation and the initial state vector must be available. The first constraint will defeat the main purpose of SI with unknown input. The second constraint relates to the main purpose of the method; it will be unknown at the initiation of the inspection. The team addressed both issues by introducing a substructure concept. The concept will help to identify the unknown excitation information and the initial state vector [2, 5, 7-9].

The most significant challenge pointed by Maybeck [10] is that the SI-based concept cannot be used to identify structures using experimental measured information and deterministic formulations. He correctly pointed out the primary reasons for his conclusion. First, correctly specifying the system's mathematical model can be challenging. Mathematical models to represent large existing structures are generally approximate and do not necessarily represent the true or physics-based behavior of the system. There are various parameters that are left unaccounted for because of the lack of knowledge. Second, dynamic structural systems cannot be perfectly driven by control inputs. They are also driven by disturbances that can neither be controlled nor modeled using deterministic formulations. Third, if experiments are conducted to measure altered responses caused by the defects, noises in the measurements corrupt the data and introduce some degree of uncertainty.

Thus, before developing the SI-based concept, Maybeck's concerns must be addressed. The authors and their team successfully addressed all these issues and proposed several Kalman filter-based algorithms [2, 5, 7-9]. The steps they took to mitigated all the

challenges need further consideration. They are emphasized in this paper.

3. Recent Development and State-of-Art Advancements in SI-based SHAM Techniques

This section will discuss the works done at the University of Arizona, contribution made by other researchers in the similar areas, and the improvements necessary for health assessment of large real structural systems. The least-squares (LS)-based estimation procedure mentioned above is appropriate when the input excitation is unknown. Wang and Haldar [1] proposed a procedure, popularly known as Iterative Least-Squares with Unknown Input (ILS-UI), to implement the LS-based concept. They used viscous-type structural damping. The efficiency of the numerical algorithm was improved later by introducing Rayleigh-type proportional damping, known as Modified ILS-UI or MILS-UI [3]. Later, Katkhuda et al. [4] improved the concept further and called it Generalized ILS-UI or GILS-UI. Recently, Das and Haldar [8] extended the procedure for three dimensional (3D) large structural systems and denoted as 3D GILS-UI.

For the SHAM of large structural systems, the LS-based approaches may not be appropriate, since the responses are expected to be measured only at small parts of the structure. After an extended study, the research team at the University of Arizona concluded that the prediction-correction-based recursive procedures embedded in the extended Kalman filter (EKF) with Weighted Global Iteration (WGI) concept would be appropriate when measured responses were limited. However, to implement the EKF-WGI concept, two additional conditions must be satisfied. First, to satisfy the governing equation of motion of the structural dynamic system, the excitation information must be known, defeating the basic objective of SHA without using excitation information. Second, the initial value of the state vector must be known to start the local iteration. The research team concluded that these issues can be resolved by using a substructure approach. For overall SHA, they proposed a two-stage approach [5].

Stage 1 – Using the available responses in the substructure(s) and applying the ILS-UI procedure, the information on the unknown input excitation and stiffness and damping parameters of all the elements in the substructure are generated.

Stage 2 – Judicially using information on the state vector obtained in Stage 1 and the excitation information, the EKF-WGI concept can be implemented and then the whole structure can be identified. In this way, the health of the whole structure can be assessed using only limited number of noise-contaminated response information.

The concept was initially denoted as ILS-EKF-UI [2]. Later, it was improved further and denoted as Modified ILS-EKF-UI or MILS-EKF-UI [3] and Generalized EKF-UI or GILS-EKF-UI [5]. Most up-to-date version of the concept is a three-stage procedure, known as ILS-EKF-UI-ADIT [11], developed for any general three dimensional structures.

Various other researchers have also attempted to develop such procedures. They are indicated here for the sake of completeness. Yang et al. [12] proposed a recursive least-squares estimation procedure with unknown inputs (RLSE-UI) for the identification of stiffness, damping, and other nonlinear parameters, and the unmeasured excitations. Yang and Lin [13] implemented an adaptive technique in RLSE-UI to track the variations of structural parameters due to damages. This procedure can appropriately provide damage time instant in continuous monitoring. Then, Yang et al. [14] proposed a new data analysis method, denoted as the sequential nonlinear least-square (SNLSE) approach, for the on-line identification of structural parameters. Later, Yang and Huang [15] extended the procedure for unknown excitations and reduced number of sensors (SNLSE-UI-UO). They verified the procedures for simple linear and nonlinear structures. Wang and Cui [16] proposed least-squares method with statistical averaging algorithm (LSM-SAA). Several other methods based on least-squares approach can also be found in [17-24].

Other procedures using unknown input include iterative gradient-based model updating method based on dynamic response sensitivity [25] and genetic algorithm (GA)-based output only procedure [26].

Similarly, the Kalman filter-based procedures have been developed by various other researchers. Koh and See [27] proposed an adaptive EKF (AEKF) to estimate both the parameter values and associated uncertainties in the identification. Yang et al. [28] proposed an adaptive tracking technique based on EKF to identify structural parameters and their variation during damage events. Ghosh et al. [29] developed two novel forms of EKF-based parameter identification techniques; these are based on variants of the derivative-free locally transversal linearization (LTL) and multi-step transverse linearization (MTrL)

procedures. Liu et al. [30] proposed multiple model adaptive estimators (MMAE) that consists of bank of EKF designed in the modal domain (MOKF) and incorporated fuzzy logic-based block in EKF to estimate the variance of measurement noise Recently a significant research has been published on the application of empirical mode decomposition and Hilbert transform (EMD-HT) [31] for non-model based structural health assessment.

This section documented the up-to-date progress in the SHA using SI-based approaches. The research team at the University of Arizona attempted to overcome the theoretical and implementation challenges for the SHA of real structural systems covering over two decades. They had to overcome some of the major challenges that slowed the progress in the related areas in the past. Some of their major contributions are discussed below.

4. Addressing Uncertainty in SI-based SHAM and Non-convergence Issues

Challenges in the development of SI-based SHAM have been discussed earlier. One of the major issues that cause non-convergence in the algorithm is the uncertainty in the measured response information. This is specifically addressed in this section.

4.1 What is Measurement Uncertainty?

Measurement uncertainty relates to the accuracy of the measurements recorded by a sensor or equipment. Any measurement is subject to some level of uncertainty. Various unknown sources contribute to measurement uncertainty, such as uncertainties introduced by the measuring device, by the object being measured, by the environmental disturbance, by the operator and many other sources. Deterministic analyses cannot incorporate uncertain processes. Statistical procedures are necessary to incorporate the presence of uncertainty in the measurements. Two most important statistical parameters calculated in any uncertainty analysis are the mean and the standard deviation.

Measurements are repeated several times to obtain more confidence in the measurement. An average gives an estimate of the unknown 'true' value. It is also of interest to know how widely the results are spread about this average or mean. Standard deviation is used to quantify the spread of the measurements and gives an idea about the uncertainty. The most recent methods proposed by the research team require information on the measured acceleration time-histories at a limited number of DDOFs. Thus, mitigation of uncertainties in acceleration time-histories, both translational and rotational, requires further discussion.

4.2 Uncertainty in Measured Responses

Acceleration time-histories are generally preferred over velocity and displacement measurements due to several advantages. They are discussed elsewhere [7]. Measured time-history of responses, however, do not necessarily produce the true desired signals. Acceleration time-histories measured using accelerometers contain uncertainties from various unknown sources. The uncertainties can be grouped into two forms; (a) error introduced in accelerometer's and autocollimator's raw signal and (b) error introduced in the numerical integration process [32]. Uncertainties in a raw acceleration time history produced by a sinusoidal excitation are shown in Figure 2. They include the baseline errors (DC bias and slope), noise, and the high-frequency contamination.

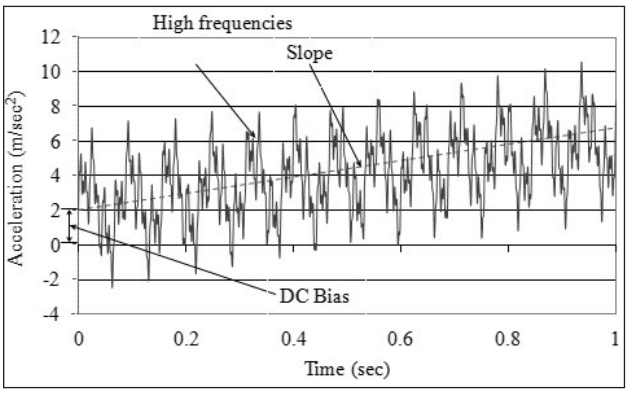

Figure 2: Typical raw signal from accelerometer [33]

The DC bias causes shift of the mean of the dynamic response from its zero mean. The slope introduces linear or nonlinear trend in the signal. Noise and high frequencies cause distortion of the regular wave form of the signal.

They are difficult to remove from the time histories. Normalizing the raw data about its mean is expected to remove most of the DC bias. If there is presence of a linear slope in the time history, it can be removed with the linear regression fitting technique. If a slope is not removed, when the acceleration time history is integrated to obtain velocity and displacement time histories, it will introduce a parabolic shape and cubic polynomial, respectively. Thus, the cubic polynomial is an error due to integration of a sinusoidal acceleration time history with slope. Most of the noise can also be removed from the measured time history. To remove noise, a low-pass filter is usually used. This process can be undertaken along with the process to remove high frequency responses as discussed next. Sometimes

unwanted high frequency response is misclassified for noise because they cannot be distinguished from the time domain data plot. To detect the presence of high frequency responses, the Fast Fourier Transformation (FFT) is often used. Once the presence of unwanted frequencies is identified, filtering techniques can be used to remove them. Low-pass filters are used to remove high frequencies and high-pass filters are used to remove low frequencies. If only a particular frequency is of interest, both low-pass and high-pass filters can be used together, or a band-pass filter can be used to remove all the frequencies outside of the frequency band of interest.

4.3 Uncertainties Introduced during Numerical Integration

Filtered acceleration time-histories are integrated successively to obtain velocity and displacement time-histories required for the purpose of SHAM. Filtered acceleration time-histories when integrated successively using numerical integration procedures introduces errors of integration. For the sake of discussion, let's assume that DC bias (offset) and slope can be removed from a signal appropriately using numerical procedures. Theoretically generated time-history of an acceleration signal contaminated with 5% RMS noise is shown in Figure 3. Time resolution of the response is 0.0001s. Using rectangular method of integration, the acceleration time-history is numerically integrated successively to obtain velocity and displacement time-histories. The velocity and displacement time-histories are shown in Figure 4 and 5, respectively. The velocity and displacement time-histories obtained by integration are compared with the theoretical time-histories. It can be observed that the integrated velocity time history slightly differs (not visible in Figure 4) from the theoretical time history. However, large error in the integrated displacement time history can be seen in Figure 5, along with the visible errors of the offset and slope. Even if the acceleration is assumed to be noise-free, discrepancies can be observed while integrating the acceleration time history. Obviously these types of error can cause non-convergence for some cases of structural parameter identification.

Issues of non-convergence due to integration errors are well-known in the research community. Vo and Haldar [32] reported issues of non-convergence. They attempted to mitigate integration errors by using several integration techniques and performed a comparative study on the efficiency of the schemes. Two theoretical signals, one is a simple sinusoid

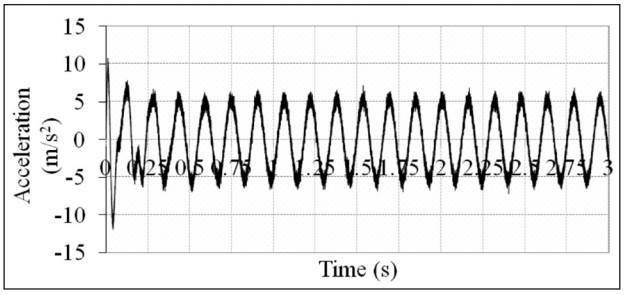

Figure 3: Time-history of a theoretical acceleration contaminated with 5% RMS noise [11].

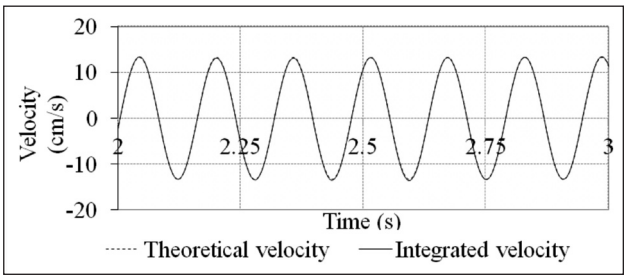

Figure 4: Time-history of velocity obtained from the acceleration shown in Figure 3 [11].

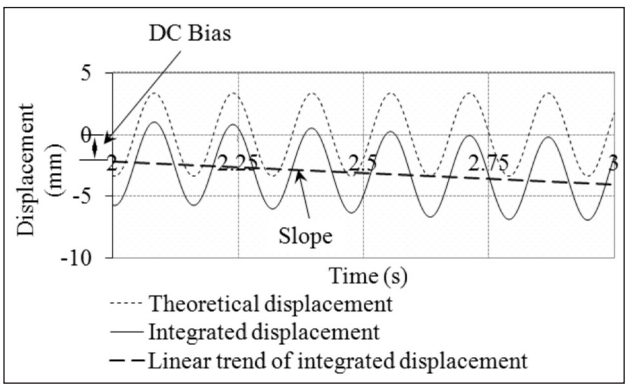

Figure 5: Time-history of displacement obtained from the velocity shown in Figure 4 [11].

with no damping and another with under-critical damping was taken as the integrand and numerical integration was performed between 0 and 1 sec. Closed form integrations were available for both the signals. Three methods, trapezoidal rule, Simpson's rule and Boole's rule, were considered as the methods of integration. Uniformly spaced intervals of 100, 200, 500, 1000, 2000, 5000, and 10000 were considered. For the first example, the maximum integration error was 10^{-4} for Simpson's rule with an interval of 100. For the second example, the maximum integration error was 10^{-5} for trapezoidal rule with an interval of 100. For all other intervals the trapezoidal rule has been found to produce higher errors comparative to the other methods for both the signals. It has also been observed that with the decrease in the interval, the integration errors go down significantly. In any

case, when the integration errors are compared with actual accelerometer's output error (typically 2 to 5%), it does not matter which integration method is used. When the signal is sampled at less than 0.01 sec, the integration error would be at least two orders of magnitude less than that of the accelerometer's error. It was commented that the trapezoidal rule is preferred to both Simpson's rule and Boole's rule because of its simplicity and efficiency in computing time.

The above conclusion is valid for regular harmonics, such as sinusoids. If the acceleration time-history is irregular, for example an earthquake time-history or when the signal is not a steady-state time-history, the above conclusion may not be totally true. Mitigation of integration errors based on their underlying physics and development of advanced digital integration schemes is now under development by the research team at the University of Arizona.

4.4 Phase and Amplitude Errors

While conducting laboratory investigation for the identification of a one-dimensional beam and a two-dimensional frame using measured responses, the team at the University of Arizona observed that post-processed data failed to identify structures for the structural health assessment purpose [33-34]. The algorithm failed to converge providing negative stiffness for some of the elements. The team performed root cause analysis considering several possible sources of errors and identified that the amplitude error and phase-shift error, shown in Figure 6, are the main contributing factors to the non-convergence. Accelerometers are supplied with a calibration factor to convert accelerometer's output voltage into acceleration unit. The provided scale factor always has calibration error embedded in it, causing amplitude error. Another source of error that directly contributes to the amplitude error is the misalignment of the sensing element mounted inside the accelerometer's case. This error is often referred to as cross-coupling. For the accelerometers used by the research team, the combined root-sum-squared error for scale factor error and cross-coupling is ±2.8%. The algorithm has been observed to converge up to a convergence threshold of 0.5%. Thus, the post-processed acceleration time-histories will fail to identify a structure if the error crosses the threshold.

The phase-shift error, as shown in Figure 6, is generally caused by data latency and the numerical integration of noisy signal. However, the primary source of the phase-shift error is the integration of

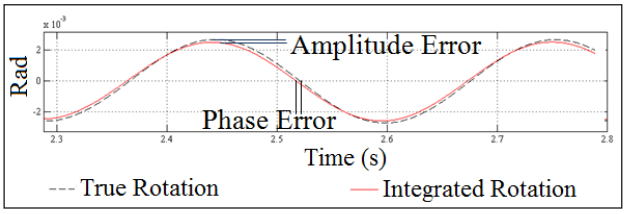

Figure 6: Amplitude and phase errors in a signal.

the measured acceleration time-histories to obtain velocity and displacement time-histories. The worst case phase-shift for velocity was estimated to be 1.8 degrees. Displacement response phase-shift was estimated to be a maximum of 6.5 degrees. The second source of phase-shift error is data latency caused by the sampling rate of the data-logger. This error occurs because there is a time delay in the sampling of two consecutive responses. The data-logger used in the test has a maximum latency of one micro-second. For 5 channels of data recording, a total latency of 5 micro-seconds is expected. For the tests, the phase shift error of data latency is found to be 0.09 degrees and integration error of 6.5 degrees. The algorithm converges only up to 0.5 degrees [32]. In summary, the algorithms are found to be sensitive to both amplitude and phase-shift errors.

4.5 Mitigation of Phase and Amplitude Errors

The research team observed that by using fewer nodal responses, the total amplitude error can be reduced. The phase-shift error can be mitigated by scaling responses of all nodes based on the responses of a single reference node. The reference node can be chosen arbitrarily; however, the team used the excitation node at the reference node. Vo and Haldar [34] discussed related issues in more details.

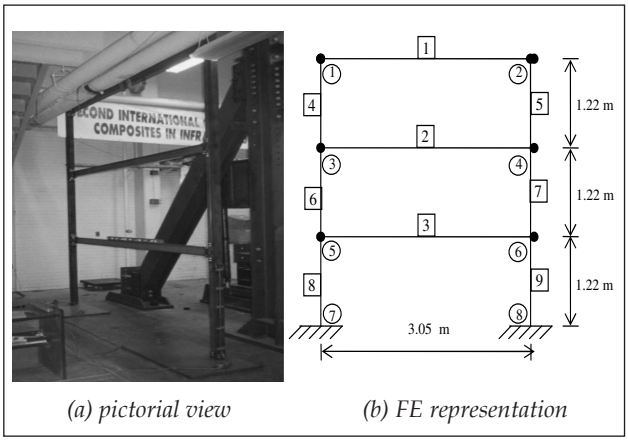

Figure 7: Experimental verification of a two-dimensional frame [35].

Martinez-Flores et al. [35] conducted experimental verification of a scaled three-story two-dimensional frame, as shown in Figure 7. In order to mitigate the two prime sources of errors, the authors measured horizontal translational acceleration time-histories at all six node points. Then, the angular response time-histories were generated based on the proportionality of the transverse to angular responses. The proportionality constant of each rotational DDOF in the frame was estimated with respect to reference nodal response at node 2. They showed that theoretically generated and experimental measured angular responses using an autocollimator are very similar, indicating the validity of the response scaling approach.

In his doctoral thesis, Das [11] reported similar non-convergence issues while developing the structural health assessment procedure for three-dimensional large structural systems. A three-stage procedure combining Advanced Digital Integration Technique (ADIT) and Iterative Least-Squares Extended Kalman Filter with Unknown Input (ISL-EKF-UI) has been proposed. After performing integration using ADIT technique, the amplitude and phase shift errors are mitigated by using a scaling approach which is based on scaling angular responses (as many as possible) from the transverse responses. Then, as many responses as possible are scaled at other nodes from the reference node. The scaling procedure is discussed here for a one-story three dimensional frame, as shown Figure 8.

Case (a) - Rotational responses about *X*-axis at node 1 are scaled from translational responses along *Z*-axis at node 1. Rotational responses about *X*-axis at node 2 are scaled from translational responses along *Y*-axis at node 2. Rotational responses about *X*-axis at node 3 are scaled from translational responses along *Z*-axis at the node 3.

Case (b) - After angular responses at a node are scaled from the translational responses at the same node, responses at other nodes are scaled from reference responses at node 1. Translational response along *X*-axis at node 2 is scaled from the translational response along *X*-axis at node 1. Translational responses along *Y*-axis and *Z*-axis and rotational responses about *X*-axis are scaled from the corresponding responses at node 1.

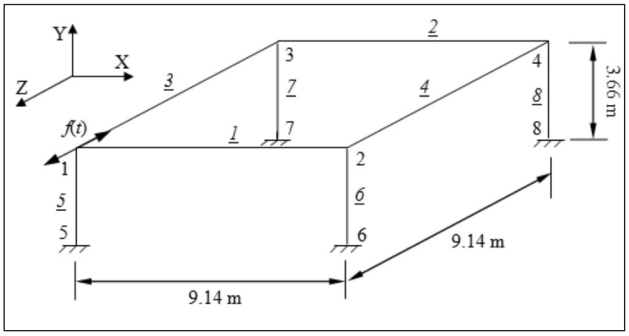

Figure 8: A single-story three-dimensional frame [11].

Structural identification and health assessment of the three-dimensional frame using the responses corrected for amplitude and phase errors are discussed in detail in the doctoral dissertation by Das [11].

5. Nonlinearity in Structural Dynamic Response

Dynamic responses measured for structural assessment always contain some form of nonlinearity. The issues of nonlinearity need to be addressed based on their sources and types.

5.1 Sources of Nonlinearity

Nonlinearity in a system may come from several sources. The solution of the dynamic governing equation itself introduces nonlinear responses in terms of sine, cosine functions and exponential decay terms. For a linear structure, the estimation of the unknown parameters jointly with nonlinear dynamic responses in the state is a nonlinear estimation problem. In other words, the state vector of the system, which needs to be identified, includes system parameters and nonlinear responses and this makes the structural system identification is nonlinear. Wu and Smyth [36] made similar conclusions and commented "the system is linear; however, the estimation of the unknown parameters jointly with the state is a nonlinear estimation problem."

If the level of excitation is severe, it may also cause nonlinearity due to inelastic stiffness and damping. In the context of SHAM, during an inspection, the structure is not expected to be excited severely. But the presence of defects in structure will introduce another unknown but major source of nonlinearity at the initiation of inspection. This source of nonlinearity cannot be mathematically expressed during the inspection process because it is unknown. But its presence will be very clear if EKF-based procedure failed to identify the structure. Since at the beginning of an inspection, the current defect-free or severity of defective state will be unknown, it is preferable and more conclusive if an Unscented Kalman filter (UKF)-based procedure is used for structural health assessment.

5.2 Effect of Nonlinearity

Measured structural dynamic responses are expected to be nonlinear. Responses obtained by solving the governing equation (Eq. 1) and the presence of material and geometric nonlinearity introduce nonlinear response behavior. The degree of nonlinearity depends on many parameters including the geometry, applied excitation, material property, presence of defects, boundary conditions, etc. A framed structure is considered to theoretically demonstrate how nonlinearity alters dynamic responses. In the context of structural health assessment, the nonlinear responses can be handled in several ways. The research team successfully used Extended Kalman filter (EKF) concept to identify structures with mildly nonlinearity. In the presence of severe nonlinearity, the team used the UKF concept. The discussion on UKF can be found in [9].

A five-story two-dimensional frame is considered. Configuration of the frame is described elsewhere [37]. The frame is constrained in the vertical direction, since the lateral deformation due to bending is expected to be much higher than the vertical deformation. The frame is exited in the horizontal direction by a time-history of dynamic loading with large amplitude, such that geometric and material nonlinearities are introduced in the responses. Comparison of linear and nonlinear translational acceleration, velocity, and displacement of at the top story where the excitation has been applied are shown in Figures 9, 10, and 11, respectively. As can be observed, the nonlinear responses differ from the linear responses in terms of both phase and amplitude. The Power Spectrum Density (PSD) plots obtained by performing FFT of the signals are shown in Figures 12, 13, and 14, for the acceleration, velocity and displacement, respectively. No visible difference is observed between the linear and nonlinear responses. Therefore, FFT-based approach is not suitable to assess if the responses are

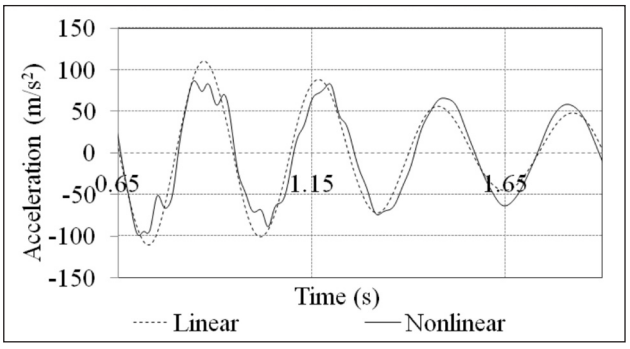

Figure 9: Time-history of linear and nonlinear acceleration.

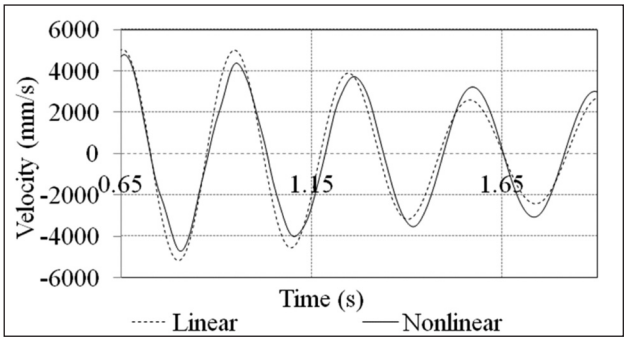

Figure 10: Time-history of linear and nonlinear velocity.

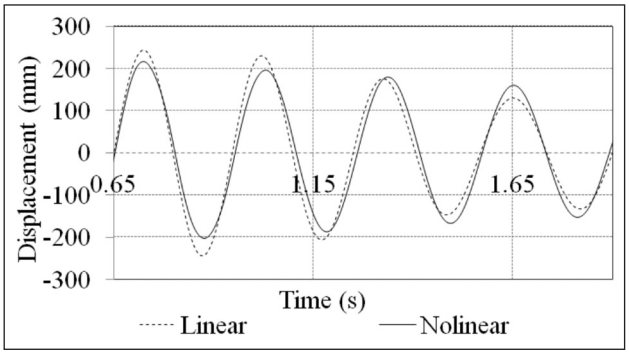

Figure 11: Time-history of linear and nonlinear displacement.

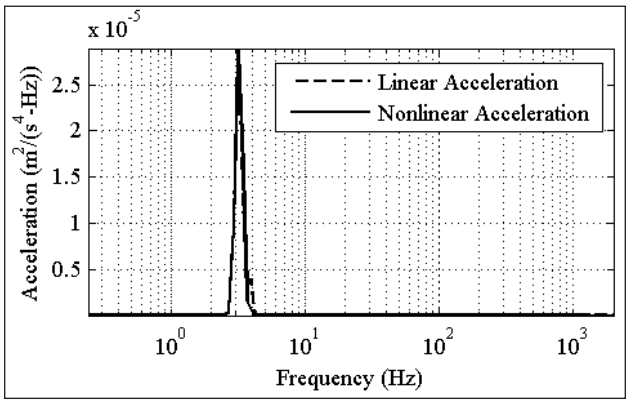

Figure 12: Power spectrum density plot for linear and nonlinear acceleration.

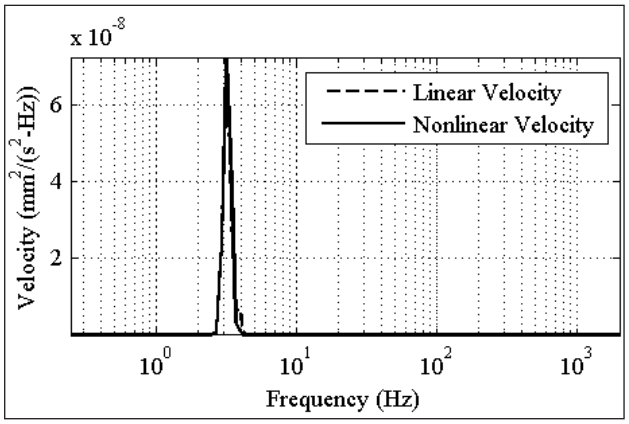

Figure 13: Power spectrum density plot for linear and nonlinear velocity.

Table 1: Statistical moments of linear and nonlinear acceleration (m/s²), velocity (m/s), displacement (m)

Statistical Moments	Acceleration		Velocity		Displacement	
	Linear	Nonlinear	Linear	Nonlinear	Linear	Nonlinear
Mean	1.301	1.228	0.004	0.000	-0.002	-0.002
Standard Deviation	54.375	51.286	2.627	2.490	0.128	0.122
Kurtosis	-1.020	-1.263	-1.103	-1.240	-1.172	-1.320

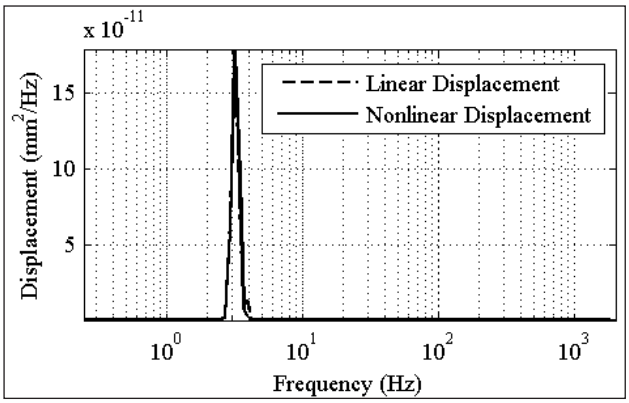

Figure 14: Power spectrum density plot for linear and nonlinear displacement.

coming from linear or nonlinear dynamic systems. Further investigation was conducted to see if the statistical moments (see Table 1) could provide any indication of nonlinearity. It can be observed that the mean is very close to zero, which is expected. The standard deviation and kurtosis are observed to decrease from linear to nonlinear. However, such decrease may not be significant for weak nonlinearity. Further investigation would be necessary on a case by case basis.

For the structural parameter identification, a procedure must be intelligent to assess if the responses are linear or nonlinear and use the appropriate mathematical model accordingly. If the model assumed for structural identification is linear whereas the actual measured responses are nonlinear, the identification will be erroneous. As discussed earlier, several researchers have developed linear system identification techniques using iterative least-squares, various forms of Kalman filters, genetic algorithm, etc. Some of them are applicable for nonlinear systems as well, such as Extended Kalman filter-based procedure. In any case, the first step in such structural identification should be the identification of the type of the response. Fourier Transform (FT)-based procedures are not sufficient for this purpose since they are based on linearity. Hilbert-Huang Transform (HHT)-based procedures developed by Huang et al. [31] are popularly used for post-processing of nonlinear and nonstationary responses. Wavelet-based procedures are also used.

5.3 SHAM of Nonlinear Structures - Unscented Kalman Filter (UKF) Concept

When the nonlinearity is mild, extended Kalman filter (EKF) can be used. The authors observed that there is a threshold of nonlinearity, unknown in most cases, beyond which EKF may not identify a structure appropriately. To obtain the optimal solution to the nonlinear filtering problem, a complete description of the conditional probability density function is necessary. Unfortunately, a large number of parameters are required for its description. In the past decades, many techniques of suboptimal approximation have been developed for nonlinear structural SI [38]. The EKF concept has been widely used for nonlinear system identification through linearizing nonlinear models. However, the derivation of the Jacobian matrices and the linearization approximations to the nonlinear functions can be nontrivial and can lead to implementation difficulties, particularly when the nonlinearities are severe. To address these limitations Julier et al. [39] developed the UKF concept. It is further enhanced by Wan and Van Der Merwe [40]. UKF was developed with the underlying assumption that approximating a Gaussian distribution is easier than approximating an arbitrary nonlinear function. Unlike EKF, UKF does not approximate nonlinear equations of the system. Instead, it approximates the posterior probability density by a Gaussian density function, which is represented by a set of deterministically selected sample points. Suppose, a nonlinear function $y = e^{2x}$ and x is a Gaussian random variable with a mean of 1.5 and a variance of 0.25. The

Table 2: Comparison between true and predicted mean and variance of $y = e^{2x}$

	True	UKF	EKF
Mean of y	33.12	30.99	20.09
Variance of y	793.40	795.15	403.43

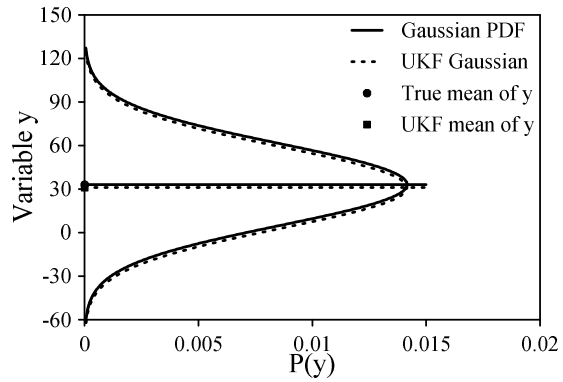

(i) Gaussian probability distribution function (PDF) of y

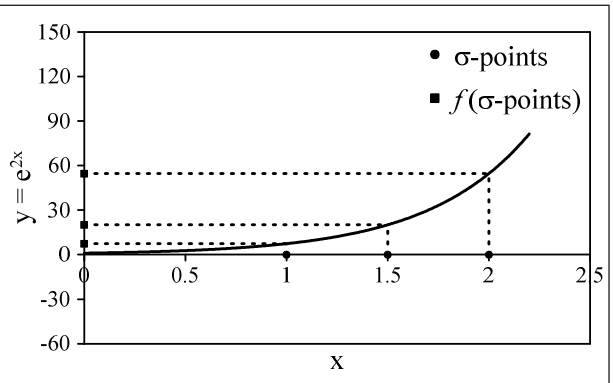

(ii) Function relationship

(a) Propagation of Uncertainty using UKF

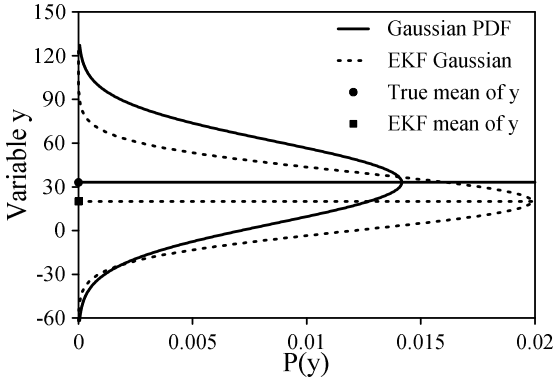

(i) Gaussian probability distribution function (PDF) of y

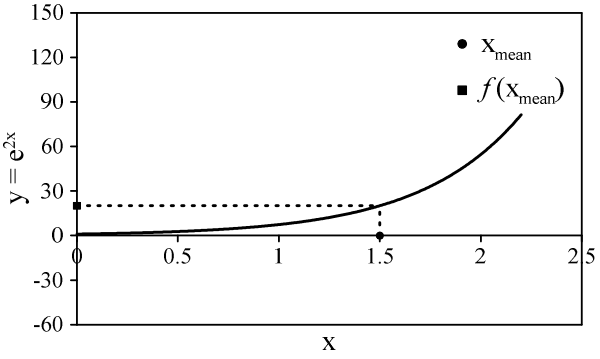

(ii) Function relationship

(b) Propagation of uncertainty using EKF

Figure 15: Propagation of uncertainties using UKF and EKF

true mean and variance of y can be calculated as 33.12 and 793.40, respectively, as shown in Table 2. The corresponding mean and variance of *y* according to UKF and EKF are also given in Table 2. The differences and the errors associated with the two procedures can be clearly observed from the results.

When sample points are propagated through a nonlinear transformation, they capture the true mean and covariance up to the second-order of any nonlinearity. If the priori random variable is Gaussian, the posterior mean and covariance are accurate to the third-order for any nonlinearity. The concept is described in Figure 15.

6. Additional Challenges

SHAM is an evolving area of research. Various unknown challenges often arise while verifying and validating the theoretical procedures for a practical structural inspection, specifically for large structural systems. Other than uncertainty and nonlinearity, the research team at the University of Arizona addressed several other challenges. Some of them are discussed here.

6.1 Generation of Additional Response without Repeating Inspection

As briefly discussed in Section 3, the research team introduced the substructure concept to implement the Kalman filter-based algorithms to identify structures with minimum response information. For economic reason, the size of the substructure, where dynamic responses are measured, is to be kept to an absolute minimum. However, the team observed that the errors in the identification using the absolute minimum substructure could be high and the health assessment can be inconclusive. The team also observed that the errors in the identification can be reduced significantly by using more response information. Obviously, collection of additional responses after the conclusion of the inspection may not be possible or can be highly expensive. The team successfully used the scale

factor concept discussed in Section 4.5 to mitigate the phase and amplitude errors and generate additional response information without conducting any additional testing. The concept can be used for both two and three dimensional structures.

6.2 Locations and Numbers of Substructures

Locations and numbers of substructures are very important in assessing structural health using the Kalman filter-based concepts. The predictive behavior of all the algorithms developed by the team improves significantly if the defects are in the or close to the substructure. To assess large structural systems, the use of multiple substructures at different locations becomes an attractive alternative. This will make defects close to a substructure. It is to be noted that the unknown excitation force must be applied to a node (primary node) in the substructure. For multiple substructures, multiple excitations are required. For seismic loading, all nodes are the primary node. Thus, no additional effort is necessary to identify large structural systems excited by the seismic loading.

7. Conclusions

Structural health assessment and monitoring (SHAM) has been an evolving area of research over several decades. Verification and validation of the most recent mathematical model-based SHAM concepts face significant challenges dealing with large structural systems. The authors and their research team have been involved in developing various concepts and strategies for economic and accurate SHAM of large realistic engineering structures. They showed that the system identification-based concept can be used to detect defects at the element level and their severity using the procedures they developed. Based on their experience, the commonly encountered challenges associated with measurement uncertainties and nonlinearities have been discussed in this paper. Emphasis has been given on the need of physics-based data processing and signal conditioning generally not discussed in the literature. Additional challenges also expected to be encountered during inspection of large structures are briefly discussed in this paper.

References

1. Wang, D. and Haldar, A. (1994), "An Element Level SI with Unknown Input Information," J. Engrg. Mech., ASCE, Vol. 120, No. 1, pp. 159-176.
2. Wang, D. and Haldar, A. (1997), "System Identification with Limited Observations and Without Input," ASCE J. Engrg. Mech., Vol. 123, No. 5, pp. 504-511.
3. Ling, X. and Haldar, A. (2004), "Element Level System Identification with Unknown Input with Rayleigh Damping," J. Engrg. Mech., ASCE, Vol. 130, No. 8, pp. 877-885.
4. Katkhuda, H., Martinez-Flores, R., and Haldar, A. (2005), "Health Assessment at Local Level with Unknown Input Excitation," J. Struct. Engrg., ASCE, Vol. 131, No. 6, pp. 956-965.
5. Katkhuda, H. and Haldar, A. (2008), "A Novel Health Assessment Technique with Minimum Information," Struct. Cont. & Health Monitoring, Vol. 15, No. 6, pp. 821-838.
6. Das, A. K. and Haldar, A. (2010), "Structural Integrity Assessment under Uncertainty for Three Dimensional Offshore Structures," Int. J. Terraspace Sc. and Engrg. (IJTSE), Vol. 2, No. 2, pp. 101-111.
7. Das, A. K., Haldar, A. and Chakraborty, S. (2012), "Health Assessment of Large Two Dimensional Structures using Minimum Information – Recent Advances," Advances in Civil Engrg., 2012, Article ID 582472, doi:10.1155/2012/582472.
8. Das, A. K. and Haldar, A. (2012), "Health Assessment of Three Dimensional Large Structural Systems – A Novel Approach," Life Cycle Reliability and Safety Engineering, Vol. 1, Issue 1, pp. 1-14.
9. Al-Hussein, A., and Haldar, A. (2015), "A Novel Unscented Kalman Filter for Health Assessment of Large Structural Systems with Unknown Input," Journal of the Engineering Mechanics Division, ASCE, Vol. 141, No. 7, DOI: 10.1061/(ASCE)EM.1943-7889.0000926 .
10. Maybeck, P. S., (1979), "Stochastic Models, Estimation, and Control Theory," Academic Press, Inc., UK.
11. Das, A. K. (2012). "Health Assessment of Three Dimensional Large Structural Systems using Limited Uncertain Dynamic Response Information," PhD Dissertation, University of Arizona, Tucson, Arizona. Volume 2012, Article ID 582472.
12. Yang, J. N., Pan, S., and Lin, S. (2007), "Least-Squares Estimation with Unknown Excitations for Damage Identification of Structures," J. Engrg. Mech., Vol. 133, No. 1, pp. 12-21.
13. Yang, J. N. and Lin, S. (2005), "Identification of Parametric Variations of Structures Based on Least Squares Estimation and Adaptive Tracking Technique," J. Engrg. Mech., Vol. 131, No. 3, pp. 290-298.
14. Yang J. N., Lin, S., Huang, H.W., and Zhou, L. (2006), "An Adaptive Extended Kalman Filter for Structural Damage Identification," J. Struct. Cont. and Health Monitoring, Vol. 13, pp. 849–867.
15. Yang, J. N. and Huang, H. (2007), "Sequential Non-linear Least-square Estimation for Damage Identification of Structures with Unknown Inputs and Unknown Outputs," Int. J. Non-lin. Mech., Vol. 42, pp. 789-801.
16. Wang, X. J. and Cui, J. (2008), "A Two-step Method for Structural Parameter Identification with Unknown Ground Motion," The 14th World Conference on Earthq. Engrg., Beijing, China.
17. Choi, Y. M., Cho, H. N., Kim, Y. B., and Hwang, Y. K. (2001), "Structural Identification with Unknown Input Excitation," KSCE J Civil Engrg., Vol. 5, No. 3, pp. 207-213.
18. Chen, J. and Li, J. (2004), "Simultaneous Identification of Structural Parameters and Input Time History from Output-only Measurements, Comput. Mech., Vol. 33, pp. 365-374.

19. Chase, J. G., Begoc, V., and Barroso, L. R. (2005b), "Efficient Structural Health Monitoring for Benchmark Structure using Adaptive RLS Filters," Comp. and Struct., Vol. 83, pp. 639-647.
20. Chase, J. G., Spieth, H. A., Blome, C. F., and Mandler, J. B. (2005a), "LMS-Based Structural Health Monitoring of a Non-linear Rocking Structure," Earthquake Engrg. and Struct. Dyn., Vol. 34, pp. 909-930.
21. Garrido, R. and Rivero-Angeles, F. J. (2006), "Hysteresis and Parameter Estimation of MDOF Systems by a Continuous-Time Least-Squares Method," J. Earthquake Engrg., Vol. 10, No. 2, pp. 237-264.
22. Sandesh, S. and Shankar, K. (2009), "Time Domain Identification of Structural Parameters and Input Time History using a Substructural Approach," Int. J. Struct. Stability and Dyn., Vol. 9, No. 2, pp. 243-265.
23. Kun, Z., Law, S. S., and Zhongdong, D. (2009), "Condition Assessment of Structures under Unknown Support Excitation," Earthq. Eng. & Eng. Vib., Vol. 8, pp.103-114.
24. Xu, B., He, J., Rovekamp, R., and Dyke, S. J. (2011), "Structural Parameters and Dynamic Loading Identification from Incomplete Measurements: Approach and Validation," Mech. Sys. and Sig. Process., doi:10.1016/j.ymssp.2011.07.008.
25. Lu, Z. R. and Law, S. S. (2007), "Identification of System Parameters and Input Force from Output Only," Mech. Sys. and Sig. Process., Vol. 21, pp. 2099-2111.
26. Perry, M. J. and Koh, C. G. (2008), "Output-only Structural Identification in Time Domain: Numerical and Experimental Studies," Earthq. Engrg. and Struct. Dyn., Vol. 37, pp. 517-533.
27. Koh, C. G. and See, L. M. (1994), "Identification and Uncertainty Estimation of Structural Parameters," J. Engrg. Mech., Vol. 120, No. 6, pp. 1219-1236.
28. Yang, J. N., Huang, H., and Lin, S. (2006), "Sequential Non-linear Least-square Estimation for Damage Identification of Structures," Int. J. Non-lin. Mech., Vol. 41, pp. 124-140.
29. Ghosh, S., Roy, D., and Manohar, C.S. (2007), "New Forms of Extended Kalman Filter via Transversal Linearization and Applications to Structural System Identification," Comp. Methods in App. Mech. and Engrg., Vol. 196, pp. 5063-5083.
30. Liu, X., Escamilla-Ambrosio, P. J., and Lieven, N. A. J. (2009), "Extended Kalman Filtering for the Detection of Damage in Linear Mechanical Structures," J. Sound and Vib., Vol. 325, pp. 1023-1046.
31. Huang, N. E., Shen, Z., Long, S. R., Wu, M. C., Shih, H. H., Zheng, Q., Yen, N-C., Tung, C. C., and Liu, H. H. (1998), "The Empirical Mode Decomposition and the Hilbert Spectrum for Nonlinear and Non-stationary Time Series Analysis," Proc. R. Soc. Lond. A., Vol. 454, pp. 903-995.
32. Vo, P. H. and Haldar, A. (2003), "Post Processing of Linear Accelerometer Data in System Identification," J. Struct. Engrg., Vol. 30, No. 2, pp. 123-130.
33. Martinez-Flores, R. (2005), "Damage Assessment Potential of a Novel System Identification Technique – Experimental Verification," PhD Dissertation, Department of Civil Engineering and Engineering Mechanics, University of Arizona, Tucson, Arizona.
34. Vo, P. and Haldar, A. (2004), "Health Assessment of Beams Experimental Investigation," J. Struct. Engrg., Vol. 31, No. 1, pp. 23-30.
35. Martinez-Flores, R., Katkhuda, H., and Haldar, A. (2008), Structural Performance Assessment with Minimum Uncertainty-Filled Information, Int. J. Performability Engrg., Vol. 4, No. 2, pp. 121-140.
36. Wu, M. and Smyth, A.W. (2007), "Application of the Unscented Kalman Filter for Real-time Nonlinear Structural System Identification," Structural Control Health Monitoring, Vol. 14, No. 7, pp. 971-990.
37. Haldar, A. and Das, A. (2010). "Prognosis of Structural Health: Non-Destructive Methods," International Journal of Performability Engineering Vol. 6, No. 5, pp. 487-498.
38. Kerschen, G., Worden, K., Vakakis, A. F., and Golinval, J. C. (2006), "Past, Present and Future of Nonlinear System Identification in Structural Dynamics," Mech. Sys. and Sig. Processing, Vol. 20, No. 3, pp. 505-592.
39. Julier S. J., Uhlmann, J. K., Durrant-Whyte, H. F. (1995), "A new Approach for Filtering Nonlinear Systems," Proceeding of the American Control Conference, Seattle, Washington, pp. 1628-1632.
40. Wan, E. A., Van der Merwe, R. (2000), "The Unscented Kalman Filter for Nonlinear Estimation," Proceedings of Symposium on Adaptive Systems for Signal Processing, Communication and Control (AS-SPCC), Lake Louise, Alberta, Canada.

Life Cycle Reliability and Safety Engineering
Vol.4 Issue 2 (2015) 13-19

Damage Quantification in Building Structures using Bayesian Inference: Hybrid Approaches

Kanta Prajapat and Samit Ray-Chaudhuri*
[1]*PhD Student, Dept. of Civil Engg., Indian Institute of Technology Kanpur, UP - 208016, India.*
[2]*Associate Professor, Dept. of Civil Engg., Indian Institute of Technology Kanpur, UP - 208016, India*
kanta@iitk.ac.in, samitrc@iitk.ac.in (Corresponding Author)

Abstract

It is widely known that in civil structures, the modal properties of higher modes are difficult to obtain using ambient excitations. This is because under ambient conditions, sufficient energy is not available to reasonably excite the higher modes. This scarcity of data coupled with the problem associated with large dimensionality of the uncertain parameter space often make the damage quantification a challenging job. In this paper, damage quantification in a numerically simulated 16-storey and a 6-storey moment resisting frame is done under Bayesian framework with different approaches. In the first approach, a two-stage damage quantification approach is employed where the stages differ with the choice of starting value of Markov Chain. In the second approach, the issue of lack of appropriate data is resolved by modifying the structure with adding some known masses such that its natural frequencies and mode shapes get changed. Therefore, more data can be acquired from the same structure to improve the efficiency of the updation algorithm. Results show that both approaches seem to be promising in model updation/damage quantification based on only a few lower mode shape data.

Keywords: Bayesian statistics; Modal parameters; Damage; Mass modification;

1. Introduction

From past several decades, model updating has been widely used successfully in various engineering applications to develop better mathematical models. In recent years, model updating is becoming an integral part of damage detection and quantification of structures. This paper focuses on damage quantification in building structures using model updating. Both deterministic and statistical approaches have been used for model updation in the past. However, many factors such as noise associated with experimental measurements and incompleteness of experimental measurements may lead to a non-unique deterministic solution of the inverse problem. Therefore, it is hard to rely on the deterministic approach for model updation. Bayesian approach for model updation of civil structures has been satisfactorily used in past by many researchers. This approach can deal with ill-conditioning and non-uniqueness issues of deterministic approach. A significant work has been done to develop updated model using both modal parameters and time history data (e.g. acceleration) of a given structure [1, 3, 4, 5, 8, 10, and 11]. Particular emphasis was placed on localizing and quantifying the existing damage in structures along with focusing on the various issues of Bayesian model updating.

Sohn and Law [14] applied Bayesian probabilistic approach to localize and quantify the amount of damage in structures employing incomplete and noisy modal data. A novel approach for online health monitoring and damage assessment of structures using Bayesian probabilistic measures was presented by Vanik et al. [15]. In this approach, system identification was first performed in undamaged state and then continuous monitoring cycles were run to detect the damage in the structure. Beck and Yuena [2] emphasized the need of appropriate model class selection by examples of some linear and non-linear structural systems. Muto and Beck [9] employed Bayesian approach for updation and class selection for Masing hysteretic structural models. Using vibration measurements (modal data) on a steel cantilever beam a Bayesian inference based damage localization technique was presented by Huhtala and Bossuyt [6]. Simoen et al. [13] studied damage assessment of a slice of 7-story RC building using Bayesian uncertainty quantification technique. Damage detection in plate type structures was studied by Kurata et al. [7].

Employing Bayesian approach for a problem with large number of unknown parameters and limited number of data sets available for defining the likelihood function may not yield reasonable

estimation of unknown parameters. Therefore, instead of taking all structural parameters as unknown for damage quantification of the structure, in this work, first it is assumed that the damage locations are identifiable using a fundamental mode shape and its derivative based approach. Then the quantification of damage at only the identified locations is done using modal data of a few lower modes.

Two different techniques are employed in this work for this purpose. In first technique, damage is quantified in two stages. The two stages differ in regard of the chosen initial value in Markov chain and relate with each other with the fact that the initial value for the second stage is chosen depending on the results of the first stage. If only the fundamental mode data is used for model updation or damage quantification, one may get substandard results due to the lack of data in updation algorithm. Therefore, in the second approach, a mass modification technique is employed and some known masses are added to the structure such that a different mode shape from the same structure can be obtained. Then these mode shapes along with the mode shape of the original structure are used to quantify damage in the structure. Metropolis-Hasting algorithm for sampling in Markov Chain Monte Carlo environment is employed for both the techniques proposed.

2. Bayesian Model Updating

Bayesian model updating is a statistical tool to minimize the error in the outcomes of a physical process from its mathematical model. The following relation is employed for Bayesian model updating schemes:

$$Posterior\ distribution \propto Likelihood \times Prior\ distribution \quad (1)$$

Prior distribution for any model parameter is determined based on the available knowledge about the parameter. The term likelihood is a probabilistic function which relates the plausibility of getting the observed outcome of the physical process for a given value of a parameter of the mathematical model. Finally, the term posterior distribution gives a more favorable distribution for the model parameters by operating the likelihood function on the prior and thus, refining the prior distribution to posterior.

Mathematically, if the outcome of the mathematical model is expresses as $\underline{x}(i;\underline{a})$ for some model class with model parameter vector $\underline{a}$ and system input Z_i for $i = 1,2...n$ time steps for each time step then the experimental/real time outcome of the physical process can be related to $\underline{x}(i;\underline{a})$ as:

$$\underline{y}(i) = \underline{x}(i;\underline{a}) + \underline{e}(i;\underline{a}) \qquad i = 1,2,...n \quad (2)$$

Equation 2 comprises of a deterministic part $\underline{x}(i;\underline{a})$ and a random part $\underline{e}(i;\underline{a})$ (error or difference of mathematical and experimental/real time outcome). The random part $\underline{e}(i;\underline{a})$ can be represented with some probabilistic distribution. If $\underline{e}(1;\underline{a}),\underline{e}(2;\underline{a}),...\underline{e}(n;\underline{a})$ represent the error distribution functions for each time step, then the error probability model for n time steps can be represented as some function of these error distribution functions.

$$p(E^n \mid \underline{\sigma}) = h_n(\underline{e}(1;\underline{a}),\underline{e}(2;\underline{a}),...\underline{e}(n;\underline{a});\underline{\sigma}) \quad (3)$$

where $\underline{\sigma}$ is a vector of variances of $\underline{e}(1;\underline{a}),\underline{e}(2;\underline{a}),...\underline{e}(n;\underline{a})$. Therefore, the total uncertain parameter vector comprises of the uncertain model parameters vector $\underline{a}$ and the uncertain variances vector $\underline{\sigma}$ and can be represented with a vector $\underline{\alpha}$ as shown in Equation 4.

$$\underline{\alpha} = [\underline{a}^T, \underline{\sigma}^T]^T \quad (4)$$

Given the error probability model as defined in Equation 3, the outcome probability model conditioned on the parameter vector $\underline{\alpha}$ and input Z^n can be defined as

$$\begin{aligned} p(Y^n \mid \underline{\alpha}, Z^n) &= f_n(\underline{y}(1),...,\underline{y}(n);\underline{\alpha},Z^n) \\ &= h_n(\underline{y}(1) - \underline{x}(1;\underline{a}),...,\underline{y}(n) - \underline{x}(n;\underline{a});\underline{\sigma}) \end{aligned} \quad (5)$$

if $\pi(\underline{\alpha})$ represents the prior joint distribution of unknown parameters, then the joint probability of outcome probability model with parameter vector $\underline{\alpha}$ conditioned on input Z^n can be written as

$$p(Y^n \underline{\alpha} \mid Z^n) = f_n(\underline{y}(1),...,\underline{y}(n);\underline{\alpha},Z^n)\pi(\underline{\alpha}) \quad (6)$$

Integrating Equation (6) over the space $S_{\underline{\alpha}}$ of parameter vector $\underline{\alpha}$ the marginal distribution of outcome probability model conditioned on input Z^n can be given as

$$p(Y^n \mid Z^n) = \int_{S_{\underline{\alpha}}} f_n(Y^n;\underline{\alpha},Z^n)\pi(\underline{\alpha})d\underline{\alpha} \quad (7)$$

Now, if D represents a dataset of input Z^m and output Y^m for 'm' time steps, then mathematically the relation $Posterior\ distribution \propto Likelihood \times Prior\ distribution$ can be expressed as

$$\begin{aligned} p(\underline{\alpha} \mid Y^m) &= kp(Y^m \mid \underline{\alpha},Z^m)\pi(\underline{\alpha}) \\ &= kf_m(Y^m;\underline{\alpha},Z^m)\pi(\underline{\alpha}) \end{aligned} \quad (8)$$

where

$$k^{-1} = p(Y^m \mid Z^m) \quad (9)$$

Thus, with the information of the prior distributions and experimental outcome, one can obtain a more favorable posterior distribution of unknown parameters employing Bayesian approach. With the increased number of unknown parameters, the dimensionality of parameter space S_{α} increases. This makes the analytical evaluation of Equation 7 difficult. Therefore, in this work Markov Chain Monte Carlo (MCMC) simulation is employed to draw samples from a higher dimensional joint distribution. A brief discussion on Metropolis-Hasting sampling algorithm is presented in the next section, which is used in this work to draw samples under MCMC environment.

3. Metropolis-Hasting Algorithm

A Markov chain is said to be reached stationary distribution when it satisfies the following equation:

$$\omega(x)q(x,y) = \omega(y)q(y,x) \tag{9}$$

In Equation (9), ω is the target distribution and q represents the transitional probability distribution function which gives the transition probability from one realization of random value to other realization. In case when the exact transition probability function is not known, the transition probability function (often known as proposal distribution) has to be assumed. In such case, Equation (9) becomes

$$\omega(x)q(x,y) > \omega(y)q(y,x) \tag{10}$$

Metropolis-Hasting sampling algorithm provides a way to reach the stationary distribution in Markov chain by introducing a probability of move $\eta(x,y)$ as given by the following relation:

$$\eta(x,y) = \min\left[\frac{\omega(y)q(y,x)}{\omega(x)q(x,y)},1\right],\ \omega(x)q(x,y) > 0$$
$$= 1 \qquad \text{otherwise} \tag{11}$$

So, the proposed sample from the proposal distribution is accepted with a probability $\eta(x,y)$ to achieve the target distribution ω.

4. Proposed Approaches

The use of damage localization techniques prior to damage quantification in Bayesian model updation algorithms minimizes the problem of high dimensional variable space in Bayesian framework. Due to the space constraints, the fundamental mode shape and its derivative-based approach, which is employed in this work for damage localization, is not discussed here. A detailed study on this approach can be found in Roy and Ray-Chaudhuri [12].

As the initial value to start the Markov chain may influence the convergence of chain and results when proposal distribution is not chosen carefully. Therefore, in the first approach damage quantification is done in two stages and the two stages differ in the choice of initial value to start the Markov chain. In the first stage, any arbitrary values of unknown parameters are chosen to start the chain; but in the second stage the starting values are chosen as the resulting mean of the unknown parameters from the first stage. Results from the second stage showed an improvement over the results from the first stage. Figure 1 shows the complete algorithm.

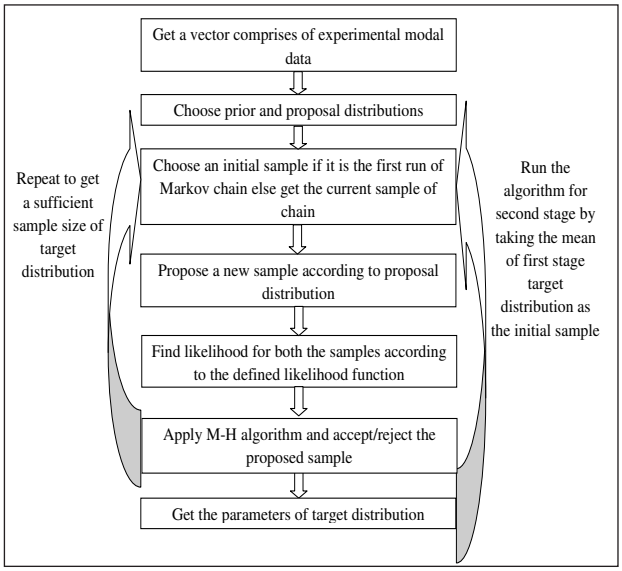

Figure 1: Algorithm for two stage approach

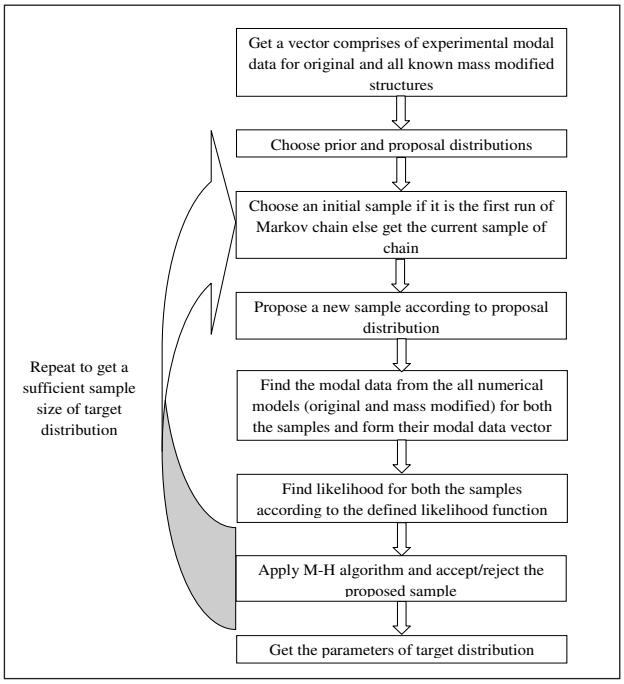

Figure 2: Algorithm for mass modification approach

When only the fundamental mode shape data is used for damage quantification, results may deteriorate because of the lack of data in defining the likelihood function. The second approach proposed in this work deals with this problem by modifying the original structure through adding some known masses to it. The masses are added in such a way that they are effective in changing the mode shapes of the structure without altering its stiffness. Therefore, instead of having only a single mode shape data (as only fundamental mode shape is used), multiple mode shape data for fundamental mode, one with each mass modification can be obtained from the same structure. Then model updation is done employing all these data. The complete algorithm is shown in Figure 2.

5. Numerical Modeling and Results

5.1 Two-stage Approach

For the first approach, a 16-storey 3-bay moment resisting frame is modeled in OpenSees. This analytical model is chosen as the base model. Damage is then inserted at several places in this base structure by reducing the stiffness of the members to simulate a damaged structure. Figure 3 shows the schematic diagram of the frame with damage locations. Five different members at different places are damaged by reducing their stiffness with different reduction parameters (named as theta1, theta2 etc.) as given in Table 1. These reduction parameters are then taken as unknown parameters and tried to obtain through Bayesian approach. The unknown parameters are assumed as statically independent. Exponential distribution with mean = 1 is taken as the prior distribution and Gamma distribution is chosen for the proposal distribution. Markov chain is run for a total of 1000 simulation for each unknown parameter. Modal data (Frequencies and mode shapes of first three modes) from the known damaged structure is treated as experimental/real time outcome of the actual physical model. Likelihood is taken as the product of probability density of self normalized elements of the error vector (difference between the data from known damaged structure and data from each simulated structure). The probability density function for each element is assumed as Gaussian distribution with zero mean and variance of two. Metropolis-Hasting algorithm is adopted to simulate the posterior distribution. A burning period of 200 and a thinning parameter of 5 are used in Markov chain to get the final posterior distribution.

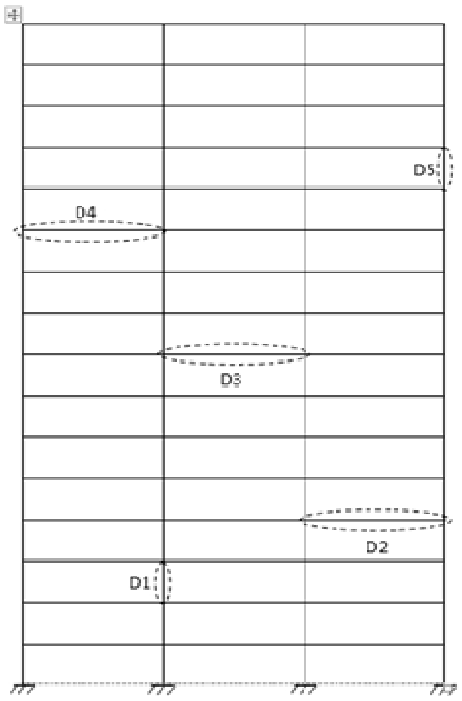

Figure 3: Schematic diagram of 16-storey model with damage locations

In this approach, damage quantification is done in two stages. As the starting value of Markov chain influences its convergence when proposal distribution is not chosen with care. The proposed two-stage approach proves to be beneficial in such scenario. At first stage, any arbitrary value of unknown parameters

Table 1: Actual value for different parameters

Parameter	Actual value
theta1	0.713
theta2	0.84
theta3	0.732
theta4	0.624
theta5	0.806

Table 2: Comparison of both stages results in two stage approach

First stage		Second stage	
Posterior mean	% Deviation with actual	Posterior mean	% Deviation with actual
0.795	11.5	0.687	3.6
1.0	19.04	0.836	0.48
0.816	11.47	0.732	0.0
0.757	21.31	0.621	0.48
0.849	5.33	0.816	1.24

are chosen to start the chain and posterior distributions for the unknown parameters are obtained. In second stage, instead of starting the chain with any arbitrary value the mean of posterior distributions from the first stage, are chosen as the starting value to run the Markov chain.

Figure 4 shows the joint posterior distribution of different parameters obtained after the second stage. It is clear from this figure that the obtained posterior is in a range which is very near to the actual value of the parameter instead of a broad range of chosen prior distribution. The mean of the posterior distribution is taken as the parameter value in each stage. Comparison of results from the first and second stage with the actual values of unknown parameters is shown in Table 2. It can be observed from Table 2 that the results improve significantly in second stage.

5.2 Mass Modification Approach

To illustrate the mass modification approach a 6-storey single bay frame is modeled in OpenSees. Damage is introduced by reducing the stiffness of all beams with a stiffness reduction parameter (k_b) and all columns with another stiffness reduction parameter (k_c). Therefore, the problem deals with the determination of two unknown parameters k_b and k_c (taken equal as given in Table 3). Here also the unknown parameters are assumed as statically independent as in the two-stage approach. All other parameters in MCMC algorithm like prior distribution, likelihood function, burning period, thinning parameter etc. are also assumed to be same as in the two-stage approach. The difference with the two stage approach is that here the modal data from the known damaged structure which is taken as experimental/ real time outcome of the actual physical model comprises of frequency of first two modes and mode shape data of fundamental mode only. Therefore, additional fundamental mode shape data is acquired by adding known masses to the structure such that the mode shape of the structure gets changed. The structure is modifies two times with known masses. Then all this data (with or without mass modification)

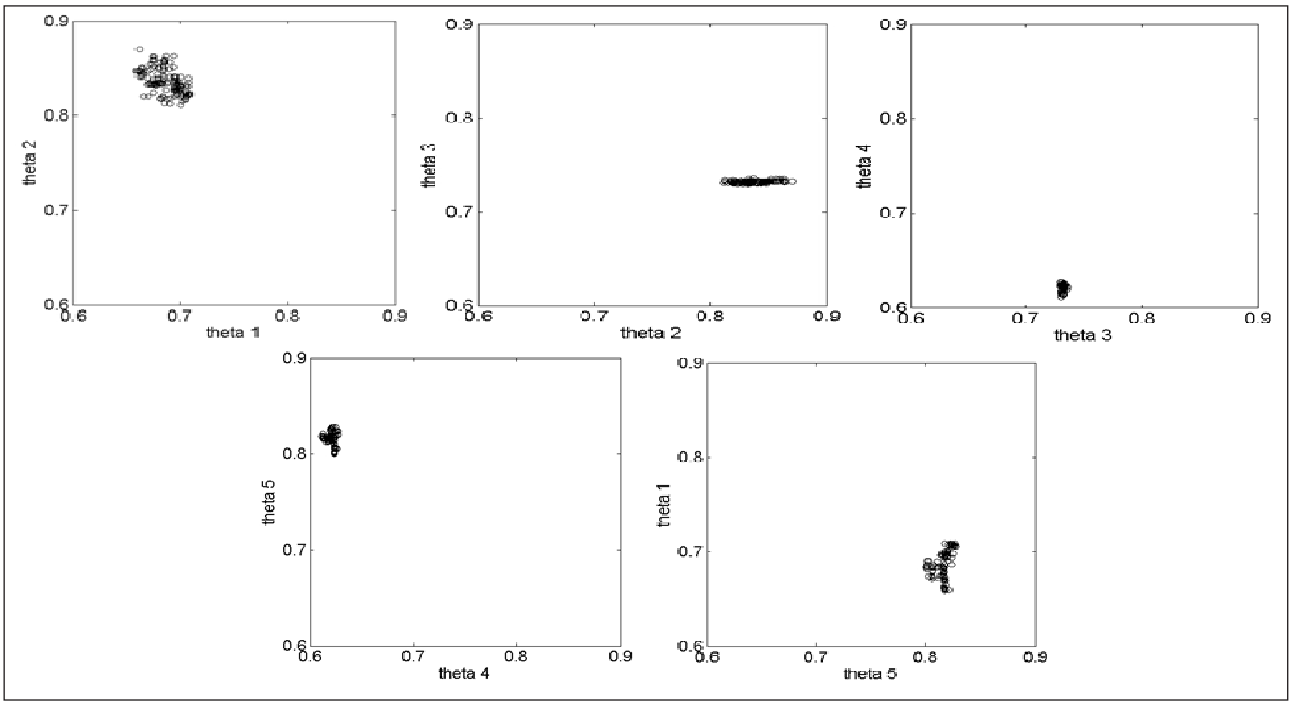

Figure 4: Posterior distributions in two stage approach

Table 3: Mass modification approach results for 6-storey single bay frame

Parameter	Actual value	Posterior mean (without noise)	Posterior mean (with noise)	% deviation with actual (without noise)	% deviation with actual (with noise)
kc	0.84	0.888	0.955	5.4	12.04
kb	0.84	0.873	0.849	3.78	1.07

is considered in making the likelihood function. For each simulation of unknown parameters modal data is obtained for each known mass modified structure and the original damaged structure to incorporate in the likelihood function in the same way as done in the two-stage approach.

To study the effect of noise in experimental data a Gaussian white noise with signal-to-noise ratio (SNR) 50 is added to the simulated experimental data. Table 3 shows the results for with and without noise. This is clear from Table 3 that the proposed approach is promising in damage quantification when only fundamental mode shape data is available for updation. Also, the proposed approach is capable of dealing with data contaminated with noise. Results show that the percentage deviation from the actual parameter values is within acceptable limit for both with and without noise data.

To see the effectiveness of proposed approach with increased number of unknown parameters the 16-storey 3-bay moment resisting frame of two stage approach is also considered here. The loactions of unknown parametrs are taken as known at priory in this approach also and same loactions are chosen for unknown parameters as in the case of two stage approach. The actual value of unknown parameters is taken as unity. The starting value for unknown parameters is chosen as 1.5. Other parametrs are taken as same as in the two stage approach. Simulated experimental data is obtained by modifying the structure three times with known masses such that different modal data can be acquired for each mass modifiction. Modal data of first three modes are considered as simulated experimental data. Table 4 shows the results in terms of posterior mean of the unknown parameters with their percentage deviation from the actual value of the parameters. It can be observed from Table 4 that except for two or three parameters the percentage deviation from the actual value is quite high. The approach does not perform efficiently when there is a large number of unknown parameters. Instead of taking only mass modification approach a combine two stage and mass modification approach can be employed to get better results in future.

Table 4: Mass modification approach results for 16-storey 3-bay moment resisting frame

Parameter	Actual value	Posterior mean	% deviation with actual
theta1	1.0	1.10	9.0
theta2	1.0	1.17	14.53
theta3	1.0	1.07	6.5
theta4	1.0	0.75	33.3
theta5	1.0	1.64	39.02

6. Conclusions

Two different approaches are proposed for damage quantification in civil structures. Localization of damage before quantification helps in improving the efficiency of MCMC algorithm by reducing the dimension of the unknown parameter space. The first approach is useful when not much information about the prior distribution and proposal distribution can be acquired. Results of second stage in first approach demonstrate a good improvement over the first stage. The second approach is promising when only fundamental mode shape or very few lower mode shapes data is available for updation. The mean of posterior distributions are found in good agreement with actual value of parameters. Also, the approach performed well in case of noisy data. The approaches proposed herein are however needed to be verified for actual noisy data from existing structures and with more number of unknown parameters.

References

1. Beck J. L. and Katafygiotis L. S., "Updating of a model and its uncertainties utilizing dynamic test data" Computational Stochastic Mechanics, Springer, pp. 125–136, 1991.
2. Beck J. L. and Yuena K. V., "Model selection using response measurements: Bayesian probabilistic approach" Journal of Engineering Mechanics, Vol 130, No. 2, pp. 192–203, 2004.
3. Cheung S. H. and Beck J. L., "Bayesian model updating using hybrid monte carlo simulation with application to structural dynamic models with many uncertain parameters" Journal of Engineering Mechanics, Vol 135, No. 4, pp. 243–255, 2009.
4. Cheung S. H. and Beck J. L., "Calculation of posterior probabilities for bayesian model class assessment and averaging from posterior samples based on dynamic system data." Computer-Aided Civil and Infrastructure Engineering, Vol 25, No. 5, pp. 304–321, 2010.
5. Ching J., Muto M., and Beck J. L., "Bayesian linear structural model updating using gibbs sampler with modal data" Proceedings of the 9th International Conference on Structural Safety and Reliability, Millpress, pp. 2609–2616, 2005.
6. Huhtala A. and Bossuyt S., "A bayesian approach to vibration based structural health monitoring with experimental verification" Journal of Structural Mechanics, Vol 44, No. 4, pp. 330–344, 2011.
7. Kurata M., Lynch J. P., Law K. H., and Salvino L. W., "Bayesian Model Updating Approach for Systematic Damage Detection of Plate-Type Structures" Springer, 2012.

8. Moaveni B., Barbosa A. R., Conte J. P., and Hemez F. M., "Uncertainty analysis of modal parameters obtained from three system identification methods" Proceedings of the XXVth International Conference on Modal Analysis (IMAC), Orlando, FL, USA, 2007.
9. Muto M. and Beck J. L., "Bayesian updating and model class selection for hysteretic structural models using stochastic simulation" Journal of Vibration and Control, Vol 14, No. 1-2, pp. 7–34, 2008.
10. Panagiotou M., Restrepo J. I., and Conte J. P., "Shake-table test of a full-scale 7-story building slice. phase i: Rectangular wall" Journal of Structural Engineering, Vol 137, No. 6, pp. 691–704, 2010.
11. Papadimitriou C., Beck J. L., and Katafygiotis L. S., "Updating robust reliability using structural test data" Probabilistic Engineering Mechanics, Vol 16, No. 2, pp. 103–113, 2001.
12. Roy K. and Ray-Chaudhuri S., "Fundamental mode shape and its derivatives in structural damage localization" Journal of Sound and Vibration, Vol 332, No. 21, pp. 5584–5593, 2013.
13. Simoen E., Moaveni B., Conte J. P., and Lombaert G., "Uncertainty quantification in the assessment of progressive damage in a 7-story full-scale building slice" Journal of Engineering Mechanics, Vol 139, No. 12, pp. 1818–1830, 2013.
14. Sohn H. and Law K. H., "A bayesian probabilistic approach for structure damage detection" Earthquake engineering and structural dynamics, Vol 26, No. 12, pp. 1259–1281, 1997.
15. Vanik M. W., Beck J. L., and Au S. K., "Bayesian probabilistic approach to structural health monitoring" Journal of Engineering Mechanics, Vol 126, No. 7, pp. 738–745, 2000.

Life Cycle Reliability and Safety Engineering
Vol.4 Issue 2 (2015) 20-27

Metamodeling of nonstationary uncertain structural systems based on wavelet transform decomposition

M.D. Spiridonakos & E.N. Chatzi*
Institute of Structural Engineering, D-BAUG, ETH Zurich, Switzerland
Email: chatzi@ibk.baug.ethz.ch

Abstract

The problem of estimating reduced complexity metamodels for the accurate representation of computationally costly numerical models with time-varying properties and uncertain input parameters is addressed in this work. The introduced metamodeling method is based on the discrete wavelet transform of the dynamic response signals. The coefficients of this transform are defined as random parameters, in this way accounting for the inherent system uncertainties. These random coefficients are expanded onto a polynomial chaos basis resulting into a representation that is fully described via a finite number of deterministic projection coefficients. The effectiveness of the proposed methodology is illustrated through its application on the metamodeling of a finite element model of a simply supported beam featuring a moving mass, simulating the vehicle crossing problem. The attained results demonstrate the efficiency of the proposed methodology for accurate simulation of the involved time-varying dynamics.

Keywords: *Metamodeling; nonstationary; uncertainty; polynomial chaos basis; discrete wavelet transform.*

1 Introduction

Due to reasons relating to manufacturing or construction, ageing processes, loading and boundary conditions, measurement errors, and even inability of the numerical model to account for the physics of the system, almost every structural system is characterized by uncertainty. The propagation of uncertainty through such a system gives rise to corresponding uncertainties of the structural dynamics and, in turn, to the overall behaviour of the structure. The problem becomes even more pronounced when the system at hand is described by time varying dynamics [1, 2, 3], thus furthering the complexity of the governing laws involved. In view of the above, the international research community has underlined, the necessity for developing dynamic structural models able to additionally encompass the aforementioned uncertainties [4].

In an effort to accurately model structural systems, engineers will most commonly resort to the use of Finite Element (FE) models. Indeed, the FE method is known to offer a strong tool for the computational modelling of large engineering systems with the method been extensively used in a number of civil, mechanical and aeronautical applications [5, 6]. Moreover, the recently introduced spectral stochastic FE method comprises the first important step for the extension of the classical FE method toward stochastic implementations, including that of uncertainty propagation via relevant FE models [7]. This approach has been adopted by several researchers and has undergone several important developments and improvements over the last decade [8, 9, 10]. The method relies upon the expansion of the uncertain input parameters onto a suitably defined Polynomial Chaos (PC) basis and the description of the model output as a random parameter spanned onto the same prescribed stochastic basis through a set of unknown deterministic coefficients of projection [11].

Although the PC expansion approach has been proved to constitute a computationally efficient methodology for describing uncertainty propagation using stationary models [7, 12], its extension to the nonstationary case is not straightforward. Nonstationary, or else time-varying systems, i.e., systems with properties that are changing with time, may be encountered in a plethora of structural applications, ranging from train-bridge systems to wind turbines and aerospace. Although oftentimes nonstationarity may be neglected or overlooked for the purposes of simplicity, this would not be pretend, or to the side of safety for the aforementioned examples as well as a number of other sys-tems where nonstationarity has to be taken into account in favour of refining modelling accuracy and obtaining a better insight into the involved dynamics.

The main complexity in dealing with such systems is that due to their intrinsic time-variability, the corresponding numerical models used for their representation are described through differential equations with time-varying parameters, rendering PC expansion an intricate task. On the other hand, employing a Monte-Carlo method for uncertainty quantification is not always an efficient option, since it is frequently linked to slow convergence, often requiring thousands of simulations even for static problems [13]. Thus, when requiring a mutliplicity of forward simulations, such as in design optimization, or model updating procedures obtained via time history loading of nonstationary systems, a simpler representation of the FE model should be considered, able to accurately reproduce the behavior of the nonstationary structure. In the work presented herein, an inverse approach is adopted employing nonstationary system identification techniques leading to the formulation of a "model" of the system's FE model, i.e., a metamodel.

Nonstationary identification methods so far met in the literature may be primarily classified into non-parametric and parametric [2]. In the first class, extensions of the classical frequency domain methods to the nonstationary case, such as the Short-Time Fourier Transform (STFT), the Wigner-Ville distribution and others, which may be grouped under the umbrella of the Cohen class of distributions [14], the Empirical Mode Decomposition (EMD), the Hilbert-Huang Transform (HHT) and wavelet expansion have been proposed [15, 16]. On the other hand, parametric methods are normally based on transfer function or state space models with time-varying parameters [17, 18] and, despite their ability to more efficiently account for nonstationarity, they come at the cost of considerable effort, user inference and expertise.

The main goal of the present study is the development of a metamodeling approach which is able to provide reduced representations of large numerical models for the accurate, yet computationally accelerated, prediction of their dynamic response. The metamodeling method introduced in this work is based on a sparse representation of the numerical model response signals via the Discrete Wavelet Transform (DWT) [19]. The coefficients of the wavelet decomposition are considered as random variables this way accounting for the uncertainty propagation through the numerical model. These random coefficients are expanded onto a suitably defined finite-dimensional PC basis resulting into a non-parametric representation that is fully described by the deterministic projection coefficients. The sparsity of the representation may be achieved by means of thresholding, while the projection coefficients are estimated by linear least squares fit.

It should be added that in previous work, the PCE has been coupled with nonlinear Autoregressive models for the metamodeling of the response of hysteretic nonlinear systems [20]. However, in the present study an additional challenge arises, since the time varying dynamics owed to the inherently changing system properties enter the system equations.

The remainder of the paper is organized as follows: in Section 2 the metamodeling problem is formally defined, and the metamodeling method based on the DWT and PC expansion is described. In Section 3 the introduced method is illustrated via a numerical case study, simulating a popular case for monitoring consideration, i.e., that of a vehicle crossing a bridge along with the main metamodeling results. Finally, the conclusions of this study are summarized in Section 4.

2 Discrete Wavelet Transform Metamodeling Method

Consider a time-varying structural system represented by a numerical model $\mathcal{M}$ that is characterized by a number of input parameters related to the properties of the modelled structure (mechanical and/or geometric). It is assumed that M of these parameters are subject to uncertainty and that they may be described by independent random variables gathered in a random vector $\boldsymbol{\xi} = [\xi_1, \xi_2, \ldots, \xi_M]^{\mathsf{T}}$.

As a result, the dynamic response of the numerical model to a given input excitation will be a random variable following a probability density function (pdf) with characteristics that depend on the corresponding pdf of the input variables and the mechanism of uncertainty propagation, that is

$$y[t, \boldsymbol{\xi}] = \mathcal{M}(x[1], x[2], \ldots, x[t], \boldsymbol{\xi}) \quad (1)$$

with $t = 1, 2, \ldots, T$ designating normalized by the sampling period discrete time, $x[t]$ the excitation input signal, $y[t, \boldsymbol{\xi}]$ the corresponding numerical model response signal, and $\boldsymbol{\xi}$ the M-dimensional vector of input random variables with known joint probability density function (pdf) $f(\boldsymbol{\xi})$.

Metamodeling refers to the process of identifying a reduced order and computational complexity representation $\widetilde{\mathcal{M}}$ of the large-scale numerical model $\mathcal{M}$. In the present work, a metamodel is sought for the representation of the time-varying dynamics of $\mathcal{M}$ and the accurate simulation of its time history loading response.

The classical PC expansion approach has been proved to be a computationally efficient way for describing the uncertainty propagation of time invariant problems [7, 8]. However, the dynamic response of a nonstationary numerical model is dependent upon both the pdf of the input parameters and time. Thus, for the case of non-parametric metamodeling the dynamic response of the numerical model at each distinct time instant *t*, should be treated as a separate output and a PC expansion should be performed, leading to a huge number of coefficients of projection.

In order to circumvent this difficulty a metamodeling method based on the DWT is introduced. Wavelets may be considered as particularly effective for representing highly transient phenomena such as the dynamic response of structural models – especially when these models are characterized by nonstationary properties and/or are subjected to nonstationary loading conditions like earthquakes and strong winds – while they also achieve high compression rates since they are able to perform signal decomposition at different resolutions and frequency bands.

It should be noted that parametric metamodels based on linear and non-linear autoregressive models with exogenous excitation with parameters expanded on PC basis (PC-ARX and PC-NARX models) have also been introduced recently in the metamodeling context by the authors of the present study [21, 22] in treating the issue of hysteretic nonlinear behavior and stochastic excitation. The challenge herein however lies in the fact that the nonstationarity is inherent to the system properties and not due to nonstationary excitation resulting into the onset of nonlinearities.

2.1 Discrete wavelet transform

Within the DWT framework an arbitrary signal $y[t]$ of finite energy may be casted into orthonormal wavelet basis as [23]:

$$y[t] = \sum_{\ell} \sum_{n} d_n^{\ell} \psi_n^{\ell}[t] \tag{2}$$

with d_n^{ℓ} denoting the coefficients of expansion, while $\psi_n^{\ell}[t]$ are the orthonormal wavelet basis functions obtained from the mother wavelet function $\psi[t]$ through the operations of dilation and translation:

$$\psi_n^{\ell}[t] = 2^{\ell/2} \psi[2^{\ell} t - n] \tag{3}$$

with ℓ and n designating the dilation and translation indices, respectively.

The DWT-based signal decomposition may be realized by means of a computationally efficient method known as Multi-Resolution Analysis (MRA) [19]. The MRA algorithm relates the DWT with the processes of multilevel low-pass and high-pass filtering followed by down sampling, which result in a hierarchically organized decomposition of the signal into a series of approximations and details (Figure 1) [23]. The approximation and detail coefficients may be calculated recursively as follows:

$$a_n^{\ell} = \sum_{m} h[m - 2n] a_m^{\ell-1} \tag{4a}$$

$$d_n^{\ell} = \sum_{m} g[m - 2n] d_m^{\ell-1} \tag{4b}$$

where $h[n]$ and $g[n]$ are the lowpass and highpass filters, respectively, defined by the wavelet and its scaling function. The DWT and the MRA algorithm are initialized with $a_n^0 = y[t]$ which defines the first level of the DWT. Iterating Equations (4a) and (4b) L times, the transformed signal consists of L sets of detail coefficients at $\ell = 1, \ldots, L (\boldsymbol{d}^1, \ldots, \boldsymbol{d}^L)$, and a set of approximation coefficients at level L $(\boldsymbol{a}^L)$. The number of levels L in the multi-resolution algorithm depends on the length of the signal. The MRA algorithm is schematically represented in Figure 1.

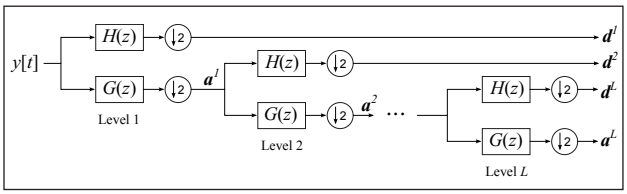

Figure 1: The Tree Algorithm of the Multi-Resolution Wavelet Analysis.

Normally the energy of the response signal $y[t]$ is concentrated in particular frequency bands related with the dynamics of the modelled structure and thus may be approximated by a sparse wavelet expansion.

The sparse representation is achieved by applying a threshold policy on the detail coefficients, keeping only a limited number of them [19].

The selection of the wavelet transform coefficients is presently based on the hard thresholding criterion, that is the wavelet coefficient is replaced by zero if its magnitude is less than a predifined threshold thr:

$$d_j^{\ell,\text{hard}} = \begin{cases} 0 & \text{if } |d_j^\ell| < \text{thr} \\ d_j^\ell & \text{if } |d_j^\ell| \geq \text{thr} \end{cases} \tag{5}$$

Hard thresholding is applied on a normalized, by the median of the finest detail wavelet coefficients d^1, version of the signal $y[t]$ [19].

The retained coefficients of the DWT may be collected in a complete vector of coefficients θ

$$\boldsymbol{\theta} = [\, \boldsymbol{a}^L,\, \boldsymbol{d}^{L,\text{hard}},\, \ldots,\, \boldsymbol{d}^{1,\text{hard}}\,]^\intercal \tag{6}$$

which is in turn used for the approximate reconstruction of the initial signal $y[t]$ by means of the inverse DWT.

In the case of an uncertain system, the response signal $y[t]$ will also depend on the uncertain input variables vector $\boldsymbol{\xi}$, as already shown in Eq. (1).

2.2 Polynomial chaos expansion

In order to approximate the numerical model dynamic response $y[t, \boldsymbol{\xi}]$ for every realization of $\boldsymbol{\xi}$ in an efficient way, the DWT coefficients θ should also be random variables depending on $\boldsymbol{\xi}$, that is $\boldsymbol{\theta}(\boldsymbol{\xi})$. The latter may be represented by a deterministic mapping which describes its relation with the input random variables. More specifically, assuming that the multilevel wavelet transform coefficients $\theta_i(\boldsymbol{\xi})$ have finite variance, they admit the following PC representation [11]:

$$\theta_i(\boldsymbol{\xi}) = \sum_{j=1}^{\infty} \theta_{i,j} \cdot \phi_{\boldsymbol{b}(j)}(\boldsymbol{\xi}) \tag{7}$$

where $\theta_{i,j}$ are unknown deterministic coefficients of projection, $\boldsymbol{b(j)}$ is the multi-indices of the multivariate polynomial basis, and $\phi_{\boldsymbol{b}(j)}$ are multivariate basis functions that are orthonormal with respect to the joint pdf of $\boldsymbol{\xi}$, that is:

$$E[\phi_{\boldsymbol{\alpha}}(\boldsymbol{\xi}), \phi_{\boldsymbol{\beta}}(\boldsymbol{\xi})] = \delta_{\boldsymbol{\alpha},\boldsymbol{\beta}} = \begin{cases} 1 & \text{for } \alpha = \beta \\ 0 & \text{otherwise} \end{cases} \tag{8}$$

Each pdf may be associated with a well known family of orthogonal polynomials. For instance, the normal distribution is associated with Hermite polynomials while the uniform distribution with Legendre. A list of the most common probability density functions along with the corresponding orthogonal polynomials and the corresponding formulations may be found in [11]. The multivariate basis functions $\phi_{\boldsymbol{b}(j)}$ are then constructed through tensor products of the corresponding univariate functions.

For purposes of practicality, the infinite series of expansion of Eq. (7) must be truncated through selection of an appropriate functional subspace consisting of a finite number of terms. The usual approach followed is the selection of the multivariate polynomial basis with a total maximum degree P, that is $|\boldsymbol{b}_j| = \sum_{m=1}^{M} b_{(j,m)} \leq P \; \forall j$. In this case the dimensionality of the functional subspace is equal to:

$$p = \frac{(M+P)!}{M!P!} \tag{9}$$

where M is the number of random variables and P the maximum basis degree. In this way, Eq. (7) should be rewritten as:

$$\theta_i(\boldsymbol{\xi}) = \sum_{j=1}^{p} \theta_{i,j} \cdot \phi_{\boldsymbol{b}(j)}(\boldsymbol{\xi}) + e_i \tag{10}$$

with e_i designating the residual error of the truncated PC expansion, with the resulting metamodel being fully parametrized in terms of a finite number of deterministic coefficients of projection $\theta_{i,j}$. The estimation of $\theta_{i,j}$ (with $i = 1, \ldots, \dim(\theta)$ and $j = 1, \ldots, p$) is a linear regression problem that may be solved by means of ordinary least squares optimization, based on available time history data for the excitation and dynamic response of the numerical model. This data may be acquired for a set of simulations, conducted for different realizations of the input random vector, using the full scale numerical model.

Toward this end, a series of K simulations conducted for a corresponding number of input random vector realizations $\boldsymbol{\xi}_k = [\xi_{k,1}, \xi_{k,2}, \ldots, \xi_{k,M}]^\intercal$ (for

$k = 1, 2, \ldots, K)$ is considered available. The corresponding dynamic response signals of the full scale numerical model to a specific excitation signal $x^T = \{x[1], x[2], \ldots, x[T]\}$ are indicated as $\boldsymbol{y_k^T}(\boldsymbol{\xi}_k) = \{y_k[1, \boldsymbol{\xi}_k], y_k[2, \boldsymbol{\xi}_k], \ldots, y_k[T, \boldsymbol{\xi}_k]\}$. For these simulations, the input vector $\boldsymbol{\xi}_k$ is generated from the input parameter space either randomly or by using a structured sampling technique, such as the Latin Hypercube Sampling (LHS; [24]).

The complete procedure of the metamodel identification is illustrated in the flowchart of Figure 2.

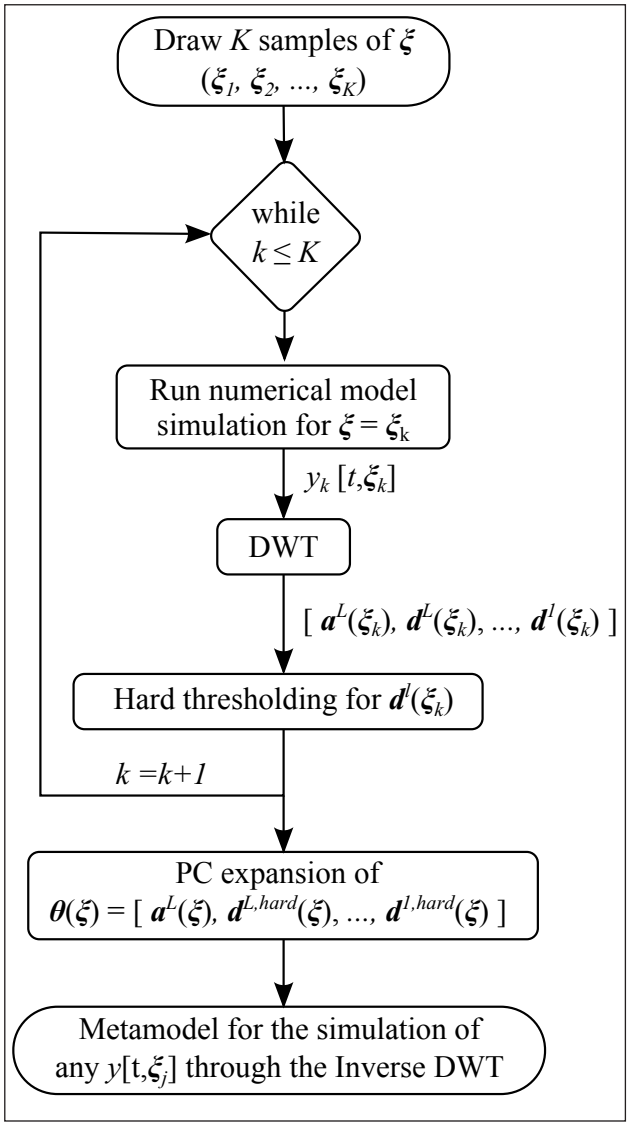

Figure 2: Flowchart of the metamodeling method.

3 Numerical Example

3.1 Simply supported beam with a moving mass

A FE model of a simply supported beam featuring a moving mass (Figure 3) and subjected to random excitation is presently considered for the assessment of the introduced method. The considered testcase simulates bridge under moving vehicle problem that is often met within a Structural Health Monitoring (SHM) context.

The beam of length L = 1.5 m is comprises an orthogonal steel cross section with isotropic material behavior and is discretized in N = 1000 elements. The geometric properties of the beam are summarized in Table 1. It is considered that the steel's Young modulus E is characterized by uncertainty and may be modelled as a random variable following a normal (Gaussian) distribution E ~ N(200, 25) (GPa). The rest of the beam's mechanical and geometric properties are considered to be characterized by negligible uncertainty.

The moving mass is also assumed as uncertain, following a normal distribution $m_{\text{total}} \sim \mathcal{N}(1, 0.04)$ (kg), while it is equally distributed over $\mu = 100$ nodes of the beam, that is $m_i = m_{\text{total}}/100$ for $i = 1, \ldots, 100$. The velocity of the mass is $v = 0{,}375$ m/s moving from left to right.

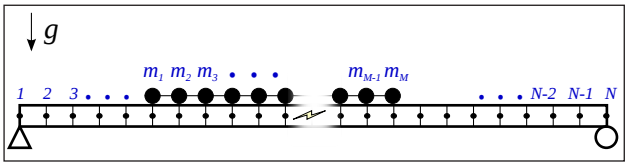

Figure 3: The model of the simply supported beam featuring a moving mass.

Table 1: Geometric and mechanical properties of the beam model.

Geometric		Mechanical	
Length	L=1.50 m	Poisson ratio	ν=0.29
Width	W=0.05 m	Density	ρ=7850 kg/m3)
Height	H=0.01 m	Young modulus	E~N(200,25) (GPa)

The identification of the beam's metamodel is based on recordings of the vertical displacement of the beam as calculated at node 200 located $L/5$ away from its left support ($y[t, \boldsymbol{\xi}] = u_{L/5_y}[t, \boldsymbol{\xi}]$).

3.2 Simulation experiments

For all simulation experiments, the beam model is simulated for 6.4 s ($t \in$ [-2, 4.4]) and is subjected to a 1600 sample long random excitation signal applied to all the nodes of the beam (y-axis direction; sampling frequency f_s = 250 Hz). A total number of K=100 full scale numerical simulations are conducted for

a corresponding number of input variable vectors $\boldsymbol{\xi}_k (k = 1, 2, \ldots, 100)$ which are drawn by using the LHS method. The values of the input variables drawn are shown in Fig. 4.

The first mass m_1 is located on node 1 (left boundary) at time instant t = 0 s and is advanced one node per each subsequent time step followed by the

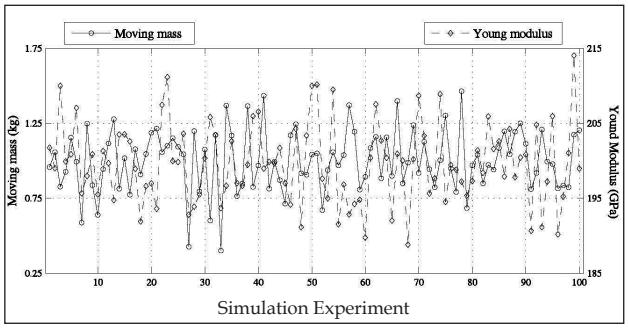

Figure 4: Material beam Young modulus and mass properties for the 100 simulations conducted.

rest of the masses. Thus, the last mass exits the beam at time instant t=4.4 s and these 1100 samples are retained for the subsequent analysis. The time-histories of the model's dynamic response at node 200, for all simulations, are shown in Figure 5 along with the histogram of the displacement of the node observed

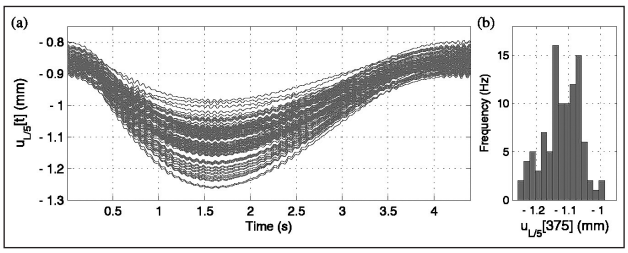

Figure 5: (a) FE model dynamic response signal $y[t, \boldsymbol{\xi}_k]$ for input parameter vectors $\boldsymbol{\xi}_1, \ldots, \boldsymbol{\xi}_{100}$ and (b) the histogram of the beam displacement at time instant t =1.5 s for all simulation experiments.

from all experiments at time instant t=1.5 s.

3.3 Metamodeling results

The level of the MRA is first selected by decomposing the available response data $y_k^T(\boldsymbol{\xi}_k)(k = 1,..., 100)$ at various MRA levels (ℓ =1,... ,7). The results of this procedure indicate that a maxi-mum level of the MRA equal to five (L=5) should be adequate for the accurate reconstruction of the dynamic response signals (Figure 6).

The MRA algorithm with L = 5 for every $y_k^T(\boldsymbol{\xi}_k)$ gives a set of (1171 × 100) wavelet coefficients. The

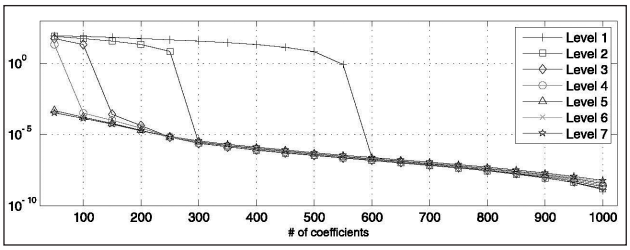

Figure 6: Mean normalized square error value for the 100 simulation experiments conducted, various MRA levels ($\ell = 1, \ldots, 7$) and different levels of compression

dimensionality of this set may be significantly reduced after applying hard thresholding with thr = 10. This value is selected through a trial and error procedure for compromising the length of the wavelet coefficients vector with the minimization of the normalized sum of squared errors (NSE) criterion:

$$\text{NSE} = \frac{\sum_{t=1}^{T} \left(y_k[t, \boldsymbol{\xi}_k] - \tilde{y}_k[t, \boldsymbol{\xi}_k]\right)^2}{\sum_{t=1}^{T} (y_k[t, \boldsymbol{\xi}_k])^2} \tag{11}$$

obtained from the reconstruction $\tilde{y}_k^T(\boldsymbol{\xi}_k)$ of $\tilde{\nu}_k^T(\boldsymbol{\xi}_k)$. The persistence of each of the 1171 wavelet coefficients after the thresholding procedure is shown in Figure 7. All the 345 non-zero coefficients are retained for the subsequent PC expansion.

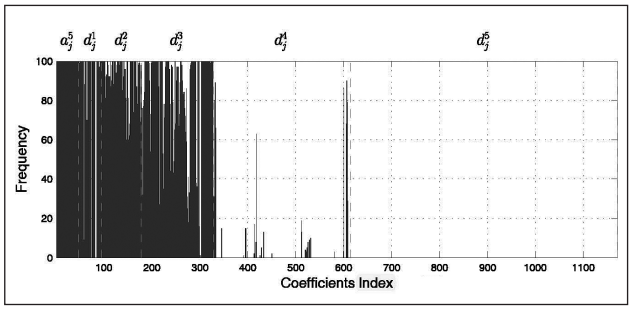

Figure 7: Persistence of the wavelet coefficients after hard thresholding.

The input random variables are transformed into standard Gaussian variables and thus the wavelet coefficients are expanded on Hermite polynomials of the standard Gaussian random variables ξ_1 and ξ_2 :

$$\xi_1 = \frac{E - 200}{5}, \quad \xi_2 = \frac{m_{\text{total}} - 1}{0.2} \tag{12}$$

The PC maximum total degree is selected equal to four p = 4 resulting to 15 bases functions (see Eq. (9)). The final set of (345 ×15) PC projection coefficients may be used for the simulation of the dynamic response of the FE model $y^T(\boldsymbol{\xi})$ for any realization of $\boldsymbol{\xi}$ drawn from the predetermined joint pdf. The NSE errors of the reconstructed 100 signals that were used for the identification of the metamodel are shown in Figure

8 and are in all cases less that 3.2×10^{-6}%. The original FE dynamic response signal $y_1^T(\boldsymbol{\xi}_1)$ is also contrasted to the metamodel-based reconstruction $\tilde{y}_1^T(\boldsymbol{\xi}_1)$ in Figure 9. Furthermore, the original detail wavelet coefficients are also cross-compared to those obtained after thresholding and expanding on the PC basis in the same figure.

The performance of the estimated metamodel is finally assessed through its application for the simulation of the dynamic response of the

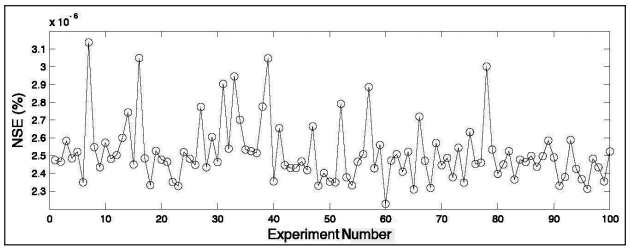

Figure 8: The Normalized Sum of Squared errors obtained by the reconstructed dynamic response signals based on the identified metamodel.

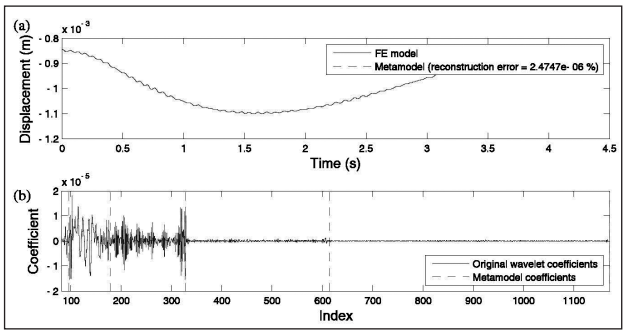

Figure 9: (a) The $y_1^T(\boldsymbol{\xi}_1)$ dynamic response of the FE model and the corresponding reconstructed signal $\tilde{y}_1^T(\boldsymbol{\xi}_1)$ based on the identified metamodel, and (b) the original detail wavelet coefficients and those obtained by the metamodeling method.

numerical model of Figure 3 for random variable values $\boldsymbol{\xi}_j^{\text{valid}}$ that are different from those of the initial 100 experiments. More specifically, the following values are used for these validation experiments: $\boldsymbol{\xi}_1^{\text{valid}} = [-4 \;\; -2]^{\mathsf{T}}$, $\boldsymbol{\xi}_2^{\text{valid}} = [-2 \; 0]^{\mathsf{T}}$ and $\boldsymbol{\xi}_3^{\text{valid}} = [0 \; 2]^{\mathsf{T}}$ with the corresponding values of the FE model input variables being summarized in Table 2.

The simulated responses of the metamodel, along with the dynamic response of the FE model for these validation experiments are illustrated in Figure 10. As it may be observed, the estimated metamodel is capable of reproducing the dynamic response of the numerical model with excellent accuracy for all these

Table 2: Values of the input variables for the validation experiments.

Experiment	1	2	3
E (GPa)	180	190	200
$m_{\{total\}}$ kg	0.6	1	1.4

cases. It should be noted that in two of these cases, extreme values have been selected for some of the uncertain parameters (for instance, the mass value for $\boldsymbol{\xi}_3^{\text{valid}}$ is much higher than the values used for the initial simulations and the identification of the metamodel). Finally, it should be added that the metamodel-based simulated response was calculated in negligible time, 10^5 times lower that the time required for the simulation experiment of the FE model. This translates into an order of magnitude of milliseconds for the metamodel simulation versus roughly 10 minutes per simulation for the FE model. These estimates are obtained as the mean value of 100 simulations on a PC with quad-core Xeon 3.5 GHz CPU and 8 GB RAM.

4. Conclusions

This work introduces a reduced order metamodel for the modeling of nonstationary systems based on the DWT and PC basis expansion. The metamodel is identified through a multi-step procedure, which includes the computationally inexpensive MRA algorithm for the decomposition and compression of the dynamic response signals of a large scale FE model, and a least squares optimization procedure for the expansion of the wavelet coefficients onto properly selected PC basis. In order to illustrate the

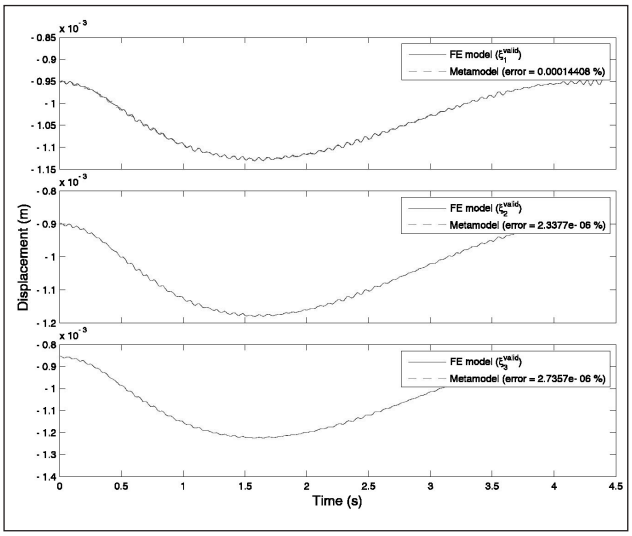

Figure 10: The dynamic response of the FE model and the corresponding metamodel-based simulation signal for the validation experiments.

workings of the method, the whole procedure is implemented for the construction of a metamodel representation of a FE model of a beam under moving load, subject to random excitation. The meta-model was estimated from simulated data obtained by the original FE model, with the mechanical properties of the structure assumed to be uncertain parameters following probability distributions with predefined characteristics. Overall, the study demonstrated the effectiveness and applicability of the proposed method for the estimation of stochastic, computationally inexpensive metamodels that are capable of accurate approximation of nonstationary systems, while at the same time accounting for the inherent uncertainties involved. This comes to compliment previous work of the authors on the successful use of PCE for the metamodeling of hysteretic nonlinear systems.

References

1. M. Spiridonakos, A. Poulimenos, and S. Fassois, "Output-only identification and dynamic analysis of time-varying mechanical structures under random excitation: A comparative assessment of parametric methods," Journal of Sound and Vibration, vol. 329, pp. 768–785, March 2010.
2. A. Poulimenos and S. Fassois, "Parametric time-domain methods for non-stationary ran-dom vibration modelling and analysis – a critical survey and comparison," Mechanical Systems and Signal Processing, vol. 20, no. 4, pp. 763–816, 2006.
3. L. Avendaño Valencia and S. Fassois, "Stationary and non-stationary random vibration mod-elling and analysis for an operating wind turbine," Mechanical Systems and Signal Processing, vol. 47, no. 1-2, pp. 263–285, 2014.
4. G. Schuëller, "On the treatment of uncertainties in structural mechanics and analysis," Comput-ers & Structures, vol. 85, no. 5-6, pp. 235–243, 2007.
5. K.-J. Bathe, "Finite element method," in Wiley Encyclopedia of Computer Science and Engi-neering (B. Wah, ed.), pp. 1253–1264, Wiley & Sons, Inc., 2009.
6. V. Z. Zadeh and A. Patnaik, "Finite element modeling of the dynamic response of a composite reinforced concrete bridge for structural health monitoring," International Journal of Advanced Structural Engineering, vol. 6, no. 2, pp. 1–14, 2014.
7. R. Ghanem and P. Spanos, Stochastic Finite Elements: A Spectral Approach, Revised Edition. Dover Publications, 2012.
8. G. Blatman and B. Sudret, Probabilistic Engineering Mechanics, vol. 25, no. 2, pp. 183–197, 2010.
9. S. T. and P. Lermusiaux, "Dynamical criteria for the evolution of the stochastic dimensionality in flows with uncertainty," Physica D: Nonlinear Phenomena, vol. 241, pp. 60–76, 2012.
10. P. V. M. Gerritsma, J.-B. van der Steen and G. Karniadakis, "Time-dependent generalized poly-nomial chaos," Journal of Computational Physics, vol. 229, pp. 8333–8363, 2010.
11. C. Soize and R. Ghanem, "Physical systems with random uncertainties: Chaos representations with arbitrary probability measure," SIAM Journal on Scientific Computing, vol. 26, no. 2, pp. 395–410, 2004.
12. D. Xiu and G. Karniadakis, "The Wiener-Askey polynomial chaos for stochastic differential equa-tions," SIAM Journal on Scientific Computing, vol. 24, no. 2, pp. 619–644, 2002.
13. G. Blatman and B. Sudret, "Adaptive sparse polynomial chaos expansion based on least angle regression," Journal of Computational Physics, vol. 230, no. 6, pp. 2345–2367, 2011.
14. L. Cohen, Time Frequency Analysis. Prentice Hall PTR, 1995.
15. Z. Shi and S. Law, "Identification of linear time-varying dynamical systems using hilbert transform and empirical mode decomposition method," Journal of Applied Mechanics, vol. 74, pp. 223–230, March 2007.
16. R. Ghanem and F. Romeo, "A wavelet-based approach for the identification of linear time-varying dynamical systems," Journal of Sound and Vibration, vol. 234, pp. 555–576, 2000.
17. M. Spiridonakos and S. Fassois, "Non-stationary random vibration modelling and analysis via functional series time-dependent ARMA (FS-TARMA) models – a critical survey," Mechanical Systems and Signal Processing, vol. 47, pp. 175–224, Aug 2014.
18. Z. Shi, S. Law, and H. Li, "Subspace-based identification of linear time-varying system," AIAA Journal, vol. 45, pp. 2042–2050, August 2007.
19. S. Mallat, A Wavelet Tour of Signal Processing, The Sparse Way. Academic Press, 3rd ed., 2008.
20. M. Spiridonakos and E. Chatzi, "Metamodeling of dynamic nonlinear structural systems through polynomial chaos NARX models", Computers & Structures, vol. 157, pp. 99-113, 2015.
21. M. Spiridonakos and E. Chatzi, "Metamodeling of structural systems through polynomial chaos ARX models," in International Conference on Uncertainty in Structural Dynamics (USD2012), Leuven, Belgium, September 17-19, 2012, 2012.
22. M. Spiridonakos and E. Chatzi, "Metamodeling of structural systems with parametric uncer-tainty subject to stochastic excitation," in 11th International Conference on Structural Safety & Reliability (ICOSSAR 2013), Columbia University, New York, June 16-20 2013.
23. J. Murguia and H. Rosu, "Discrete wavelet analyses for time series," in Discrete Wavelet Trans-forms -Theory and Applications (J. Olkkonen, ed.), Intech, 2011.
24. J. C. Helton and F. J. Davis, "Latin hypercube sampling and the propagation of uncertainty in analyses of complex systems," Reliability Engineering and System Safety, vol. 81, no. 1, pp. 23– 69, 2003.

Life Cycle Reliability and Safety Engineering
Vol.4 Issue 2 (2015) 28-39

Sensor Placement using Fisher Information Matrix for Robust Finite Element Model Updating

Masoud Sanayei[1*], Christopher J. DiCarlo[1], Peeyush Rohela[1], Eric L. Miller[2], Misha E. Kilmer[3]
[1]*Department of Civil & Environmental Engineering, Tufts University, Medford MA, USA, 02155;*
[2]*Professor, Department of Electrical & Computer Engineering, Tufts University, Medford MA, USA, 02155;*
[3]*Professor, Department of Mathematics, Tufts University, Medford MA, USA, 02155;*
Email: masoud.sanayei@tufts.edu;

Abstract

Three methods are presented to reduce the influence of measurement errors in parameter estimation in finite element model updating for structural health monitoring and damage assessment. First, a method using the Fisher information matrix is developed to choose an efficient set of measurement locations. This ensures efficient setup of a non-destructive test for finite element model updating for a given set of unknown parameters. Second, a normalization scheme is presented that, generally speaking, weighs data in a manner that varies inversely to the level of measurement error. This normalization results in a final estimate that is very close to the maximum likelihood estimator of the unknown parameters. Finally, the Fisher information matrix and its inverse, the Cramer-Rao lower bound covariance matrix, are used to quantify the uncertainty in the final estimates. Numerical examples showed the proposed methods are effective in improving observability and accuracy of parameter estimates in finite element model updating. Minimizing the effect of measurement errors and their propagation in parameter estimates can greatly improve the finite element model updating for structural health monitoring.

Keywords: Structural Parameter Estimation, Finite Element Model Updating, Measurement Errors, Maximum Likelihood Estimator, Fisher Information Matrix, Cramer-Rao Lower Bound, Sensor Placement

1. Introduction

This research aims to make enhancements to the parameter estimation process for finite element model updating in presence of measurement errors in the following areas: (1) the design of non-destructive tests to ensure useful data are collected for estimation of a set of unknown parameters, (2) statistical normalization to make the final estimates less sensitive to measurement error, and (3) quantification of uncertainty in parameter estimates to aid in decision making. It is shown through numerical simulations that these effects have significant effect on the robustness, variance, and usefulness of the parameter estimation process in structural health monitoring. These methods are studied for specific error functions or residuals that were developed by the authors and previous graduate students as referred further in the text.

Recently, there has been interest in the use of Bayesian methods for structural health monitoring. Its application in development of sensor placement algorithms for structural identification for multi-type sensory systems is researched by Yuen and Kuok [1]. Using a sequential sensor placement algorithm of Bayesian nature, they assess the overall performance of various types of sensors at different locations of a structure and demonstrate the effectiveness of their proposed method with examples of shear building and lattice towers with up to four different sensor types.

The use of multiple types of data or "data fusion" in parameter estimation is an area of active research. Perera et al. [2] present a damage identification methodology that allows combining static and dynamic measurements in a single stage model updating procedure formulated as a multi-objective framework. Bell et al. [3] simultaneously use dynamic mode shapes and frequencies as well as static data including displacements, tilts, and strains to update a finite element model of a scale bridge deck located at the University of Cincinnati Infrastructure Institute [4]. Because the different types of measurements vary over several orders of magnitude (strains are on the order of 10^{-6}, tilts on the order of 10^{-3} radians, and displacements are on the order of 10^{-1} to 10^{+1} depending

on units) there is a need for normalization such that each measurement is appropriately weighed in the estimation process. They choose to normalize the error function with respect to its initial values. This solution produces reasonable parameter estimates, but the final estimates vary depending on the initial assumptions of the unknown parameters. This paper presents a different form of normalization. It is based on the level of uncertainty as quantified in a covariance matrix of the measurements and does not exhibit a dependence on initial values of unknown parameters.

The current, deterministic methods of finite element model updating work very well when there is little or no error in the model and measurement data, but they start to exhibit large errors in parameter estimates when even modest levels of error are present. There are three types of errors that cause inaccuracies in the estimates. These errors can be classified as modeling errors, measurement errors, and estimation errors. Sanayei et al. [5] have studied the impact of modeling error on parameter estimation in finite element model updating and found that the derivative of the sensitivity matrix with respect to modeling errors reveal the potential effect of modeling errors on the parameter estimation process. Also, the sparse set of measurements may cause the modeling errors to propagate throughout the error function because of the matrix inversions required to condense out the DOFs with unmeasured responses. The effects of modeling errors are beyond the scope of this work. Furthermore, there are special setups, such as the laboratory settings, where modeling errors are better controlled. Measurement errors occur because the measurement systems (sensors and data acquisition system) are not capable of producing perfect measurements. In a laboratory setting, measurement errors can be significantly lower depending on the type of measurements and calibrations. However, measurement errors can be significant in the field based on instrumentation types, installation methods, field calibrations, and presence of larger ambient noise. Measurement errors also include errors that arise while processing raw sensor data into usable measurements. One such example is extraction of the mode shapes from time history acceleration data. Measurement errors are addressed in this paper. Minimizing the effect of measurement errors and their propagation and magnification in the parameter estimation process can greatly improve the accuracy of updated finite element models.

2. Error Function and Scalar Objective Function

The static flexibility error function developed by Sanayei et. al [6] compares predicted and measured displacements. Based on the inverse of the force-displacement relationship, it is defined as,

$$\mathbf{e}(\mathbf{p}) = \mathbf{u}_{predicted} - \mathbf{u}_{measured} = \mathbf{B}\left[\mathbf{K}(\mathbf{p})\right]^{-1}\mathbf{f}^m - \mathbf{u}^m \qquad (1)$$

In the above formulation, $\mathbf{K}(\mathbf{p})$ is the stiffness matrix which is dependent on the model parameters in the NUP x 1 vector $\mathbf{p}$, where NUP is the number of unknown parameters. Examples of stiffness parameters include axial rigidity EA, bending rigidity EI, torsional rigidity GJ, and spring stiffness as used in finite element analysis. The matrix $\mathbf{B}$ is a Boolean matrix that extracts the measured degrees of freedom of the inverted stiffness matrix. The vectors $\mathbf{f}^m$ of size NDOF x 1 and $\mathbf{u}^m$ of size NMDOF x 1 are measured forces and displacements respectively obtained from each non-destructive load case, where NDOF is the number of degrees of freedom of the system containing zero and nonzero forces and NMDOF is the number of measured degrees of freedom.

Ordinarily, several load cases are used in a nondestructive test. Also, at times a combination of global displacement and rotation measurements in Eq. (1) are used in conjunction with local strain measurements [7]. Multiple nondestructive test load cases and different error functions of various sizes are combined by vertically concatenating (denoted by ;) the individual error function vectors as follows:

$$\{\mathbf{e}\} = \{\mathbf{e}_1; \mathbf{e}_2; \ldots; \mathbf{e}_{n-1}; \mathbf{e}_n\}. \qquad (2)$$

The error vector, Eq. (1), is of size NM x 1 where NM is the total number of measurements and is equal to the number of load cases times the number of sensors per load case. For parameter estimation, the error vector, Eq. (2), is converted into a scalar objective function that can be minimized to arrive at the final estimates:

$$J(\mathbf{p}) = \mathbf{e}^T\mathbf{e}\,. \qquad (3)$$

Minimization of the scalar error function, Eq. (3), results in multi-response parameter estimation [8]. Similar to the static flexibility error function, error functions can be also be formulated in terms of static strains or modal displacement parameters as summarized in [9]. The methods developed in this research are applicable to those error functions as well.

3. Maximum Likelihood Estimation

This research is based on the fact that all measurements in structural health monitoring are representative of the true behavior of the structure with the addition of some random measurement error. Assuming that the distribution characteristics of the measurement error are known, the "likelihood" of observing any set of measurements can be calculated for a given set of model parameters. The likelihood of a set of model parameters given a set of measurements is the probability of observing the measurements in a model with those parameters. Updating the unknown parameters of the model changes the model behavior and therefore changes the likelihood of observing the set of measurements. Finding the model parameters that maximize the likelihood of the measurements results in the maximum likelihood estimate for those parameters. The maximum likelihood estimate is the most plausible configuration for the unknown parameters given the collected data.

In order to calculate a maximum likelihood estimate it is necessary to first define some preliminary assumptions and definitions. It is assumed that the data obtained from a non-destructive test is contaminated with unbiased normal error. These measurements can be described as follows,

$$\mathbf{f}^m \sim N\left(\boldsymbol{\mu}_f, \boldsymbol{\Sigma}_f\right), \tag{4}$$

$$\mathbf{u}^m \sim N\left(\boldsymbol{\mu}_u, \boldsymbol{\Sigma}_u\right), \tag{5}$$

where $\mathbf{f}^m$ and $\mathbf{u}^m$ are vectors of measured data obtained from the non-destructive test representing the force applied and the displacements measured, respectively. Since the measurements are assumed unbiased, the mean values μ_f (NDOF x 1) and μ_u (NMDOF x 1) are vectors of the measured applied forces and measured responses of the structure.

The following formulation requires additional data in comparison to non-statistical methods. In order to calculate likelihoods properly, the standard deviation of the measured data is used. These data are typically available to experimentalist through instrument specifications and calibration data. Often sensor manufacturers give confidence bounds on the measurements from a particular sensor. With some assumptions such as normality and unbiasedness, the standard deviation of a measurement can be back calculated. Further excluding the T distribution to reduce complexity, if a 95% confidence interval is given, the following equation for the standard deviation, sigma, can be used.

$$\sigma = \frac{(UB - LB)}{(2*1.96)} \tag{6}$$

In this case UB and LB are the upper bounds and lower bounds of the confidence interval respectively. The error in the measurements of the force and response are assumed to be independent, so the covariance matrices Σ_f (NDOF x NDOF) and Σ_u(NMDOF x NMDOF) are only populated along the diagonals. The diagonals of $\Sigma_f$and Σ_u contain the squares of the standard deviations (or variances) of the forces and measurements respectively.

When Eq. (4) and Eq. (5) are substituted into Eq. (1), the error function becomes a linear combination of uncorrelated normal random variables. Thus, the error function, **e**, is a normal random variable itself,

$$\mathbf{e} \sim N\left(\boldsymbol{\mu}_e, \boldsymbol{\Sigma}_e\right), \tag{7}$$

With

$$\boldsymbol{\mu}_e = \mathbf{B}\mathbf{K}^{-1}\boldsymbol{\mu}_f - \boldsymbol{\mu}_u = \mathbf{0} \text{ and} \tag{8}$$

$$\boldsymbol{\Sigma}_e = \left(\mathbf{B}\mathbf{K}^{-1}\right)\boldsymbol{\Sigma}_f\left(\mathbf{B}\mathbf{K}^{-1}\right)^T + \boldsymbol{\Sigma}_u . \tag{9}$$

The size of $\mathbf{e}$ is (NMDOF x 1). Since μ_f and μ_u consist of true forces and displacements, the force-displacement model implies that the right side of Eq.(8) is equal to zero and therefore the error function is unbiased. The formulation for the covariance matrix of the error function Σ_e in Eq. (9) is a result of the fact that $\mathbf{e}(\mathbf{p})$ in Eq. (1) is a linear combination of normal random variables. Note that even though all errors in force and displacement measurements are assumed independent, the random terms of the error function are not independent. This is evident from the presence of the terms **B** and $\mathbf{K}^{-1}$ in Eq. (9) and results in Σ_e for a given load case to be fully populated (i.e., Σ_e is a dense matrix).

One way to view the relationship between variance matrices in Eq. (9) is as follows. $\Sigma_e = \mathbf{P} + \Sigma_u$, where $\mathbf{P}$ is the symmetric positive definite matrix $\left(\mathbf{B}\mathbf{K}^{-1}\right)\boldsymbol{\Sigma}_f\left(\mathbf{B}\mathbf{K}^{-1}\right)^T$. Therefore, we can think of Σ_e as the symmetric positive definite matrix Σ_u, perturbed by a symmetric positive definite perturbation matrix $\mathbf{P}$. If a symmetric positive definite matrix is perturbed by another symmetric positive definite matrix, the

eigenvalues can only increase [10]. Therefore, the eigenvalues of Σ_e, which are positive and real, must be bounded below by the positive and real eigenvalues of Σ_u. Furthermore, since it is well-known that the determinant of a matrix is the product of its eigenvalues, it follows that the determinant of Σ_e is bounded below by the determinant of Σ_u. We will make use of these observations in deriving a simplified approximation to our cost function shortly.

The error function **e** is a normally distributed random vector that is dependent on the set of structural parameters **p** and the measured data $\mathbf{f}^m$ and $\mathbf{u}^m$. If the measurements, $\mathbf{f}^m$ and $\mathbf{u}^m$ are held constant, and the parameters **p** are allowed to vary, the likelihood function of the model parameters is obtained. This function is denoted here with *L*:

$$L(\mathbf{p}) = f_e(\mathbf{e}\,|\,\mathbf{p}) = \frac{1}{(2\pi)^{NM/2}\left|\mathbf{\Sigma}_e\right|^{1/2}} \exp\left(-\tfrac{1}{2}\left(\mathbf{e}^T\mathbf{\Sigma}_e^{-1}\mathbf{e}\right)\right). \quad (10)$$

This expression gives the likelihood of observing the structural behavior of $\mathbf{f}^m$ and $\mathbf{u}^m$, given a set of model parameters **p**, where **e** is an implicit function of **p** through the dependency of K on **e**. In order to find the maximum likelihood estimator for **p**, Eq. (10) must be maximized over the estimated parameters. Since the natural log function is a strictly increasing function in the positive domain, maximizing Eq. (10) is equivalent to maximizing the natural log of it. This is called the log-likelihood function and is denoted here with $l(\mathbf{p})$.

$$\ln(f_e(\mathbf{e}\,|\,\mathbf{p})) = l(\mathbf{p}) = -\frac{NM}{2}\ln(2\pi) - \tfrac{1}{2}\ln\left(\left|\mathbf{\Sigma}_e\right|\right) - \tfrac{1}{2}\left(\mathbf{e}^T\mathbf{\Sigma}_e^{-1}\mathbf{e}\right) \quad (11)$$

NM and π are constant so when maximizing Eq.(11) the first term can be ignored because it is not dependent on **p**. From Eq. (9), Σ_e is dependent on the estimated parameters, because of the presence of $\mathbf{K}(\mathbf{p})$ in its formulation, but this makes the problem of optimizing Eq. (11) significantly more difficult. Therefore, simplifying assumptions might be used to replace Eq. (11) by a surrogate objective function.

First, from the previous discussion, Σ_u is positive definite, $\left|\mathbf{\Sigma}_e\right|$ cannot go to zero, which means that the expression $-\ln\left(\left|\mathbf{\Sigma}_e\right|\right)$ will not blow up to infinity, and thus log-likelihood function is bounded above by $-\ln\left(\left|\mathbf{\Sigma}_u\right|\right)$ plus the last term in Eq. (11). Since Σ_u does not depend on Eq. (11), then, to get our surrogate objective function, we will ignore $-\tfrac{1}{2}\ln\left(\left|\mathbf{\Sigma}_e\right|\right)$.

Next, we need to think about maximizing $-\tfrac{1}{2}\left(\mathbf{e}^T\mathbf{\Sigma}_e^{-1}\mathbf{e}\right)$, or alternatively, minimizing $\tfrac{1}{2}\left(\mathbf{e}^T\mathbf{\Sigma}_e^{-1}\mathbf{e}\right)$. First, we note that since Σ_e is symmetric and positive definite, Σ_e^{-1} is too, and so $\Sigma_e^{-1}=\mathbf{G}^T\mathbf{G}$ for some matrix **G**. This means that objective function is:

$$\tfrac{1}{2}\left\|\mathbf{Ge}\right\|_2^2 \le \tfrac{1}{2}\left\|\mathbf{G}\right\|_2^2\left\|\mathbf{e}\right\|_2^2 = \tfrac{1}{2}\lambda_{\max}\left(\mathbf{G}^T\mathbf{G}\right)\left\|\mathbf{e}\right\|_2^2 =$$
$$\tfrac{1}{2}\left(1/\lambda_{min}\left(\mathbf{\Sigma}_e\right)\right)\left\|\mathbf{e}\right\|_2^2 \le \tfrac{1}{2}\left(1/\lambda_{min}\left(\mathbf{\Sigma}_u\right)\right)\left\|\mathbf{e}\right\|_2^2.$$

Where the last inequality follows from the discussion relating the eigenvalues of Σ_e to Σ_u.

Since $\tfrac{1}{2}\left\|\mathbf{e}\right\|_2^2 = \tfrac{1}{2}\left(\mathbf{e}^T\mathbf{e}\right)$, if we can keep the latter expression small, we keep the objective function small as well. But the upper bound does not depend on Σ_e, which suggests that, as least locally, we may be able to think of Σ_e as fixed, and minimize $\mathbf{e}^T\Sigma_e^{-1}\mathbf{e}$. In our algorithm, we update Σ_e each outer iteration after a new value of **e** becomes available. This is equivalent to solving a sequence of local minimization problems where Σ_e is held fixed:

$$J(\mathbf{p}) = \mathbf{e}^T\mathbf{\Sigma}_e^{-1}\mathbf{e}\,. \quad (12)$$

This is the scalar objective function J(p). After simplification of Eq. (11), we arrived at the scalar objective function, J(p) which is both weighted and normalized with respect to the inverse of variance in each measurement [11].

4. Frame Example

The frame example shown in Figure 1 is a simple two-story steel portal frame that could be part of the lateral stability system of a building. The height of each story is 250 cm and the width of the frame is 500 cm. The column supports are fixed at the ground and

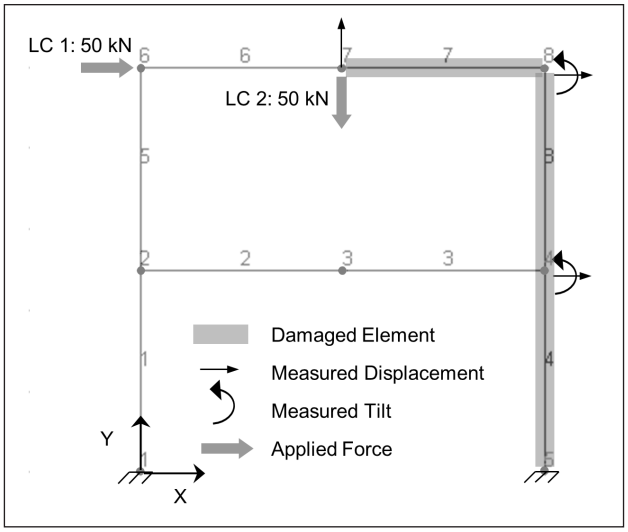

Figure 1. Frame Example

all joints are fully restrained against relative rotation. All members have geometric properties that are based on the standard W14x26 steel shape. The moment of inertia of each element is 10,198 cm^4, and the cross-sectional area of each element is 49.6 cm^2.

In this example, elements 4, 7 and 8 are damaged causing a reduction in moment of inertia. The moment of inertia of the damaged elements is 9,000 cm^4. Using PARIS© (PARameter Identification System) [9], a non-destructive test will be simulated to estimate the bending rigidities, EI, of the three damaged elements as the unknown parameters. The non-destructive test involves two load cases. In the first load case, a force of 50 kN is applied to node 6 in the horizontal direction. In the second load case, a force of 50 kN is applied to node 7 in the vertical direction. There are five displacements measured in each load case. Vertical displacement of node 7 is measured. The horizontal displacement and rotation is measured at nodes 7 and 8. There are two load cases each with five measurements, accounting for a total of 10 measurements. If coupling of axially connected degrees of freedom is assumed, then there are 9 independent measurements when the redundancies due to the Maxwell-Betti reciprocity theorem are not counted.

This non-destructive test was conducted with 1,000 Monte Carlo (MC) simulations. In each simulation, proportional normally distributed error was added to the measured forces and displacements. In each MC observation, the stiffness of the damaged elements was estimated using the error contaminated measurements. This was repeated at several different levels of error. Figure 2 shows a comparison of the covariance for maximum likelihood estimates for a 5% measurement error case with and without the proposed statistical treatment. For every unknown parameter, the maximum likelihood estimate exhibits a significantly lower coefficient of variance than the estimate without normalization.

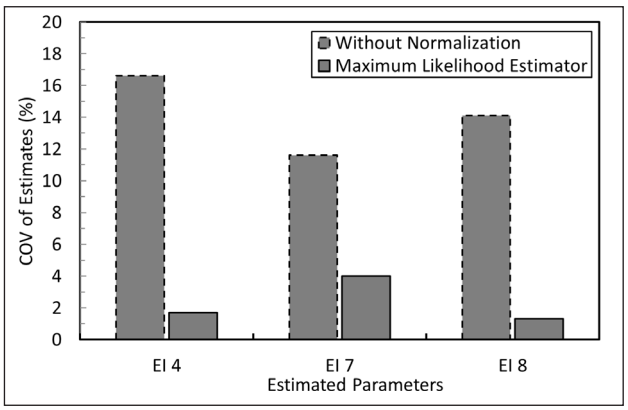

Figure 2. Comparison of COV for Maximum Likelihood Estimate and Un-normalized Estimate

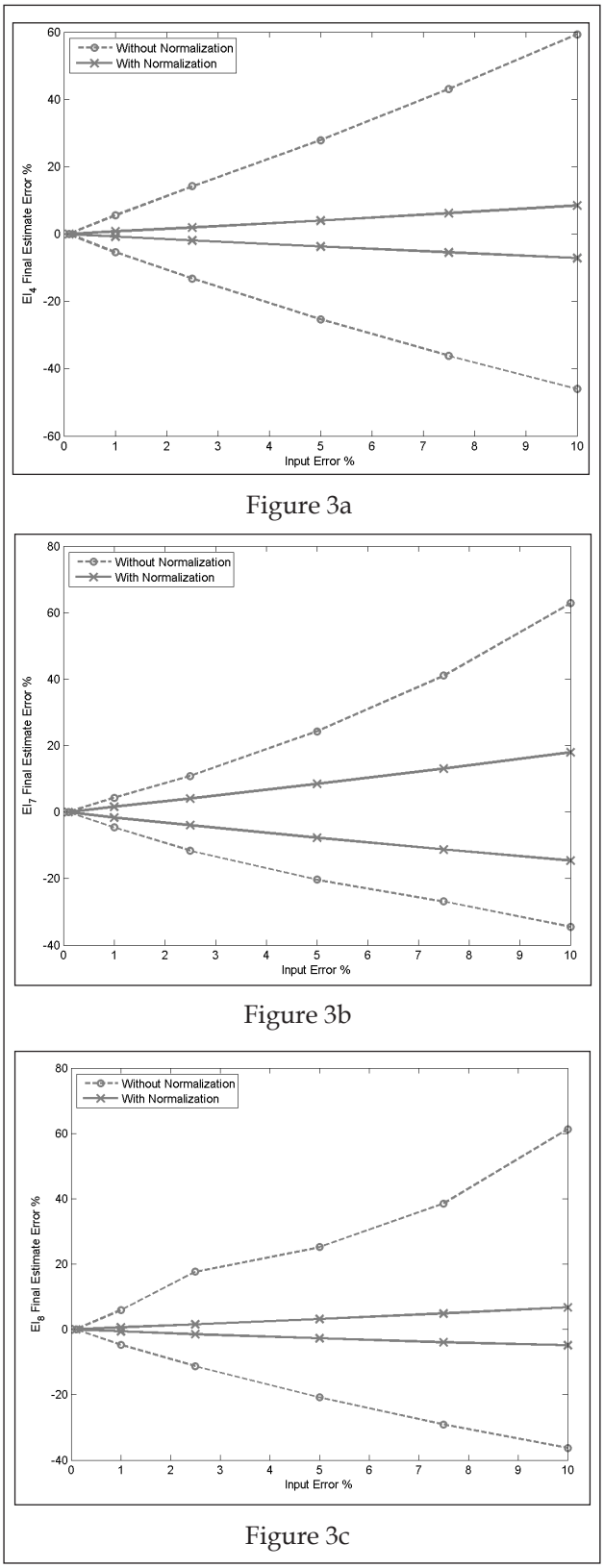

Figure 3a

Figure 3b

Figure 3c

Figure 3. Frame Example 95% Bounds of Final Estimate Error

Figure 3 shows the bounds of the middle 95% of the final estimates for elements 4, 7, and 8. This is a numerical version of the 95% confidence interval for the estimate. The dashed lines represent the bounds for the un-normalized error function and the solid lines represent the bounds for the maximum likelihood estimator. For all three elements the maximum likelihood estimator consistently produces estimates with significantly lower covariance for 1% to 10% measurement errors.

In this example there are two types of measurements, displacements and tilts. Displacements measured in centimeters are typically numerically larger than rotations measured in radians. Without normalization the error function can have mixed units where the larger magnitude measurements such as displacements have significantly larger impact on the estimation process than smaller magnitude measurements. The objective function for the pseudo-maximum likelihood estimator is normalized and is without units, and the measurements that are containing more information have more of an influence on the estimation. Using the pseudo-maximum likelihood estimator thus results in better parameter estimates.

5. Uncertainty of Estimates using Fisher Information Matrix

The estimates produced in this work are based on random variables and are therefore random themselves. Producing an estimate only solves part of the problem. In order for an engineer to use the results to make structural maintenance decisions, it is preferred to have some measure of confidence in the parameter estimates.

As it was presented above, Monte Carlo analyses can be used to give the user an idea of the variability of the estimate. In the examples presented here, it can produce estimates with lower covariance in a reasonable amount of time. However, with full-scale structures containing hundreds or thousands of degrees of freedom, the individual estimations are considerably slower. The matrix inverse operation at the heart of all the error functions is $O(n^3)$. Thus, using Cramer-Rao lower bound (CRLB) is far more computationally efficient than Monte Carlo simulations since it is based on only a single iteration compared to a large number of iterations for parameter estimations in MCs. This section develops an estimate of variability that is based on the Cramer-Rao lower bound variance. The Cramer-Rao lower bound is computed using the inverse of the Fisher Information Matrix. Ober [11] investigated the application of Fisher Information Matrix to non-stationary deterministic linear systems. It is not Monte Carlo based and is an efficient use of computer time because it only requires the result of single estimation.

This research uses the inverse of the Fisher information matrix as an estimate of the covariance matrix. It is important to note that this estimate is a lower bound of the true variance of the parameters. If $\Sigma_{\mathbf{p}}$ is the covariance matrix of the estimates and $\Im$ is the Fisher information matrix, then $\mathbf{\Sigma_p} - \Im^{-1}$ is positive semi-definite according to the Cramer-Rao inequality for the multivariate case of unbiased estimators [12].

The Fisher information matrix for an unbiased estimator is defined as follows:

$$\Im_{ij} = -\left\langle \frac{\partial^2 l(\mathbf{p})}{\partial \mathbf{p}_i \partial \mathbf{p}_j} \right\rangle \tag{13}$$

Brackets $\langle\ \rangle$ indicate expected value. In the case of this parameter estimation method, the size of the Fisher information matrix is (NUP x NUP). From Eq. (12) and the assumption that Σ_e is independent of p, the first derivative of the log-likelihood function is the following:

$$\frac{dl}{d\mathbf{p}_i} = -\mathbf{e}^T \mathbf{\Sigma}_e^{-1} \frac{\partial \mathbf{e}}{\partial \mathbf{p}_i} \tag{14}$$

where l is the log-likelihood function, $\mathbf{e}$ is the error function, and Σ_e is the covariance matrix of the error function. Taking the second derivative results in the equation

$$\frac{\partial^2 l}{\partial \mathbf{p}_i \partial \mathbf{p}_j} = -\left(\frac{\partial \mathbf{e}}{\partial \mathbf{p}_j} \right)^T \mathbf{\Sigma}_e^{-1} \frac{\partial \mathbf{e}}{\partial \mathbf{p}_i} + \mathbf{e} \mathbf{\Sigma}_e^{-1} \frac{\partial}{\partial \mathbf{p}_j} \left(\frac{\partial \mathbf{e}}{\partial \mathbf{p}_i} \right) \tag{15}$$

Using the fact that $\mathbf{e}$ has zero mean, from Eq. (8), it is clear that when taking the expectation of Eq. (15) the second term will vanish. Using the notation for the sensitivity matrix, $\mathbf{S} = \frac{\partial \mathbf{e}}{\partial \mathbf{p}^T}$, the Fisher information matrix can be written as follows:

$$\Im = \mathbf{S}^T \mathbf{\Sigma}_e^{-1} \mathbf{S} . \tag{16}$$

The inverse of the Fisher information matrix is used as the estimator for the covariance matrix of the unknown parameters:

$$\hat{\mathbf{\Sigma}} = \left(\mathbf{S}^T \mathbf{\Sigma}_e^{-1} \mathbf{S} \right)^{-1} . \tag{17}$$

6. Verification Example with Monte Carlo Experiment

The parameter covariance estimate is demonstrated using the same frame example presented earlier. The formulas are programmed into PARIS© allowing the user to get a reasonable idea of parameter uncertainty without having to perform numerous Monte Carlo iterations. Previously, a Monte Carlo approach was used to calculate the parameter standard deviations. In this section, the Monte Carlo results will be compared to the estimates using the formula derived in Eq. (22).

The CRLB covariance matrix was calculated using Eq. (17). The CRLB is an estimator for the covariance matrix of the parameter estimates. The diagonals of the CRLB represent bounds on the parameter variances. The estimate of the standard deviation is the square root of these values. In [13] the Cramer-Rao lower bound is compared to the results from the Monte Carlo simulations from the previous section for the frame example. This table shows that the Cramer-Rao lower bound gives reasonably accurate estimates of the parameter variance, but is far less time consuming to calculate than the Monte Carlo estimate.

Table 1. Comparison of Standard Deviations Estimates using CRLB and MC for Frame Example

Parameter	CRLB Var. (cm^8)	CRLB St. Dev.(cm^4)	MC St. Dev. (cm^4)	St. Dev. % Error
I_4	22,231.00	149.10	149.40	-0.20
I_7	129,130.00	359.30	358.50	0.22
I_8	13,327.00	115.40	121.10	-4.71

This approximate parameter standard deviation estimate is a powerful tool to aid in decision making. With previous methods, only a point estimate could be produced. Without any information about the confidence bounds on the estimate, it is difficult to use. Using this additional information, an interval and a level of confidence for that interval can be created using standard statistics. Using this additional information decisions about structural maintenance based on parameter estimates would be better informed resulting in a more efficient use of resources.

7. Sensor Placement

Successful finite element model updating is dependent on a well-designed non-destructive test that can easily observe the unknown parameters. Even when the error in the measurements is well controlled, a poor choice of excitation and measurement locations will doom the process from the outset. This section develops an algorithm that can be used to choose a set excitation and measurements locations that is tolerant of measurement errors and results in a final parameter estimates with lower covariance.

Choosing excitation and measurement locations on a structure is a difficult problem to solve because of its combinatorial nature. In order to solve this problem a different approach is necessary. The method presented in this section ranks the measurement and excitation locations based on their observability of all the unknown parameters, so the least productive ones can be removed. Using this approach, the number of iterations required is linear with respect to model size. And while it is not guaranteed to result in the best possible non-destructive test strategy, it usually results in a non-destructive testing strategy that is "good enough" to observe changes in all the targeted elements for parameter estimation.

The Fisher information matrix derived in the previous section can be useful in the design of non-destructive tests. Two of the four sensor location methodologies employed by Castro-Triguero et al. [13] for modal analysis of a truss bridge are based on the Fisher Information Matrix for optimal sensor placement on a dynamic system. The resulting sensor configuration will maximize the information from the system such that the data acquired from those locations would yield best identification of the unknown parameters. The Fisher information matrix can be calculated before any data are collected and before estimations are performed. The Fisher information matrix and the parameter covariance matrix are inversely related. If a set of measurements can be found that maximizes the determinant of the Fisher information matrix, this will in turn result in an estimated parameter covariance matrix with minimum determinant. Low determinant of the parameter covariance matrix is indicative of low individual parameter variances. An experimental design that results in maximum determinant of the Fisher information matrix is called D-optimal. Assuming normality of estimates, a D-optimal experimental design results in a parameter confidence ellipsoid that has minimal volume for a given level of confidence [14]. A confidence ellipsoid is simply the vector analog of a confidence interval. The confidence ellipsoid is the set of parameter vectors $\mathbf{p}$ that satisfies the following inequality,

$$(\mathbf{p}-\hat{\mathbf{p}})^T \boldsymbol{\Sigma}_p (\mathbf{p}-\hat{\mathbf{p}}) \le c\,, \tag{18}$$

where c is a scalar constant dependent on level of confidence, Σ_p is the parameter covariance matrix and $\hat{\mathbf{p}}$ is the estimated set of parameters. This is another way to say that the final estimates will have the tightest possible confidence intervals.

The main idea is to start with a superset of all possible candidates for load cases and measurements. This set should only include the locations that can be feasibly measured or excited. These load cases and measurements are then ranked based on their effect on the determinant of the Fisher information matrix. The least effective load cases and measurements are then removed until a smaller and more experimentally feasible subset is achieved. Since the poorest measurements are removed in the course of the algorithm, only the most effective measurements remain, resulting in an efficient non-destructive test design. This section builds on the work of Kammer [15] and Sanayei and Javdekar [16] using the enhancements that are presented in the following paragraphs.

A shortcoming of the research of Kammer [15] and Sanayei and Javdekar [16] is that they either assume variance is constant for each element of the error function or they ignore it entirely. Even when variance of all measurements is the same, it can be seen from Eq. (9) that Σ_e is not a uniform or diagonal matrix. The information about variations of measurements from Σ_e must be incorporated to the algorithm for a proper treatment of this problem.

Since the covariance matrix of the error function Σ_e is positive definite, it is possible to perform a Cholesky decomposition to obtain a lower triangular matrix $\mathbf{L}$ of the same size with the following property,

$$\Sigma_{e=} \mathbf{L}\mathbf{L}^T. \tag{19}$$

Taking the inverse results in the following,

$$\Sigma_{e=} \mathbf{L}^{-T}\mathbf{L}^{-1}. \tag{20}$$

Combining Eq. (16) and Eq. (20) the Fisher information matrix can be written as follows,

$$\Im = \left(\mathbf{L}^{-1}\mathbf{S}\right)^T \left(\mathbf{L}^{-1}\mathbf{S}\right). \tag{21}$$

Define the matrix $\tilde{\mathbf{S}} = \mathbf{L}^{-1}\mathbf{S}$. In this case $\tilde{\mathbf{S}}$ is of size (NM x NUP), where NM is the total number of measurements equal to the product of NMDOF, the number of measured DOF and NLC is the number of load cases applied. Using this notation, the Fisher information matrix can be rewritten using,

$$\Im = \tilde{\mathbf{S}}^T\tilde{\mathbf{S}}. \tag{22}$$

A measurement is constituted by a load case and one measured degree of freedom in that load case. Each row of $\tilde{\mathbf{S}}$ corresponds to one measurement. Consider $\Im$ and $\Im_{-i}$ which are Fisher information matrices with a full set of measurements, with the i^{th} measurement removed respectively. $\Im_{-i}$ can be written as

$$\Im_{-i} = \Im - \mathbf{r}_i^T\mathbf{r}_i\,, \tag{23}$$

where $\mathbf{r}_i$ is the i^{th} row of the $\tilde{\mathbf{S}}$ matrix and is of size (1 x NUP). The determinant of the reduced Fisher information matrix can be expressed as (see [15]).

$$\left|\Im_{-i}\right| = \left|\Im\right|\left|1-\mathbf{r}_i\Im^{-1}\mathbf{r}_i^T\right|. \tag{24}$$

Thus we have

$$\left|\Im_{-i}\right| = \left|\Im\right|\left(R_{Di}\right), \tag{25}$$

with $R_{Di} = 1-\mathbf{r}_i\Im^{-1}\mathbf{r}_i^T$. Since the Fisher information matrix is positive definite, R_{Di} must be greater than or equal to zero. If a row of $\tilde{\mathbf{S}}$ is zero, then $\mathbf{r}_i\Im^{-1}\mathbf{r}_i^T$ will also be zero. Thus it is true that $0 \le R_{Di} \le 1$. All values of $\mathbf{r}_i\Im^{-1}\mathbf{r}_i^T$ can be calculated by extracting the diagonals from the following matrix,

$$\mathbf{E} = \tilde{\mathbf{S}}\left(\tilde{\mathbf{S}}^T\tilde{\mathbf{S}}\right)^{-1}\tilde{\mathbf{S}}^T. \tag{26}$$

A singular value decomposition can be performed on $\tilde{\mathbf{S}}$ to make this calculation more stable,

$$\tilde{\mathbf{S}} = \mathbf{U}\mathbf{D}\mathbf{V}^T, \tag{27}$$

where $\mathbf{U}$ is (NM x NUP) and has the following properties $\mathbf{U}^T\mathbf{U} = \mathbf{I}$ but $\mathbf{U}\mathbf{U}^T \ne \mathbf{I}$. $\mathbf{D}$ is a diagonal matrix of size (NUP x NUP) with non-negative entries. $\mathbf{V}$ is a matrix of size (NUP x NUP) with the following properties $\mathbf{V}^T\mathbf{V} = \mathbf{I}$ and $\mathbf{V}\mathbf{V}^T = \mathbf{I}$. Using these properties, $\mathbf{E}$ can be rewritten as follows:

$$\mathbf{E} = \left(\tilde{\mathbf{S}}\mathbf{V}\mathbf{D}^{-1}\right)\left(\tilde{\mathbf{S}}\mathbf{V}\mathbf{D}^{-1}\right)^T. \tag{28}$$

From Eq. (27) and the properties of $\mathbf{V}$ and $\mathbf{D}$ mentioned above, the following is true.

$$\mathbf{U} = \tilde{\mathbf{S}}\mathbf{V}\mathbf{D}^{-1} \tag{29}$$

Thus $\mathbf{E}$ can be rewritten as,

$$\mathbf{E} = \mathbf{U}\mathbf{U}^T, \tag{30}$$

which is also known as an orthogonal projector onto the range of $\tilde{\mathbf{S}}$. Since only the diagonals of $\mathbf{E}$ are of interest, it is more efficient to calculate them by taking the square of $\mathbf{U}$ in a term by term fashion and summing across the rows. The final formulation for R_{Di} is shown below.

$$R_{Di} = 1 - \sum_{j=1}^{NPU} \mathbf{U}_{ij}^2 \tag{31}$$

8. Algorithm for Sensor Placement

Eq. (31) can be used to rank a set of measurements for sensor placement. Measurements with low corresponding $\mathbf{R}_D$ values are measurements that are valuable in the parameter estimation. However, it is not often desirable to rank individual measurements. Recall that a measurement is constituted by a load case and a measured degree of freedom in that load case. When reducing a large set of load cases and measured degrees of freedom to a more experimentally feasible set, removing a load case results in taking away measurements from all active measured degrees of freedom. Similarly, removing a measured degree of freedom removes that measurement from all active load cases. Taking this into account, it is necessary to have a way to rank the measured degrees of freedom and load cases not just individual measurements.

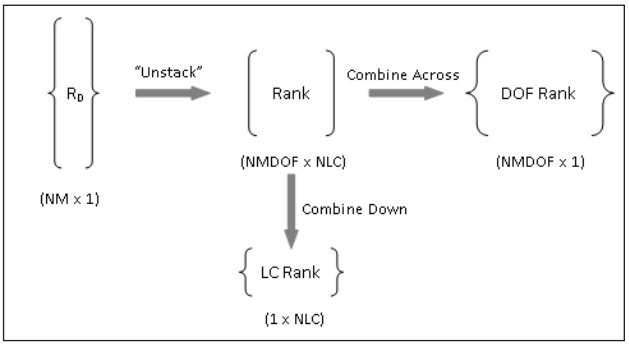

Figure 4. Sensor and Load Case Ranking Procedure Flowchart

In order to achieve this ranking, the rank vector $\mathbf{R}_D$ of length (NM) must be "unstacked" to form a matrix of size (NMDOF x NLC). This is done by extracting vectors of length (NMDOF) from the $\mathbf{R}_D$ vector and concatenating them horizontally to form a matrix. This matrix will be referred to as the Rank matrix. In the Rank matrix each row corresponds to a measured degree of freedom, and each column corresponds to a load case. Combining the matrix across rows will result in a ranking for the measured degrees of freedom and combining down columns will result in a ranking of the load cases. Figure 4 summarizes this process.

In order to mimic the form of Eq. (25) the following formulations are used to combine the Rank matrix across rows for *DOF Rank* and down columns for *LC Rank*,

$$\{DOFRank_i\} = \prod_{j=1}^{NSF} Rank_{ij} \tag{32}$$

$$\{LCRank_j\} = \prod_{i=1}^{NMDOF} Rank_{ij} \tag{33}$$

where $\mathbf{\Pi}$ indicates multiplication. Multiplication is used to keep the range of DOF and LC ranks between 0 and 1. *DOF Rank* is a ranking of each sensor, and *LC Rank* is a ranking of each load case. Since $0 \le R_{Di} \le 1$, the elements of *DOF Rank* and *LC Rank* must also be bounded by zero and one. Values close to zero indicate that taking away that measured degree of freedom or load case will result in a Fisher information matrix with very low determinant. It is desirable to keep these measurements. Values close to one indicate that the determinant of the Fisher information will remain nearly unchanged. These are the measured degrees of freedom or load cases that should be removed first, because they add little information to the non-destructive test. The load case or measured degree of freedom corresponding to the highest value in *DOF Rank* or *LC Rank* is removed from the active list and the process of calculating $\mathbf{E}_{Di}$'s and Rank is repeated. This continues until the desired number of load cases and measured degrees of freedom is obtained. The resulting experimental design is a set of measurements that will result in stable parameter estimation.

It is important to note that this is not the optimal non-destructive test design. There are many ways to measure optimality of design on an experiment for a given set of unknown parameters. This method is based on the determinant measure of optimality but it does not guarantee a D-optimal non-destructive test. For an algebraically nonlinear system of equations only the computationally intractable exhaustive approach, using all possible combinations of load cases and measured degrees of freedom, can guarantee this. The result of this method is intended to be a "good" solution to the problem. In this work, non-destructive tests that were designed using this method will be referred to as "near optimal."

9. Verification Example for Sensor Placement

The algorithm presented in the previous section will be demonstrated using the same frame example presented earlier for estimation of bending rigidities of elements 4, 7, and 8. To start, all feasible load cases and measured degrees of freedom were made active.

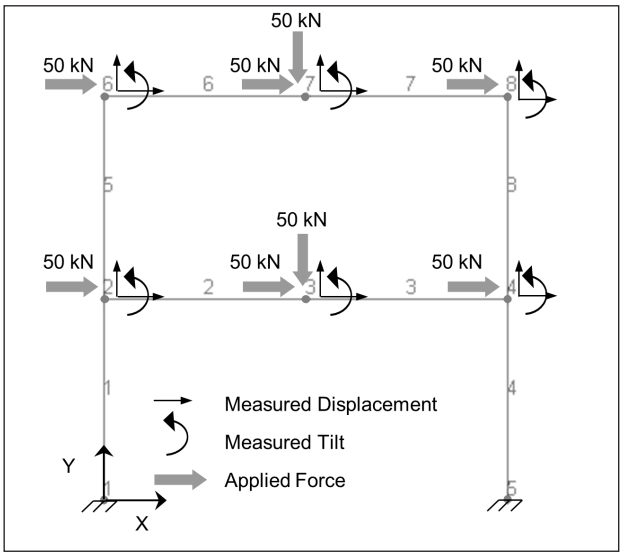

Figure 5. Available Force and Measured DOFs for Frame NDT

The superset of load cases and measured degrees of freedom was then reduced to the same size as that of the previous examples. The results from these near-optimal non-destructive tests are compared to the previous results to demonstrate the effectiveness of the non-destructive test design method.

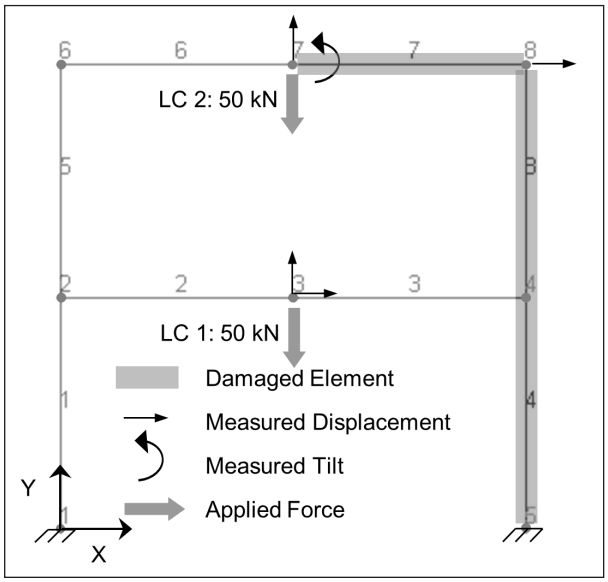

Figure 6. Near-Optimal Load Cases and Measured Degrees of Freedom for Frame Example

Load cases involving applied moments were not considered in this example because applying a pure moment to a structure in the field is very difficult. Loads were also not applied vertically over the columns because these load cases would not cause easily measurable deflections due to the high axial stiffness of the columns. All kinematic degrees of freedom were available for measurement including rotations and translations in both the vertical and horizontal directions. A summary of all available force and measured degrees of freedom in the X-Y plane is presented below in Figure 5 with eight possible load application points and 18 potential displacement and tilt measurement locations.

Using the measurement selection algorithm, the original set of 18 measured degrees of freedom was reduced to five and the original set of eight load cases was reduced to two. These measurements and load cases are shown in Figure 6 and Table 2 and Table 3.

The Rank matrix from the final iteration of the measurement selection algorithm along with the DOF Rank and LC Rank values for the selected measurements and load cases is presented in Table 4. The near-optimal non-destructive test produced significantly better results than the initial NDT design presented in Figure 1.

Table 2. Near-Optimal Loading Summary for Frame NDT

LC #	Node	Dir.	Force (kN)
1	3	Y	-50
2	7	Y	-50

Table 3. Near-Optimal MDOF Summary for Frame NDT

Meas. #	Node	Dir.
1	3	X
2	3	Y
3	7	Y
4	7	Rz
5	8	X

Table 4. Final Rank Matrix from Measurement Selection Algorithm

Meas. #	LC-1	LC-2	DOF Rank
1	0.484	0.250	0.121
2	1.000	1.000	0.999
3	0.999	0.999	0.999
4	0.763	0.212	0.162
5	0.674	0.618	0.416
LC Rank	0.249	0.033	

Recall from the previous discussion that Rank numbers near 1 indicate less useful measurements because removing them will have little effect on the determinant of the Fisher information matrix. These measurements contribute little to the estimation process. From Table 4, it is evident that measurements 2 and 3, the vertical measurements at nodes 3 and 7, could be removed with little effect on the determinant of the Fisher information matrix. This would be a

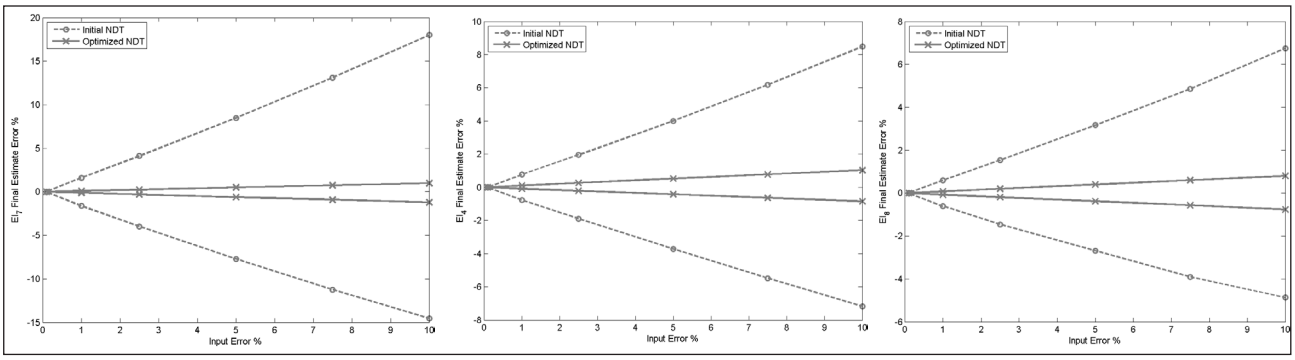

Figure 8. Near-optimal Frame Example 95% Bounds of Final Estimate Error

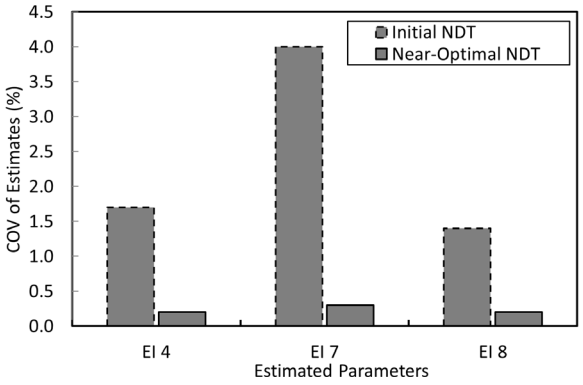

Figure 7. Comparison of COV for Initial and Near-Optimal NDT

reasonable decision if this test were carried out on a physical structure where each measurement increases the cost of the test. However, in order to make an even comparison with the previous test setup using the same number of measurements it was decided to keep these measurements so that the number of load cases and measured degrees of freedom would be the same. The near-optimal non-destructive test was simulated using 1000 Monte Carlo iterations at varying levels of error. This is compared to the results from the initial test setup with 5% measurement error in Figure 7.

Figure 8 shows the spread of the middle 95% of the final results for varying levels of error using both the initial and near-optimal testing strategies. The stability of the near-optimal NDT is shown by its narrow band in comparison to the initial test setup. Comparing the scales of Figure 3 and Figure 8, it can be seen that two levels of improvement are presented in this work. The wide bands presented in Figure 8 are the same data as the narrow bands presented in Figure 3. When an effective non-destructive test and the method of the maximum likelihood estimator are employed together the results have far less covariance.

10. Conclusions

The research presents three layers of enhancements to the parameter estimation for finite element model updating to reduce the influence of measurement errors in parameter estimation. The Fisher information matrix is developed to choose an efficient set of measurement locations for parameter estimation. The normalization scheme is developed to estimate parameters that are very close to the maximum likelihood estimator of the unknown parameters. The Cramer-Rao lower bound is used to quantify the uncertainty in the parameter estimates. The results obtained in the frame example structure point to the robustness of the approach and support the plan to move forward adapting it to more complex and realistic problems. The development of an efficient method for sensor placement in non-destructive testing can ensure useful data collection for robust parameter estimation. Any parameter estimation using these data will be tolerant to measurement errors. The effectiveness of the proposed method for design of nondestructive tests and parameter estimations with low variability is successfully shown using numerical examples.

References

1. Yuen K.-V. and Kuok S.C. (2014) Efficient Bayesian sensor placement algorithm for structural identification: a general approach for multi-type sensory systems, *Earthquake Engineering & Structural Dynamics*, DOI: 10.1002/eqe.2486.
2. Ricardo Perera, Roberto Marin, Antonio Ruiz, Static–dynamic multi-scale structural damage identification in a multi-objective framework, *Journal of Sound and Vibration*, Volume 332, Issue 6, 18 March 2013, Pages 1484-1500, ISSN 0022-460X, http://dx.doi.org/10.1016/j.jsv.2012.10.033.
3. Bell, E. S., Sanayei, M., Javdekar, C. N., Slavsky, E. (2007). "Multiresponse Parameter Estimation for Finite-Element Model Updating using Nondestructive Test Data." *Journal of Structural Engineering,* 133(8), 1067-1079.
4. Catbas, F.N. and Aktan A. E. (2002). "Condition and Damage Assessment: Issues and Some Promising Indices." *J. Structural Engineering*, ASCE, 128(8), 1026-1036.

5. Sanayei, M., Wadia-Fascetti, S., Arya, B., and Santini, E., "Significance of Modeling Error in Structural Parameter Estimation," Special issue of the International Journal of Computer-Aided Civil and Infrastructure Engineering devoted to Health Monitoring of Structures, Vol. 16, pp. 12-27, January 2001, pp. 12-27.
6. M. Sanayei, G.R. Imbaro, J.A.S. McClain, L.C. Brown, "Structural model updating using experimental static measurements" , ASCE J Struct Eng, 123 (6) (1997), pp. 792–798
7. Sanayei, M., Saletnik, M. J., (1996) "Parameter Estimation of Structures from Static Strain Measurements; I: Formulation," ASCE, Journal of Structural Engineering, Vol. 122, No. 5, May 1996, pp. 555-562.
8. Banan, M. R., Banan, M. R., Hjelmstad, K. D. (1994). "Parameter Estimation of Structures from Static Response. I. Computational Aspects." *Journal of Structural Engineering,* 120(11), 3243-3258.
9. Masoud Sanayei, Peeyush Rohela, Automated finite element model updating of full-scale structures with PARameter Identification System (PARIS), *Advances in Engineering Software*, Volume 67, January 2014, Pages 99-110, ISSN 0965-9978.
10. Stewart, G. W., and Ji-guang Sun. Matrix Perturbation Theory. Boston: Academic, 1990.
11. Ober, R. (2002) "The Fisher Information Matrix for Linear Systems." Systems and Control Letters, 47(3), 221-226.
12. Magnus, J. R., and Neudecker, H. (1988). "Maximum Likelihood Estimation." *Matrix Differential Calculus with Applications in Statistics and Econometrics,* 1st Ed., John Wiley & Sons, Ltd, New York, NY, 313.
13. Rafael Castro-Triguero, Senthil Murugan, Michael I. Friswell, and Rafael Gallego (2013) "Optimal Sensor Placement for Structures under Parametric Uncertainty" Topics in Dynamics of Bridges, Vol. 3, pp. 125-132, March 2013.
14. Melas, V., B. (2006). *Functional Approach to Optimal Experimental Design,* 1st Ed., Springer Science+Buisness Media Inc., New York, NY.
15. Kammer, D. C. (1991). "Sensor Placement for on-Orbit Modal Identification and Correlation of Large Space Structures." Journal of Guidance, Control, and Dynamics, 14(2), 251-259.
16. Sanayei, M., Javdekar C. N.,(2002) "Sensor Placement for Parameter Estimation of Structures using Fisher Information Matrix," Proceedings of 7th International Conference on Applications of Advanced Technology in Transportation (AATT 2002), Cambridge, MA, August 5-7 2002, pp. 386-393.

Life Cycle Reliability and Safety Engineering
Vol.4 Issue 2 (2015) 40-51

Non-contact and Real-time Dynamic Displacement Monitoring using Smartphone Technologies

Jae-Hong Min[1], Nikolas J. Gelo[2], and Hongki Jo[1*]
[1]*Department of Civil Engineering and Engineering Mechanics,*
[2]*Department of Computer Science, The University of Arizona, Tucson, AZ 85721, USA.*
Email: hjo@email.arizona.edu

Abstract

Many of the available approaches for Structural Health Monitoring (SHM) can benefit from the availability of dynamic displacement measurements. However, current SHM technologies rarely support dynamic displacement monitoring, primarily due to the difficulty in measuring absolute displacements. The newly developed smartphone application in this study allows measuring absolute dynamic displacements in real time using state-of-the-art smartphone technologies, such as high-performance graphics processing unit (GPU), in addition to already powerful CPU and memories, embedded high-speed/resolution camera, and open-source computer vision libraries. A carefully designed color-patterned target and user-adjustable crop filter enable accurate and fast image processing, allowing up to 120Hz frame rate for complete displacement calculation. The performances of the developed smartphone application are experimentally validated, showing comparable results with those of conventional laser displacement sensor.

Key words: structural health monitoring, smartphone technology, computer vision, dynamic displacement monitoring, real time image processing

1. Introduction

Structural displacement or deformation information is particularly important when permanent deformation occurs and is often more accurate than acceleration measurements in lower-frequency ranges. However, current SHM technologies rarely support displacement monitoring, primarily due to the difficulty in measuring absolute displacement; which mostly require fixed reference points. Though the reference-free nature of GPS-based methods conveniently measures absolute displacements, relatively low sampling rates are only available and the associate cost for survey-level dual-frequency GPSs that support sub-centimeter accuracy is still too high for routine use [1~3]. Single-frequency, low-cost GPSs, generally used for navigation purposes, have shown the feasibility for dynamic displacement monitoring [4], however, the technologies of single-frequency GPSs have not been sufficiently advanced yet for practical use in SHM applications.

Computer vision-based methods have received broad interests in measuring static and dynamic displacements of structures due to various merits of the methods. The capability of non-contact, distant measurement of absolute displacements significantly reduces the difficulties in providing stationary reference points; ensuring such reference points is a critical challenge for contact-type displacement sensors [5~8]. Moreover, these vision-based measuring systems are available at relatively low cost, combining a video camera, an optical zoom lens, lighting lamps and a precision target attached to the location of interest on the structures [9].

In most civil engineering applications, computer vision-based measuring systems have been considered particularly interesting for low-frequency vibration measurements. One of the reasons is that amplitudes of the high-frequency displacements are generally smaller than those of low-frequency displacements, causing difficulty in identifying the vibration with the limited resolution of conventional cameras. Another important reason is that the maximum frame rates (fps: frames per second) of the most of conventional video cameras are limited to 30 ~ 60fps at the best resolutions [10, 11]. Though such low frame rates would be sufficient for measuring low-frequency and high-amplitude vibrations of long-period structures, such as high-rise buildings and long-span cable-supported bridges, ensuring higher frame rate is still essential for appropriate monitoring the dynamic behavior of many of small-to-mid scale common civil structures.

One of the issues in these types of dynamic measurements is that anti-aliasing filters are not available for vision-based measuring systems. The only way to minimize such aliasing problem is to increase the frame rate. A high-speed camera allowing up to 2000fps has been investigated for dynamic displacement monitoring [12]. However the practical use of such expensive cameras for civil engineering applications is still in question, because the level of cost and the difficulty of achieving real-time processing can be the main restraint for the success of the technique itself.

Recent advances in smartphone technologies provide various onboard sensing capabilities, including, but not limited to, accelerometer, temperature sensor, GPS, altimeter, gyroscope, and etc. Particularly, embedded cameras show great advances in providing higher-resolution and higher-speed video features, often better than many conventional camcorders. Moreover, their powerful processors and memories allow for onboard processing capabilities, eliminating the need for additional computers to perform extensive image processing. However, such advanced vision and embedded processing capabilities of smartphones have not been effectively utilized for dynamic displacement monitoring applications yet.

This study investigates the feasibilities of such smartphones for dynamic displacement monitoring of civil structures. A new smartphone application is developed for real-time measurement and processing of dynamic displacements using the rear camera of the iPhone 6 Plus and OpenGL (Open Graphic Library) in the iOS environment, which enables easy and low-cost monitoring of absolute dynamic displacements. For real-time applications, a user-selectable crop filter is implemented to optimize the image size and minimize associated processing time, considering the size and distance of target, which allow up to 120fps. To clearly discriminate from the background, carefully designed targets with unique color patterns are used. To make this smartphone application be more widely embraced for practical uses, several useful features, such as autonomous detection of target centroid, email transmission of measured data, user-adjustable color hue range, high-precision time stamps, and automated onboard calibration of measured data are implemented. Following a description of the software developed herein, the performances of the smartphone application are experimentally validated with shake table tests under both indoor and outdoor conditions.

2. State-of-the-art Smartphone Technologies

Recent advances in smartphones technologies provide many attractive features in addition to its original function for mobile telecommunication (see Table 1). Various types of sensors embedded in the smartphones allow the devices to be used for various purposes; for example, motion sensing for game software, proximity sensing for screen power saving, GPS for navigation, fingerprint sensor for device security, and so on. Most of all, what makes the smartphone actually be smart is its onboard computing capability. The speed and size of their microprocessors

Table 1. Hardware specifications of example smartphones

	iPhone 5 [13]	iPhone 5S [14]	iPhone 6/Plus [15]	Galaxy S5 [16]	LG G3 [17]
Release Date	9/12/2012	9/20/2013	9/19/2014	4/11/2014	5/28/2014
CPU	Apple A6:32-bit 1.3 GHz dual core	Apple A7:64-bit 1.3 GHz dual-core	Apple A8:64-bit 1.4 GHz dual-core	1.9 GHz quad-core Cortex-A15 1.3 GHz quad-core Cortex-A7	2.5 GHz quad-core Krait 400
Memory	1 GB LPDDR2-1066 RAM	1 GB LPDDR3 RAM	1 GB LPDDR3 RAM	2 GB LPDDR3 RAM	3 GB (for 32 GB model)
Other Sensors	- Gyroscope - Accelerometer - Digital compass - Proximity sensor - Ambient light sensor	- Gyroscope - Accelerometer - Digital compass - Proximity sensor - Ambient light sensor	- Gyroscope - Accelerometer - Digital compass - Proximity sensor - Ambient light sensor - Barometer	- Gyroscope - Accelerometer - Digital compass - Proximity sensor - Ambient light sensor - Barometer - Infrared (IR) LED sensor	

Table 2. Camera performances of example smartphones

	iPhone 5 [13]	iPhone 5S [14]	iPhone 6/Plus [15]	Galaxy S5 [16]	LG G3 [17]
Rear Camera	- 8 MP iSight camera with 1.5μ pixels - Autofocus - f/2.4 Aperture - True tone flash - Hybrid IR filter	- 8 MP iSight camera with 1.5μ pixels - Autofocus - f/2.4 Aperture - True tone flash - Hybrid IR filter	- 8 MP iSight camera with 1.5μ pixels - Autofocus with focus pixels - f/2.2 Aperture - True tone flash - Hybrid IR filter	- 16 MP - Autofucos - f/2.2 Aperture - LED flash	- 13 MP - Hybrid Infrared Autofocus - f/2.4 Faperture - Dual tone LED flash
HD Rear Camera Capture	- 720p@30/60fps - 1080p@30fps	- 720p@30/60/120 fps - 1080p@30fps	- 720p@30/60/120/240fps - 1080p@30/60fps	- 1080p@30/60fps - 4K@30fps	- 720p@60fps - 1080p@30fps - 4K@30fps
GPU	- PowerVR SGX543MP3	- PowerVR G6430 (four cluster @ 450 MHz)	- PowerVR Series 6 GX6450 (4 clusters)	- ARM Mali T628MP6	- Adreno 330

and memories are sufficiently comparable with decent laptop computers.

The particular focus of this study, related with smartphones' performance, is in the cameras (see Table 2). For example, the latest version of Apple's iPhone (i.e. iPhone 6/Plus) supports up to 240 fps at 720p resolution and 120 fps at 1080p (HD) resolution. Samsung's Galaxy S5 and LG's G3 support up to 4K (UHD) resolution, but with slower frame rate (30 fps). Moreover, the integrated graphics processing unit (GPU) can rapidly manipulate and alter memory to accelerate the creation of images in a frame buffer intended for output to a display.

For this study, Apple's iPhone is selected as its higher frame rate (up to 240 fps) is a more reasonable option for reducing the aliasing issues in dynamic displacement measurements. Moreover, Apple iOS mobile operating system is more appropriate for the development of this application because within a year of its release about 91% of Apple iOS users were running iOS 7, Apple's latest release. Compare this with Android where five of the latest releases each hold about a 10% share of installations [18]. This operating system fragmentation often leads to developers having to support a variety of new and deprecated APIs to accomplish the same tasks. Although Google has taken steps to minimize the effects of operating system fragmentation [19], avoiding compatibility issues was avoidable.

The issues of fragmentation for Android devices are prevalent not only in software but also in the devices' hardware. For example, when comparing the pictures taken with 4 different Android devices under the same conditions, the differences in color and brightness are immediately clear [20]. The core functionality of the application depends on computer vision analysis and introducing variability into this process would make the initial development of the application more difficult.

Developing the app with consistent performance was established as a goal early on in the development process. By eliminating variables in the devices on which the application ran, the first version of the application could be more easily be developed. Developing the app so that it would perform consistently on devices was necessary for the first version. Developing for Android is a goal for future iterations.

3. Object Tracking using Computer Vision

To track the objects using computer vision, i) the objects of interest should be detected in video sequence first, then ii) classify the detected objects, and iii) track the movements of identified targets. Though this is a straightforward process, practical implementation of this object tracking is not that simple, because of possible variability of color, shape, and texture of the objects for each video frame [21]. Many different methods for object tracking using computer vision have been developed for past few decades, which can generally be divided into three categories; i) region-based methods, ii) contour/edge-based methods, and iii) point-based methods.

Region-based methods basically utilize the color features of the objects, as all objects can be represented by their specific color distribution. This method may not be efficient when several objects move at the same time in a video frame, because of the possible occlusion among the moving objects. However, this approach is well known to be computationally much faster than other algorithms and effective for tracking fast moving objects.Despite the shape information possibly being distorted by fast movement, the objects can be traced due to their color [22, 23].

Shape of an object can be characterized by its contour/edge/outline. Edge-based tracking can be represented in active contour model [24] and is known to be efficient in tracking moving objects, because a number of points distributed along the edge of the object can provide higher probability of accurate tracking. However, the performance of this edge-based approach is very sensitive to the initial shape of the object and not so good for 3D movement tracking.

Specific points can also be the characteristic feature of the object. This feature points should be sufficiently different from its neighbor. Usually, such feature points are extracted and detailed by descriptors that can recognize the object [25, 26]. Then the extracted feature points are matched from sequential frames to track the object. The success of this approach is dependent on how well the feature points of the object are extracted and matched, because many other similar points can be regarded as the feature points in the next frame, causing uncertainty.

If desktop or laptop computers are used for processing the images, real-time operation of the vision-based measuring systems may not be an issue. For example, a simple test shows total processing time per each frame to measure the dynamic movement of a target is just about 1~3 millisecond (ms) using a region-based object tracking method with a desktop computer that has Intel's i7-4770 CPU (quad core 64bit 3.40Hz), Nvidia GeForce GTX 650 Ti graphic card (GDDR5 128-bit, OpenGL 4.3, Memory Bandwidth 86.4 GB/sec), and 16GB RAM. Though the hardware capabilities of recent smartphones are comparable to some laptop computers, the performance is less than conventional PCs. Considering the minimization of the processing time as the key factor in realizing higher frame rate for dynamic displacement monitoring using smartphones, an appropriate object tracking method should be selected.

4. OpenCV vs. OpenGL (GPUImage)

The OpenCV library [27] is a popular open-source library for computer vision applications with thousands of optimized algorithms. The iOS-compatible release is written in C++, which can be compiled alongside Objective-C (the language used to write iOS apps), and contains many classes for easily integrating the device's camera with the OpenCV library. Despite OpenCV being a powerful computer vision library, its main drawback for usage in developing a real-time computer vision application is its lack of usage of the iPhone's GPU. Instead, all image processing is performed on the iPhone's CPU. Simple image processing can be accomplished on the CPU in real-time such as adjusting the RGB values or inverting an image. But more complex algorithms like corner detection are more expensive and cannot be performed in real-time in the CPU side of iPhone.

In order to utilize the GPU to perform complex computer vision analysis, the GPUImage library [28] was used in this study. The GPUImage applies GPU-accelerated filters and other effects to images. Filters used with GPUImage are written using the OpenGL Shading Language, using OpenGL ES 2.0 (iPhone 5 and iPhone 5S) or 3.0 (iPhone 5S and later), and are compiled at runtime. The combination of using these filters and processing them on the GPU allows complex image analysis algorithms to run at much higher speeds. Table 3 shows a comparison of rendering speeds on the CPU and GPU.

Table 3. Rendering speed comparisonGPU vs. CPU (larger fps is better)

Calculation	GPU (fps)	CPU (fps)
Thresholding x 1	60.00	4.21
Thresholding x 2	33.63	2.36
Thresholding x 3	1.45	0.05

Source: http://nshipster.com/gpuimage/

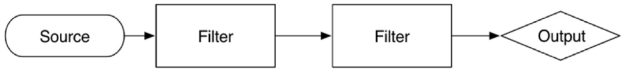

Figure 1. Example image rendering process using GPUImage
Source: http://nshipster.com/gpuimage/

By specifically targeting the hardware of the iPhone in this study, GPUImage allows for faster image processing compared to that of the CPU. To accomplish image rendering on the GPU, GPUImage is built upon an OpenGL rendering pipeline that takes a source image, passes it through a series of filters (or OpenGL shaders), and produces an output (see Figure 1). The simple integration of custom OpenGL shaders

that GPUImage creates allows for easy access to the often complicated OpenGL rendering pipeline.

5. Samrtphone App Development for Real-time Dynamic Displacement Monitoring

5.1 GPUImage library

The iOS platform and the GPUImage library were established as the starting point for the development of the application. Integrating the GPUImage library was accomplished using the Cocoapods dependency manager. After the base application was configured, all future modifications to the application were managed using a private GitHub repository.

Various object tracking methods have been explored under the iOS environment to effectively detect the target of interest and track its centroid movements of each frame front the camera. This started with examining the filters included in the GPUImage library.

Each filter in GPUImage uses OpenGL shaders to process the incoming image and produces a resulting image that can be extracted from the GPU and presented to the user. Color adjustment filters, such like RGB Levels, Hue, and Luminance Threshold filters, were studied to learn how OpenGL can manipulate the colors of an incoming frame from the camera. The color adjustment filters were able to run very quickly because of their heavy reliance on the GPU for manipulating the image. Additionally, image processing filters such as the *Harris Corner Detection*, *Sobel Edge Detection*, and *Hough Transform Line Detection* filters showed how computer vision algorithms could be implemented with OpenGL. The main difference between the color adjustment and image processing filters was the reliance of the image processing filters on the CPU to get access to the raw pixel data from the GPU and the rasterization across each pixel in the image per frame processed. This bottleneck was necessary so that data like the number of corners and the locations of these corners in the image could be determined. By simply running the image processing filters with just their OpenGL shaders and not doing any processing on the CPU, the filters were able to run very quickly. However, introducing the reading of raw pixel data from the GPU onto the CPU led to significant drops in the filters' performance.

5.2 Crop filter

None of the filters included with the GPUImage library could accurately and efficiently identify targets in a full-sized, 720×1280p, image in real-time. Because of the large amount of pixels that had to be processed in each frame, a crop filter was introduced into the rendering pipeline that could crop an image from 720×1280p to 720×100p. The result was a significant drop in processing time per frame for the image processing filters.

5.3 Target design

The color adjustment filters could successfully identify a target (e.g. red-colored targets) in an image by filtering the colors in the incoming image and produce a binary image. The binary image indicated all areas that passed the filter by highlighting the valid areas as white and all ignored areas were black. Despite the ability to identify a target with a certain color, much of the resulting output from color adjustment filters contained false positives of features in the image that were not apart of the intended target but whose RGB values could pass the filter. Similarly, many of the image processing filters like the Harris Corner Detection filter could identify a square target by its corners but its resulting output would often include highlighted areas that met the threshold for detecting a corner but were not apart of the target.

The best target to identify had to be both unique in its appearance and easy and fast to identify by an OpenGL Shader. While researching for good targets to use for identification, the yellow and black color pattern used in crash test simulations by automobile manufacturers became the best choice (see Figure 2). The pattern could be both easily identified by its color pattern and by the corners and edges of the target.

Identifying the target was best found by examining the hue values of each pixel in the image. While the hue values of a color slightly change with minor variations, the RGB values of colors can change dramatically even with minute changes in their appearance. By filtering an

Figure 2. Yellow-black color pattern target on a dummy for car crash test

Source: http://www.carkoon.com/blog/nhtsa-introduces-new-crash-test-dummy-child-safety-seat-evaluation

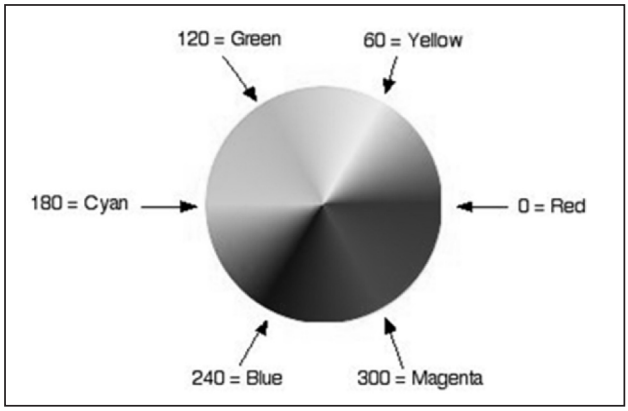

Figure 3. Hue chart of color
(Source: http://www.fmwconcepts.com/imagemagick/huemap/)

image by using a hue range rather than an RGB range, changing the colors that were to be filtered became much easier to change on the fly. The hue scale ranges from 0 to 360 (see Figure 3) and by passing upper and lower hue values to an OpenGL shader, the image could filter out all hues outside of a range. In the OpenGL shader, the value of a pixel's color had to be converted from RGB to hue using a simple algorithm. This was necessary because of the way OpenGL handles colors. For each pixel being processed, OpenGL stores its colors value in RGB. As a result, in order to filter out hue values outside of a given range, the shader must calculate the pixel's hue value.

To identify the center of the color patterned target, a combination of using two hue ranges and the *GPUImage3x3ConvolutionFilter* were required. Two hue ranges were required so that both of the colors in the target could be identified. So a new custom filter was developed by modifying the *GPUImage3x3ConvolutionFilter,* so that the hue values of neighboring pixels in trial-directions could be accessed as shown in the Figure 4. The neighboring pixels of a given pixel were used for identifying the center of the target. For example, as shown in the Figure 5, near the center of the left target, the blue

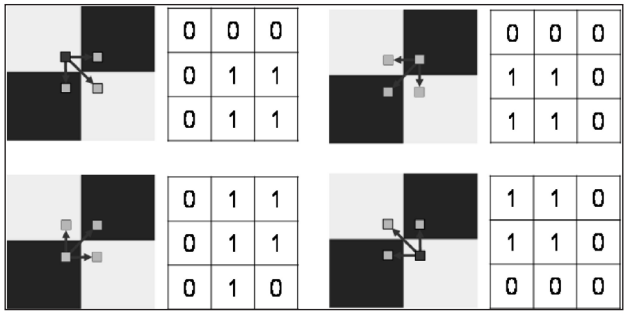

Figure 4.Modified GPUImage3x3 Convolution Filter

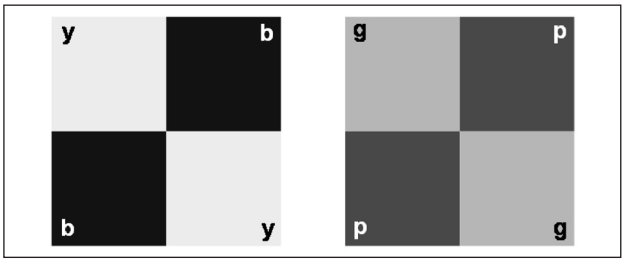

Figure 5.Example pattern of alternating colors: yellow &blue (left), green &purple (right)

and yellow colors border each other. This pattern of alternating colors (e.g. hue value difference between blue and yellow: 180) can be used to effectively identify the center of the target.

5.4 Target centroid calculation

Then, pixels near the center of the target that could be identified using this color pattern were highlighted in the OpenGL shader. Pixels that were not identified by the shader as being pixels near the center of the target were not highlighted. After the shader had processed a frame, the CPU would load the processed image into memory and find all of the pixels that were highlighted. The 2D coordinates of each highlighted pixel were averaged to find the center of the target. The coordinate of the center of the target would be recorded by the application for the use of calculating the displacement of the target at any given frame.

5.5 Real-time displacement calculation and onboard calibration

To calculate real displacement values, two of these targets were required. The second target used the same pattern but with different colors as shown in the Figure 5 (right). The colors used in the second target had similar characteristics to those in the first target in that the level of contrast between the two colors (i.e. green & purple) was very high. By using high contrast colors, the two colors in each target could easily be identified and the risk of the two colors blending together was reduced. By knowing the distance between the two targets in the frame and keeping the distance fixed, the real displace ment of the two targets can be calculated. With GPUImage, the custom OpenGL shader for finding the center of the two targets, and the ability to calculate real displacement of the target in the camera frame, the core functionality of the application was complete.

5.6 Real-time display of processed displacement

Displaying the calculated information on the screen to the user required Apple's Core Animation

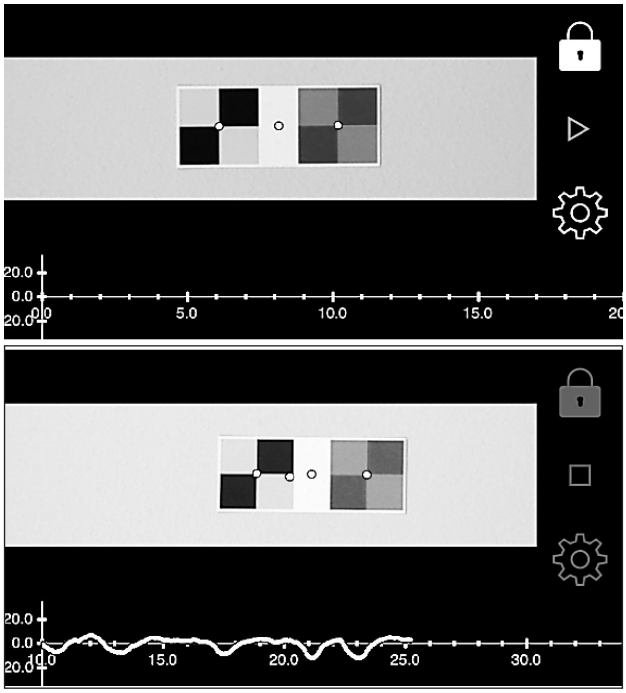

Figure 6.Screen shot of the developed iOS app: before running the app (top), real-time display of measured displacement (bottom)

library and the open source Core Plot library. Core Animation was used to display three dots on the screen that would show where the centers of the targets were. The first two dots were located at the center of each colored target and a third dot was placed in between the two targets to indicate the center of the entire pattern (see the top of Figure 6).

Once the application is started, a forth dot is appeared where the third dot was initially located, which is fixed. Then actual displacement is calculated with respect to the fourth dot (i.e. distance between the third and fourth dots), and is displayed at the bottom of the application screen in real time as shown in the bottom of Figure 6.

5.7 User configurable setting parameters

With each of these components added to the application, many parameters were introduced to control the functionality of each component. A settings feature was introduced into the application that managed how each component should perform. The settings were separated into three sections: Camera, Filter, and Graph. The options under each section are listed in the Table 4.

5.8 Setting parameter optimization

While the application could identify the target in the camera frame and calculate its displacement at each frame, its performance was slightly above the target of being below 10 milliseconds on the iPhone 6 Plus. The slowest portions of the application were identified through profiling the application using the Instruments software included with Apple's Xcode. By identifying potential areas of slow performance and memory leaks the application's processing time from capture to display was drastically increased.

- The biggest improvement in processing time was achieved simply by not displaying the camera

Table 4. Setting parameters

Camera Settings	
Frame Rate	Manually adjust the camera's frame rate 30, 60, 120 and 240 fps.
Crop Size (width & height)	Change the size of the crop filter Width (px):100/200/400/720/1280 Height (px):100/200/400/720
Auto-Focus Range	Change the autofocus range of the camera between near, far and none.
Show Camera View	Whether or not the feed from the camera should be shown on the screen.
Show Benchmark	Whether or not the current and average processing time from capturing to filtering, to displaying the image should be calculated and shown on the screen.

Filter Settings	
Show Filtered View	Whether the resulting output from the OpenGL shader should be shown in place of the raw camera view.
Pixel Search Distance	The distance between neighboring pixels used in the OpenGL shader.
Set Filter Colors	Select the hue ranges of the two colors used in each target.

Graph Settings	
Show Graph View	Whether the graph should be updated with displacement calcultions from each frame.
Target Distance (cm)	The distance (in centimeters) of the two colored targets in the camera frame.
Show X & Y Displacement	Whether the X, Y, or both displacement lines should be calculated and shown on the graph.

feed on the screen. This resulted in about a 2 to 3 millisecond drop in processing time.

- Another improvement in processing time was achieved by running all camera related operations on a separate thread and running all UI (user interface) operations on the main thread.

However, much of the slowest portions of the application could not be resolved so easily. Portions of the application could not be removed as they were integral to the application. Reducing the processing time in components like reading the raw pixel data to the CPU from the GPU, calculating the center of each target on the CPU by averaging the coordinates of all found pixels, and performing displacement calculations were difficult due to their lack of complexity and necessity to the functionality of the application.

After resolving performance issues in the application, the application's processing time was reduced to below 7 milliseconds on the iPhone 6 Plus. Due to the constraints of the hardware on the iPhone 5, such results could not be achieved. The Table 5 shows a breakdown of the processing time (average from several tests) for the application.

Table 5. Processing time breakdown (with 720×100p @ 120 fps)

Step	iPhone 5	iPhone 6 Plus
GPUImage (no display)	1.10 ms	1.10 ms
GPUImage + Crop Filter (no display)	1.34 ms	1.42 ms
GPUImage + Crop Filter + Custom Filter (no display)	35.2 ms	6.30 ms
Total w/ Displaying	37.1 ms	11.25 ms
Total w/o Displaying	35.2 ms	6.30 ms

5.9 Email transmission of measured data

Additional features were developed to allow the user to view the graph full screen after a recording session had ended and to export the collected data to a CSV file that can be emailed to a personal account for further analysis. These changes made the application suitable for testing and practical use.

Figure 7 shows the simplified block diagram of the developed iOS application in this study.

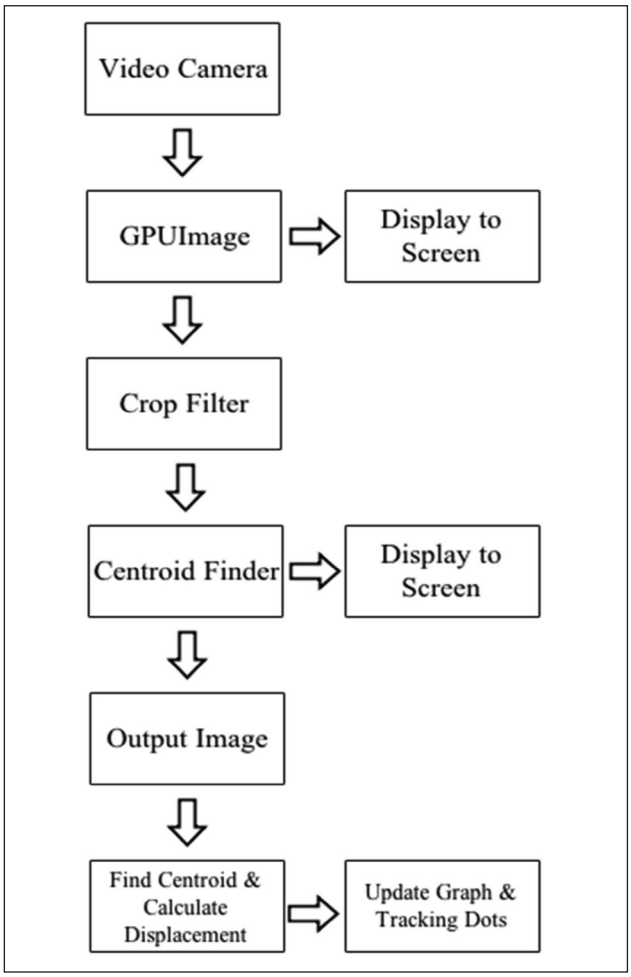

Figure 7. Software block diagram of developed iOS app

6. Experimental Validations

In order to evaluate the performances of the developed iOS app, including sampling time accuracy and the ability to track the dynamic movements of targets, a series of laboratory-scale tests have been carried out using a shaking table with single-frequency and multi-frequency sinusoidal motions.

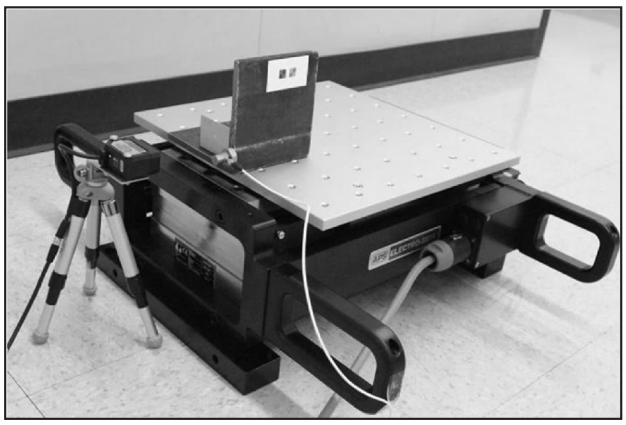

Figure 8. Shaking table test setup

6.1 Experiment setup

An APS Dynamics' APS 400 Electro-Seis shaker was used for the evaluation tests (see Figure 8). The input excitation of the shaker was amplified by the APS 145 amplifier. To compare the performance of the developed iOS App with that of a conventional displacement sensor, a laser displacement sensor (KEYENCE, IL-100, 4-μm resolution) was used as a reference. The analog voltage outputs from the laser

Figure 9.12× (left) and 50× (right) optical zoom lens designed for smartphones

sensor were measured by the National Instruments' NI-9234 ADC module (24-bit Delta-sigma ADC) with CompactDAQ chassis (cDAQ-9178 model). At the same time, NI-9269 voltage output module, which was housed in the same CompactDAQ, was used to generate the excitation signals for the shaker.

To overcome the limited resolution of the iPhone camera for long-distance and small-target measurements, optical zoom lenses were used in conjunction with the iPhone (see Figure 9). With commercially available low-cost zoom lenses, precisely designed smartphone cover cases that allow easy connection of the lens to the phone come with the package. 12× and 50× zoom lens were considered initially, but the 50× lens only was used for this tests.

6.2 Sampling Time Accuracy

Consistency of the sampling rate or sampling time is important to ensure the quality of dynamic vibration measurements. Even when conventional analog-to-digital converters are used, the time intervals between adjacent samples are not always consistent [29]. Particularly, because this kind of computer vision-based measuring systems handle extensive image processing, making sure the consistency of the sampling time is important.

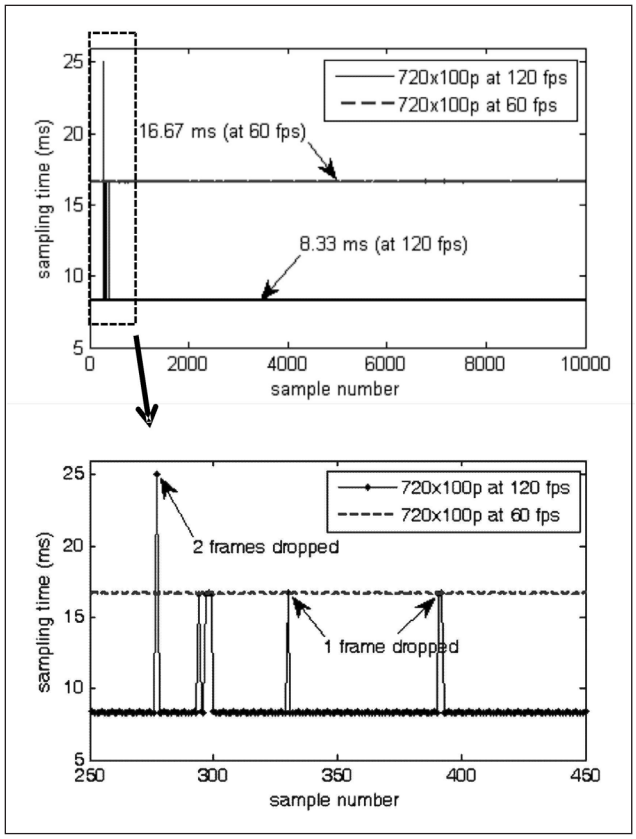

Figure 10.Sampling time accuracy (bottom: zoomed around sample # 350)

Figure 10 shows the example record of the sampling time for 60fps and 120fps cases (720×100p crop filter used for both). The case with 60fps (dotted line) shows very consistent sampling time of 16.67 milliseconds over entire measurements. However, when 120fps (solid line) was used, little inconsistencies are observed in the beginning of the measurements for couples of samples, of which phenomenon is attributed by the dropped samples (see the bottom of Figure 10). To achieve 120fps, all the image processing required to get the displacement information should be done within 8.33ms for each frame. If the processing takes more than 8.33ms, then the software automatically drops the corresponding sample out, to not cause any delay or interference to following samples. Because the case of 60fps ensures sufficient time for processing, such dropped samples were not observed in this test.

6.3 Shake Table Tests

For the initial shake table tests indoors, the iPhone with the zoom lens was placed 3.0m away from the target attached on the shake table. The target size was 1.0×2.5cm, which was composed of two rectangular alternating color patterns having 1.5cm center distance between them. 720×100p crop filter was used to track

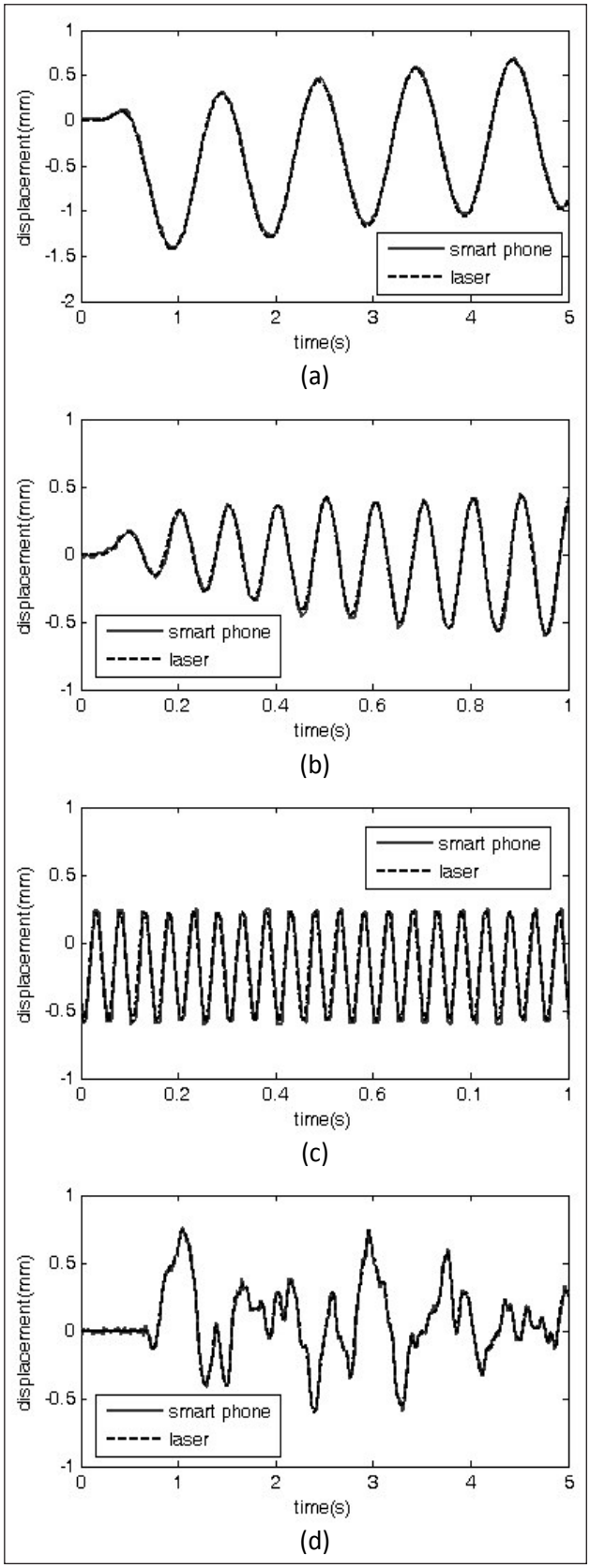

Figure 11.Indoor shake-table test results (3m from target): (a) 1Hz sine at 120fps, (b) 10Hz sine at 120fps, (c) 20Hz sine at 120fps, and (d) multi-tone sine signal at 120fps.

Figure 12.Shake-table test setup in the outdoor hallway

the target in a horizontal direction in an optimized way. The distance between the two color patterns (i.e. 1.5cm) was occupied by about 300~400 pixels, corresponding resolution for this particular set up could be estimated about 0.0375~0.05mm; actual size of each pixel was autonomously calibrated in the software and used for displacement calculation.

Figure 11 shows the shake table test results for the 1Hz, 10Hz, 20Hz sinusoidal excitations, and multi-tone excitation composed of 1~20Hz (0.2Hz step) sinusoidal signals. Vibration levels were kept below 2 mm amplitude (peak to peak), and 120 fps was used in this test. As shown in the Figure 11, the dynamic displacements measured by the iPhone 6 Plus with the developed iOS app (solid line in the Figure) agree very well with those by the laser displacement sensor (dotted line in the Figure).

Then, the shake table set ups were moved out for outdoor testing with longer target distance. The shake table set ups were placed in the outdoor hallway of the civil engineering building at the University of Arizona, of which hallway can ensure up to 50m clear line-of-sight (see Figure 12). Target distance from the iPhone camera was 33m and the same zoom lens was used, but with little bigger target (4×10cm target size and 6cm center distance between two color patterns).

Figure 13 shows some example results from the outdoor shaking table tests. The performances of the iPhone with the developed app were not so impressive, compared with indoor tests. Particularly when 120fps was used, substantial high-frequency noises were observed in the measurements by iPhone

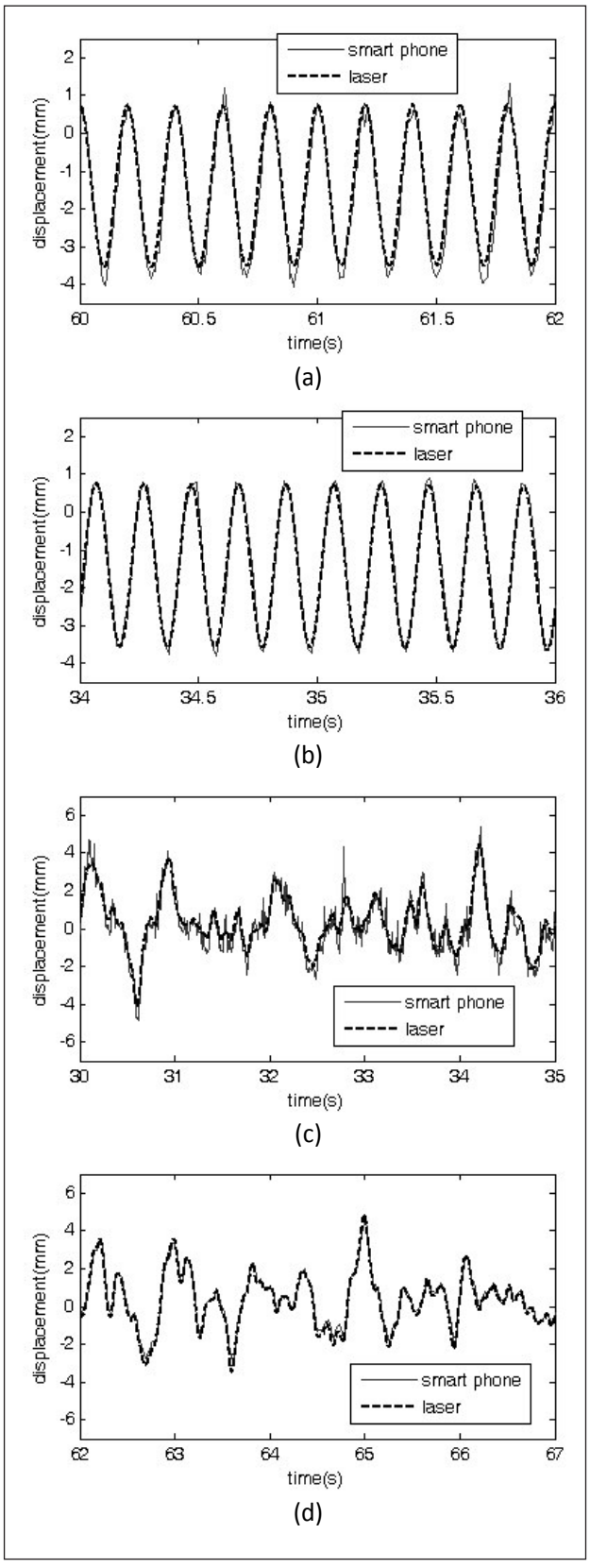

Figure 13.Outdoor shake-table test results (33m from target): (a) 5Hz sine at 120fps, (b) 5Hz sine at 60fps, (c) multi-tone sine at 120fps, and (d) multi-tone sine signalat 60fps.

(solid line in the Figure) as shown in the Figure 13 a) and c), while the results from 60fps were acceptable, successfully resolving millimeter-level displacements. Possible reasons for these high-frequency noises in outdoor tests may be attributed to, but not limited to, possibilities that i) the captured image at 120fps might be exposed to less amount of light as the higher frame rate allows the shorter exposure time, which could change the color properties in the image, ii) the phone might be subjected to unexpected high-frequency vibrations due to wind and/or building vibrations, resulting in such noisy measurements; though it is a very little vibration, its effects on the captured images would be substantial, as the target is located further and further away.

No matter what the reasons for causing such high-frequency noises, possible vibrations of the phone itself should be compensated for the practical use of this approach for dynamic displacement measurements in the field. Other sensors (e.g. accelerometer, gyroscope) embedded in the smartphone (see Table 1) may be utilized for the phone vibration compensation. To ensure sufficient amount of light for outdoor tests, a self-light emitting target (e.g. LED) may be used for future tests. In addition, a low-pass filtering can be implemented in the iOS app to reduce such high-frequency noises.

7. Conclusions

The feasibility of smartphone technologies for real-time dynamic displacement monitoring has been investigated in this study. A new smartphone application was developed under iOS environment for the iPhone. Various methods for moving object tracking have been explored, then, a region/color-based tracking method was adapted in this study because of its computational efficiency in image processing and robustness in tracking fast moving objects. In order to fully utilize the GPU capabilities of smartphones, the GPUImage library was used in developing the iOS app. A crop filter was implemented for users to compromise between the image size and frame rate without sacrificing accuracy. Onboard calibration of the image pixel size to a given-dimension target was implemented in the developed iOS app. And other various features for controlling camera, filter, and graph settings and email transmission of measured data were also incorporated in this iOS app development. All the functions required for measuring the dynamic movements of the target could successfully be operated in real time,

allowing up to 120fps with iPhone 6 Plus. And the performances of the iPhone hardware and the iOS app developed herein were experimentally validated. Although some high-frequency noises were observed from outdoor shake-table tests, the performances of the developed app were comparable to those of a conventional laser displacement sensor, allowing down to sub-millimeter resolutions at 33m distance from the target. The possibilities and limitations of the smartphone (iPhone) and its camera for real-time dynamic displacement monitoring applications have been explored in this study, pointing in the direction of the following research.

References

1. Fujino, Y., Murata, M., Okano, S., and Takeguchi, M. (2000), "Monitoring system of the Akashi Kaikyo Bridge and displacement measurement using GPS," *Proc. of SPIE, nondestructive evaluation of highways, utilities, and pipelines IV*, 229–236.
2. Casciati, F. and Fuggini, C. (2009), "Engineering vibration monitoring by GPS: long duration records," *Earthquake Engineering and Engineering Vibration*, Vol. 8(3), 459-467.
3. Yi, T.H., Li, H.N., and Gu, M. (2012), "Recent research and applications of GPS based monitoring technology for high-rise structures," *Structural Control and Health Monitoring,* Published online, DOI: 10.1002/stc.1501.
4. Jo, H., Sim, S.H., Tatkowski, A., Spencer Jr., B.F., and Nelson, M.E. (2012), "Feasibility of Displacement Monitoring using Low-cost GPS Receivers", *Structural Control and Health Monitoring*, 20(9), 1240-1254.
5. Malesa M, Szczepanek D, Kujawinska M, Swiercz A, Kolakowski P. (2010), "Monitoring of civil engineering structures using digital image correlation technique", *ICEM 14–14th International conference on experimental mechanics*. Poitiers, France.
6. Caetano, E., Silva, S., Bateira, J., (2011), "A vision system for vibration monitoring of civil engineering structures", *Experimental Techniques,* 74–82.
7. Bell E, Peddle J, Goudreau A. (2012), "Bridge condition assessment using digital image correlation and structural modeling", *IABMAS'12 – Bridge maintenance, safety, management, resilience and sustainability*, Dubrovnik, Croatia, 330–7.
8. Ji, Y.F. and Zhang, O.W. (2012), "A novel image-based approach for structural displacement measurement", *Proc. 6th Int. Conf. Bridge Maintenance, Safety Manag*., 407–414.
9. Ribeiro, D., Calcada, R., Ferreira, J., and Martins, T. (2014), "Non-contact measurement of the dynamic displacement of railway bridges using an advanced video-based system", *Engineering Structures*, 75, 164-180.
10. Ho, H.N., Lee, J.H., Park, Y.S., & Lee, J.J. (2012), "A Synchronized Multipoint Vision-Based System for Displacement Measurement of Civil Infrastructures", *The Scientific World Journal*.
11. Fukuda, Y., Feng, M., Narita, Y., Kaneko, S. I., & Tanaka, T. (2010), "Vision-based displacement sensor for monitoring dynamic response using robust object search algorithm", . *Sensors, IEEE,* 1928-1931.
12. D'Emilia, G., Razzè, L., & Zappa, E. (2013), "Uncertainty analysis of high frequency image-based vibration measurements", *Measurement*, *46*(8), 2630-2637.
13. "IPhone 5." *Wikipedia*. Wikimedia Foundation, 11 Apr. 2014. Web. 04 Nov. 2014 (http://en.wikipedia.org/wiki/IPhone_5).
14. "IPhone 5S." *Wikipedia*. Wikimedia Foundation, 11 May 2014. Web. 04 Nov. 2014 . (http://en.wikipedia.org/wiki/IPhone_5S).
15. "IPhone 6." *Wikipedia*. Wikimedia Foundation, 11 July 2014. Web. 04 Nov. 2014 (http://en.wikipedia.org/wiki/IPhone_6).
16. "Samsung Galaxy S5." *Wikipedia*. Wikimedia Foundation, 11 June 2014. Web. 04 Nov. 2014 (http://en.wikipedia.org/wiki/Samsung_Galaxy_S5).
17. "LG G3." *Wikipedia*. Wikimedia Foundation, 11 Jan. 2014. Web. 04 Nov. 2014 (http://en.wikipedia.org/wiki/LG_G3).
18. http://appleinsider.com/articles/14/08/22/while-91-of-apple-users-run-ios-7-five-different-versions-of-android-hold-10-share
19. http://www.theguardian.com/technology/2014/aug/22/android-fragmented-developers-opensignal
20. "LG G3 Review." *TechSpot*. N.p., n.d. Web. 07 Nov. 2014 (http://www.techspot.com/review/847-lg-g3/page5.html).
21. Deori, B., and Thounaojam, D.M. (2014), "A SURVEY ON MOVING OBJECT TRACKING IN VIDEO", *International Journal on Information Theory (IJIT)*, 3(3).
22. Li, L., Ranganath, S., Weimin, H., and Sengupta, K. (2005), "Framework for Real-Time Behavior Interpretation From Traffic Video", *IEEE Tran. On Intelligen Transportation Systems*, 6(1), 43-53.
23. Kumar, P., Weimin, H., Gu, I.U., and Tian, Q. (2004), "Statistical Modeling of Complex Backgrounds for Foreground Object Detection", *IEEE Trans. On Image Processing*, 13(11), 43-53.
24. Serby, D., Meier, E.K., and Gool, L.V., (2004), "Probabilistic Object Tracking Using Multiple Features", *IEEE Proc. of International Conf on Pattern Recognition Intelligent Transportation Systems*, 6, 43-53.
25. Zivkovi, Z. (2004), "Improving the selection of feature points for tracking", *Pattern Analysis and Applications*, 7(2).
26. Lou, J., Tan, T., Hu, W., Yang, H., and Maybank, S.J. (2005), "3D Model-Based Vehicle Tracking", *IEEE Trans. on Image Processing*, 14, 1561-1569.
27. "OpenCV." Web. 07 Nov. 2014 (http://opencv.org/).
28. "BradLarson/GPUImage." *GitHub*., Web. 04 Nov. 2014 (https://github.com/BradLarson/GPUImage).
29. Nagayama, T., and Spencer, B. F., Jr. (2007). "Structural health monitoring using smart sensors." *Newmark Structural Engineering Laboratory (NSEL) Rep. Series No. 1*,Univ. of Illinois at Urbana-Champaign, Champaign, IL.

SRESA JOURNAL SUBSCRIPTION FORM

Subscriber Information (Individual)

_____ _____ _____ _____

Title First Name Middle Name Last Name

_____ _____

Street Address Line 1 Street Address line 2

_____ _____ _____ _____ _____

City State/Province Postal Code Country

_____ _____ _____

Work Phone Home Phone E-mail address

Subscriber Information (Institution)

Name of Institution/ Library _____

Name and Designation of Authority for Correspondence _____

Address of the Institution/Library _____

Subscription Rates

	Subscription Quantity	Rate	Total
Annual Subscription (in India)	_____	Rs. 15, 000	_____
(Abroad)	_____	$ 500	_____
	_____		_____
	_____		_____

Payment mode (please mark)

Cheque ☐ Credit Card ☐ Master Card ☐ Visa ☐ Online Banking ☐ Cash ☐ De mand Draft ☐

Credit card Number _____

Credit Card Holders Name _____

Credit Card Holde _____

Guidelines for Preparing the Manuscript

A softcopy of the complete manuscript should be sent to the Chief-Editors by email at the address: editor@sresa.org.in. The manuscript should be prepared using 'Times New Roman' 12 font size in double spacing, on an A-4 size paper. The illustrations and tables should not be embedded in the text. Only the location of the illustrations and tables should be indicated in the text by giving the illustration / table number and caption.

The broad structure of the paper should be as follows: a) Title of the paper – preferably crisp and such that it can be accommodated in one or maximum two lines with font size of 14 b) Name and affiliation of the author(s), an abstract of the paper in ~ 100 words giving brief overview of the paper and d) Five key words which indicates broad subject category of the paper. The second page of the paper should start with the title followed by the Introduction

A complete postal address should be given for all the authors along with their email addresses. By default the first author will be assumed to be the corresponding author. However, if the first author is not the corresponding author it will be indicated specifically by putting a star superscript at the end of surname of the author.

The authors should note that the final manuscript will be having double column formatting, hence, the size of the illustration, mathematical equations and figures should be prepared accordingly.

All the figures and tables should be supplied in separate files along with the manuscript giving the figure / table captions. The figure and table should be legible and should have minimum formatting. The text used in the figures and tables should be such that after 30% reduction also it should be legible and should not reduced to less than font 9.

Last section of the paper should be on list of references. The reference should be quoted in the text using square bracket like '[1]'in a chronological order. The reference style should be as follow:

1. Pecht M., Das D, and Varde P.V., "Physics-of-Failure Method for Reliability Prediction of Electronic Components", Reliability Engineering and System Safety, Vol 35, No. 2, pp. 232- 234, 2011.

After submitting the manuscript, it is expected that reviews will take about three months; hence, no communication is necessary to check the status of the manuscript during this period. Once, the review work is completed, comments, will be communicated to the author.

After receipt of the revised manuscript the author will be communicated of the final decision regarding final acceptance. For the accepted manuscript the author will be required to fill the copy right form. The copy right form and other support documents can be down loaded from the SRESA website: http://www.sresa.org.in

Authors interested in submitting the manuscript for publication in the journal may send their manuscripts to the following address:

Society for Reliability and Safety
RN 68, Dhruva Complex
Bhabha Atomic Research Centre,
Mumbai – 400 085 (India)
e-mail : editor@sresa.org.in

The Journal is published on quarterly basis, i.e. Four Issues per annum. Annual Institutional Subscription Rate for SAARC countries is Indian Rupees Ten Thousand (Rs. 10,000/-) inclusive of all taxes. Price includes postage and insurance and subject to change without notice. For All other countries the annual subscription rate is US dollar 500 ($500). This includes all taxes, insurance and postage.

Subscription Request can be sent to SRESA Secretariat (please visit the SRESA website for details)

SRESA's International Journal of

Life Cycle Reliability and Safety Engineering

Contents

Vol.4 Issue No.2 April-June 2015 ISSN – 2250 0820